

TECHNISCHE UNIVERSITÄT MÜNCHEN
Max-Planck-Institut für Biochemie
Abteilung für Molekulare Strukturbiologie

Structural Analysis of Presynaptic Architecture by Cryoelectron Tomography

Rubén Fernández-Busnadiego

Vollständiger Abdruck der von der Fakultät für Chemie
der Technischen Universität München
zur Erlangung des akademischen Grades eines
Doktors der Naturwissenschaften
genehmigten Dissertation.

Vorsitzender:

Univ.-Prof. Dr. Dr. h. c. H. Kessler

Prüfer der Dissertation:

1. Hon.-Prof. Dr. W. Baumeister

2. Univ.-Prof. Dr. S. Weinkauff

Die Dissertation wurde am 05.01.2010 bei der Technischen Universität München
eingereicht und durch die Fakultät für Chemie am 31.03.2010 angenommen.

Contents

Abstract.....	5
1. Introduction.....	9
1.1 Synaptic Transmission.....	9
1.2 The Presynaptic Terminal.....	10
1.2.1 The synaptic vesicle cycle.....	10
1.2.2 Synaptic vesicle exocytosis.....	12
1.2.3 The presynaptic cytomatrix.....	15
1.2.4 Electron microscopy analysis of presynaptic architecture.....	16
2. Electron Microscopy and Tomography.....	21
2.1 Transmission Electron Microscopy.....	21
2.1.1 Components of transmission electron microscopes.....	21
a) Electron gun.....	21
b) Illumination system.....	21
c) Imaging system.....	23
d) Image detection system.....	23
e) Other TEM systems.....	23
2.1.2 Image formation: Phase contrast.....	24
2.2 Sample preparation.....	28
2.2.1 Radiation damage and noise.....	29
2.3 Cryo-Electron Tomography.....	30
2.3.1 Automated data acquisition.....	31
2.3.2 3D reconstruction.....	32
2.3.3 Tomogram analysis.....	34
3. Aims of This Study.....	37
4. Materials and Methods.....	41
4.1 Sample preparation.....	41
4.1.1 Synaptosomal extraction.....	41
4.1.2 Glutamate release assay.....	41
4.1.3 Pharmacological treatments and vitrification of synaptosomes.....	43
4.1.4 Hippocampal slice cultures, high pressure freezing and cryosectioning.....	43
4.1.5 Hippocampal neurons in culture.....	44
4.2 Cryo-Electron Tomography.....	44
4.3 Data analysis.....	45
5. Results.....	51
5.1 Establishment of the experimental system.....	51
5.2 The presynaptic cytomatrix in cortical synaptosomes and hippocampal organotypic slices.....	56
5.2.1 Morphology of frozen-hydrated presynaptic terminals.....	56
5.2.2 Inhomogeneity in the spatial distribution of synaptic vesicles.....	59
5.2.3 Extensive interconnectivity of synaptic vesicles.....	61
5.2.4 Clusters of interconnected synaptic vesicles.....	64
5.2.5 Tethering of proximal synaptic vesicles to the active zone.....	67
5.2.6 Synaptic vesicle size.....	69
5.2.7 Direct membrane contact between synaptic vesicles and the active zone.....	72
5.3 Computational procedures for the analysis of presynaptic architecture.....	74

5.3.1	Hierarchical classification of connectors and tethers.....	76
5.4	Observations on other neuronal structures.....	80
5.4.1	The postsynaptic density and the synaptic cleft.....	80
5.4.2	Morphology of neurons in culture	82
6.	Discussion.....	87
6.1	Morphology of frozen-hydrated neuronal preparations.....	87
6.2	Automated segmentation and analysis of presynaptic ultrastructure.....	88
6.3	The role of synaptic vesicle connectors in vesicle mobilization.....	89
6.4	Active zone organization, tethering and synaptic vesicle progression towards fusion.....	90
6.5	Synaptic vesicle distribution in resting synapses is not homogeneous.....	93
7.	Outlook	97
	Abbreviations.....	99
	Acknowledgments.....	101
	References.....	103

Abstract

Presynaptic terminals contain a large number of neurotransmitter-filled synaptic vesicles embedded in a dense filamentous network. Although intensely studied over the last decades, the organization and cellular role of this network remain unclear. Combining cryo-electron tomography with pharmacological manipulations, this work provided a quantitative assessment of the structural elements mediating synaptic vesicle organization and release in mammalian central nervous system synapses. The major conclusions of this study are the following:

1. **Cortical synaptosomes and hippocampal organotypic slices are complementary preparations that form an appropriate experimental system for the study of the native presynaptic cytomatrix in vitreous frozen-hydrated samples.** Synaptosomes allow different pharmacological manipulations, whereas slices provide a direct view into nervous tissue. In this work, presynaptic morphology was comparable in both kinds of samples, pointing to a limited influence of preparation artifacts.
2. **An automated segmentation algorithm was developed to allow a quantitative analysis of vesicle distribution and the presynaptic cytomatrix,** introducing quantitative tools for the analysis of tomographic data from pleomorphic biological structures.
3. **The short filaments that link synaptic vesicles to each other (connectors) and to the active zone (tethers) are the main components of the presynaptic cytomatrix.** Longer filaments are much less abundant and therefore likely to play secondary roles.
4. **The rearrangement of connectors upon synaptic stimulation and inhibition of phosphatases suggests that these connectors play an important role in vesicle mobilization.**
5. **The comparison between synapses at rest and those stimulated by KCl or hypertonic sucrose points to a link between the configuration of the tethering assembly and vesicle availability for release.** Short tethers were significantly removed under treatments known to (a) release the readily releasable pool (hypertonic sucrose) or (b) cleave synaptobrevin, one of the components of the SNARE complex (tetanus toxin), suggesting that **the SNARE complex is involved in the formation of the short tethers.**

1 Introduction

1. Introduction

1.1 Synaptic Transmission

The transfer of information between neurons, or between neurons and other excitable cells, takes place at specialized junctions called *synapses*. In the mammalian central nervous system, most synapses function by converting electrical signals travelling along axons into chemical substances (*neurotransmitters*) that are released onto the partner cell. Very different structures are formed at each side of the synapse (termed *pre-* and *postsynaptic* respectively), resulting in unidirectional communication. Presynaptic terminals, also known as *boutons*, are typically formed at the terminal regions of axons or in axonal shafts (*en passant* boutons). They contain neurotransmitter-filled synaptic vesicles and the machinery necessary for vesicle exocytosis, plus other organelles such as endoplasmic reticulum and mitochondria. The postsynaptic side, normally found on dendrites, harbors a dense array of postsynaptic receptors, ion channels and signaling and scaffolding proteins known as the *postsynaptic density* (PSD). The *synaptic cleft* separates pre- and postsynaptic sides and contains the cell adhesion molecules that are responsible for the tight coupling between both terminals.

Electric signals (*action potentials*) are generated at the initial segment of the axon (*axon hillock*) and travel along the axon causing membrane depolarization in presynaptic terminals. This results in the opening of voltage-gated Ca^{2+} channels that allow Ca^{2+} influx into the cell. The machinery for synaptic vesicle exocytosis is triggered by Ca^{2+} sensors. Thus, upon Ca^{2+} influx, vesicles are exocytosed and release neurotransmitter into the synaptic cleft. Neurotransmitter molecules diffuse across the cleft and eventually bind to the receptors of the postsynaptic cell, causing postsynaptic ion channels to open or close. This alteration in the ionic flux results in a postsynaptic excitatory or inhibitory potential that changes the excitability of the postsynaptic cell (Figure 1).

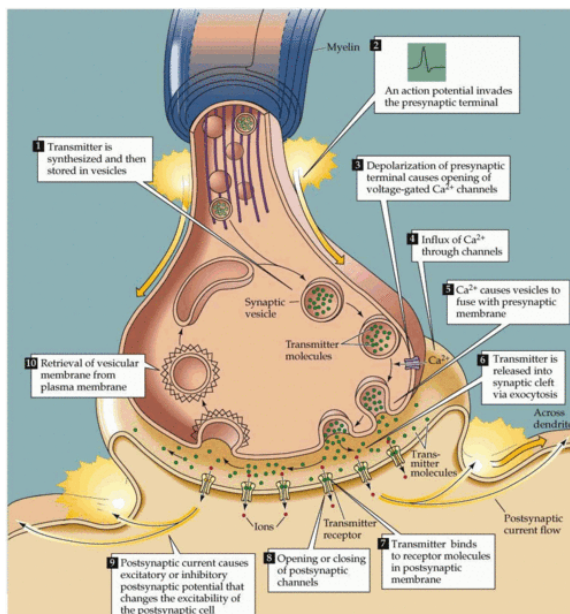


Figure 1 Sequence of events leading to synaptic transmission. The presynaptic terminal occupies the upper part of the image (Purves et al., 2008).

While synaptic transmission shares many features with other trafficking processes in the cell, it is also unique in many ways. An exquisite and intricate machinery has evolved to provide speed, reliability and precision to one of the most critical and tightly regulated processes in animal life.

1.2 The Presynaptic Terminal

In the mammalian central nervous system, most neurons form more than 500 presynaptic terminals, each of them typically containing 100-500 synaptic vesicles. Presynaptic terminals are not mere secretory machines, but also small computational units where the relation between input (action potential) and output (neurotransmitter release) is precisely regulated and varies in response to different signals, giving rise to the so-called *presynaptic plasticity*. Plasticity mechanisms, both pre- and postsynaptic, are believed to be the base of information storage and memory in the brain (for review see Kullmann and Lamsa, 2007).

In presynaptic terminals, exocytosis occurs at the so-called *active zone* (AZ) (Couteaux and Pecot-Dechavassine, 1970; Gundelfinger et al., 2003), a specialized region of the presynaptic membrane that directly faces the postsynaptic side and that hosts the fusion machinery (1.2.2). After exocytosis, vesicles are again retrieved for further use by endocytic mechanisms (1.2.1). A very dense network of filaments the so-called *presynaptic cytomatrix*, surrounds synaptic vesicles in presynaptic terminals. However, the composition and organization of this prominent structure, as well as its role in the synaptic vesicle cycle are not yet well understood (1.2.3).

1.2.1 The synaptic vesicle cycle

Neurotransmission was proposed to be mediated by exocytosis of neurotransmitter-filled synaptic vesicles by (Katz, 1969). Thereafter, decades of intensive research have provided proof for this hypothesis, making synaptic vesicles the best characterized cellular organelle (Südhof, 2006).

Synaptic vesicles are small (~ 40 nm in diameter) lipid spheres harboring a high amount of membrane proteins (Takamori et al., 2006). Trafficking proteins, such as SNAREs and Rabs, are by far the most abundant, followed by the vesicular neurotransmitter transporters, such as VGLUT1/2 (in glutamatergic synapses). Synaptic vesicles contain as well signaling and cell-surface proteins, together with one or two copies of the vacuolar ATPase that fuels the neurotransmitter transporters. Phospholipids (50%) and cholesterol (41%) account for the majority of the lipids of the membrane (Figure 2).

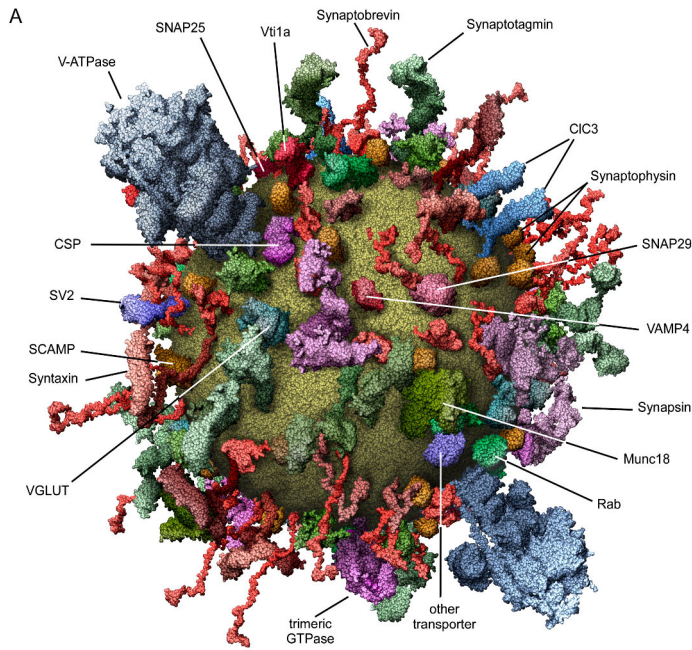


Figure 2 Molecular model of an average synaptic vesicle, quantitatively representing the most abundant vesicle proteins. Protein structures are modeled from existing partial or complete crystal structures, structures of similar or homologous proteins, or secondary structure predictions followed by short molecular dynamics simulations (Takamori et al., 2006).

Upon arrival of an action potential, the opening of voltage-gated Ca^{2+} channels causes Ca^{2+} influx into the presynaptic terminal, triggering synaptic vesicle release. This release is composed of a fast synchronous component, which takes place $\sim 50\text{-}100\ \mu\text{s}$ after Ca^{2+} influx, and a slower asynchronous component that continues for up to 1 s. Ca^{2+} concentration is believed to raise above release thresholds only in small *microdomains* around clusters of Ca^{2+} channels. Thus, only vesicles present in these regions can be exocytosed by Ca^{2+} influx (Neher and Sakaba, 2008). Under strong stimulation, vesicles from more distal areas are also mobilized towards the AZ by unknown mechanisms, which could also be Ca^{2+} -dependent (Levitan, 2008). It should be noted that spontaneous release of individual vesicles also occurs independently of synaptic activity, and that the extent of the implication of Ca^{2+} in this process has not been fully clarified yet.

The organization of synaptic vesicles is usually described in terms of functional pools (Rizzoli and Betz, 2005). The *readily released pool* (RRP) consists of vesicles that can be immediately exocytosed upon Ca^{2+} influx; they are primed for release and thought to be *docked* to the AZ (see 1.2.2). However, not all docked vesicles belong to the RRP (Rollenhagen and Lübke, 2006). The *recycling pool* is formed by vesicles released to sustain synaptic transmission under mild stimulation and includes the RRP. Vesicles mobilized only under strong stimulation constitute the *reserve pool*.

Following exocytosis, different endocytic mechanisms allow vesicle replenishment. In the case of vesicles that undergo full-collapse fusion with the cell membrane, clathrin-coated buds are generated and then scised from the membrane by the action of dynamin spirals. This pathway can also involve endosomal sorting of vesicle components, requiring several seconds for completion. Alternatively, in the so called *kiss-and-run* pathway, vesicles fuse with the cell membrane without collapsing and retaining their individual identity (i.e., most of their membrane proteins). Neurotransmitter refilling takes place in $\sim 50\text{-}100\ \text{ms}$. This fast mode of endocytosis is thought to dominate at low stimulation frequencies, whereas the slower clathrin-

mediated pathway comes into action at higher frequencies (Südhof, 2004)¹. Under very strong stimulation, *bulk* endocytosis has also been observed (Smith et al., 2008).

1.2.2 Synaptic vesicle exocytosis

SNARE proteins have been shown to drive most intracellular membrane fusion events in eukaryotes, including synaptic vesicle exocytosis (Chen and Scheller, 2001). SNARE proteins contain a homologous 70-residue sequence called SNARE motif, which assembles into a four-helix bundle to form the SNARE core complex (Sutton et al., 1998) (Figure 3A). The neuronal SNARE complex is formed by the vesicular SNARE protein synaptobrevin/VAMP together with syntaxin and SNAP-25 (the latter containing two SNARE motifs), which reside at the plasma membrane and are therefore referred to as *target SNAREs*. The association of vesicular and target SNAREs into the very stable SNARE core complex can overcome the energy barrier for fusion, bringing both membranes into very close proximity. However, the sole action of SNARE proteins is not sufficient to achieve membrane fusion *in vivo*, and the aid of the so-called SM proteins is also required (Figure 3C). Thus, in mice where the neuronal SM protein Munc-18-1 has been knocked-out, neurotransmitter release is completely abolished (Verhage et al., 2000). In contrast, residual fusion persists in synaptobrevin or SNAP-25 knockout mice, probably due to partial compensation by other SNARE isoforms (Martens and McMahon, 2008; Wojcik and Brose, 2007).

Synaptic vesicle exocytosis takes place at the AZ, with as little delay as 50 μ s upon the increase in Ca^{2+} concentration induced by action potential arrival (Südhof, 2004), indicating that this process is tightly regulated both in space and time². AZ proteins such as Munc-13s and RIMs are involved in the correct positioning of vesicles at release sites (see 1.2.3), whereas complexin (Reim et al., 2001) and synaptotagmin-1 (Fernandez-Chacon et al., 2001) are responsible for the precise timing of the Ca^{2+} -dependent component of release.

In spite of considerable efforts during the last two decades, the current understanding of synaptic vesicle exocytosis is far from complete. Many key players and interactions have been identified, but many others remain poorly understood and the exact sequence of events leading to neurotransmitter release is still debated. Furthermore, different release pathways may use different exocytosis mechanisms, and even different mechanisms may coexist in one pathway. The fast (synchronous) component of synaptic Ca^{2+} -dependent exocytosis is currently the best characterized and thought to consist on the following steps (Martens and McMahon, 2008; Südhof and Rothman, 2009) (Figure 3B):

1. Vesicles are targeted and attached to the AZ by unknown *tethering* factors, which could include the Munc-18-1/*closed* syntaxin-1 complex (Gulyas-Kovacs et al.,

¹ Even though the physiological relevance of kiss-and-run fusion has been intensely disputed, most authors currently agree that it is one of the main modes of endocytosis, together with the clathrin-mediated pathway (Harata, 2006; Rizzoli and Jahn, 2007)

² However, evidence for ectopic release has also been presented (Coggan et al., 2005)

- 2007) and/or the tripartite complex Rab-3/RIM/Munc-13 (Dulubova, 2005; Weimer et al., 2006) (see 1.2.3).
2. At the AZ, Munc-18-1 is bound to *closed* syntaxin-1, preventing the assembly of the SNARE complex (Dulubova et al., 1999). In the closed conformation of syntaxin-1 its H_{abc} domain, consisting on another three helices, is folded back into the helix containing the SNARE motif. Munc-18-1 stabilizes this arrangement by clasping the four helices together.
 3. When syntaxin-1 *opens*, the H_{abc} domain dissociates from the SNARE motif, which can now interact with SNAP-25 and synaptobrevin to form the core SNARE complex (Deak et al., 2009; Khvotchev et al., 2007). This interaction cannot take place in the absence of Munc-18-1, which remains bound to the H_{abc} domain upon syntaxin opening. At this stage, the vesicle is said to be *primed* for release.
 4. In primed vesicles, the SNARE complex is not yet fully assembled, but clamped in a metastable state by complexin.
 5. Upon action potential arrival, Ca²⁺ influx triggers a conformational change in synaptotagmin-1, which releases the complexin clamp and triggers fusion by binding to the SNARE complex and phospholipids. Thus, complexin in one hand suppresses spontaneous fusion by preventing the full assembly of the SNARE complex, and in the other enhances Ca²⁺-evoked exocytosis by keeping the complex ready for Ca²⁺-triggered synaptotagmin-1 action. This action also involves the creation of a AZ invagination that lowers the energy barrier for fusion (Hui et al., 2009).

The process follows similar steps in other exocytosis modes, but certain important details are different. For example, another, currently unknown, Ca²⁺ sensor is used in the slow (asynchronous) component of Ca²⁺-dependent exocytosis.

Using classical EM techniques, synaptic vesicles are often seen making direct membrane-to-membrane contact with the AZ. These vesicles are traditionally termed *docked*. However, in order to take into account the artifacts arising from conventional EM sample preparation, sometimes all vesicles within 30 nm from the AZ are defined as docked. In the classical model of exocytosis, vesicles are thought to be first tethered to the AZ, and then sequentially proceed to docking, priming and fusion. However, recent evidence has challenged this view, and currently there is no clear functional correlate for the morphological concept of docking. Furthermore, morphologically docked vesicles could actually be found in different functional states (Verhage and Sørensen, 2008). These considerations question the usefulness and validity of the concept of *docking*.

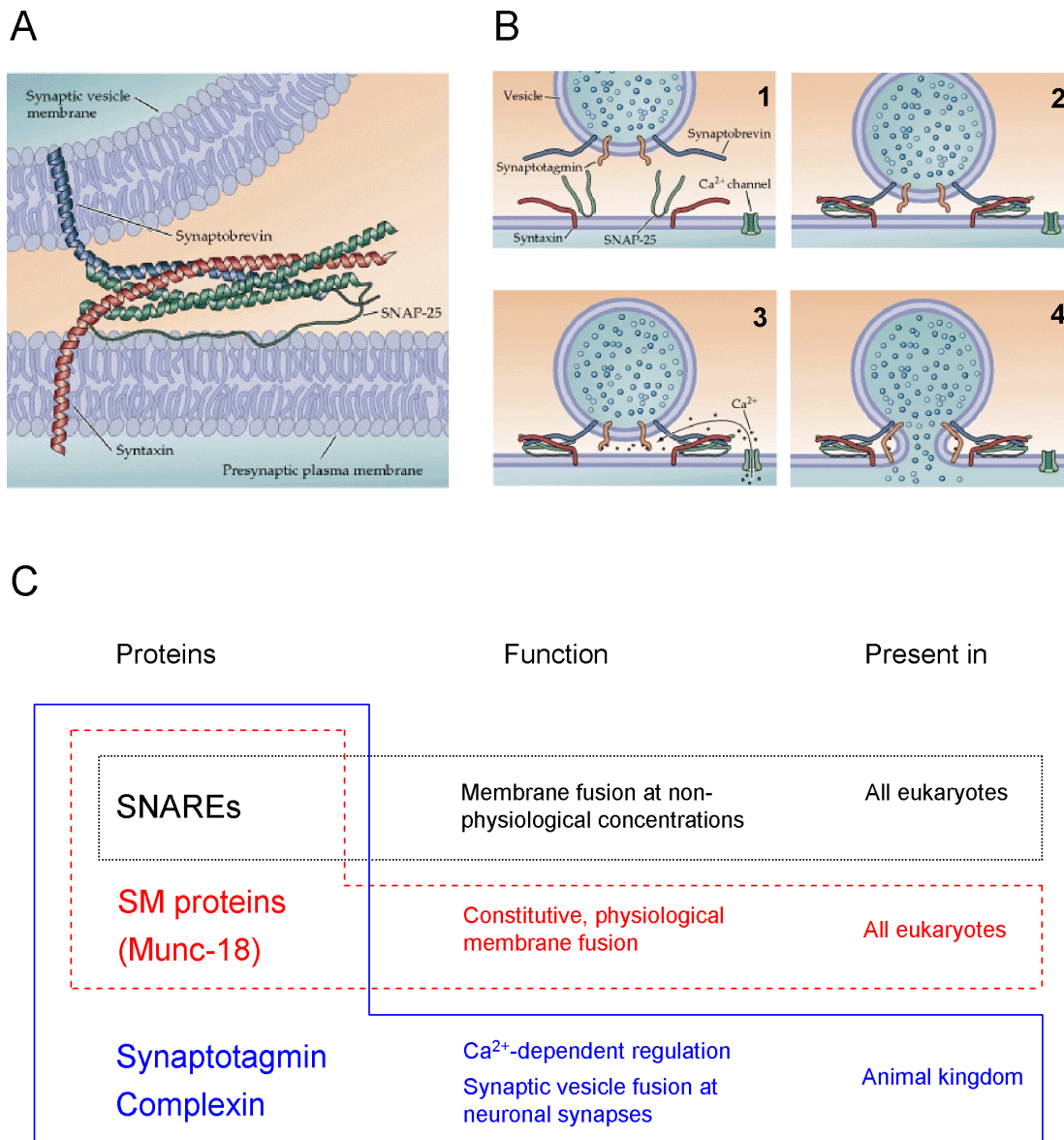


Figure 3 Synaptic vesicle release machinery. (A) Structure of the assembled core SNARE complex. (B) Proposed sequence of events underlying synaptic vesicle fusion. For simplicity, only SNAREs, synaptotagmin and Ca²⁺ channels are represented. (1) The vesicle is tethered to the cell membrane by unknown factors and the SNARE complex is not yet assembled. (2) Upon SNARE complex assembly the vesicle is primed for fusion. (3) Ca²⁺ binds to synaptotagmin, triggering (4) vesicle fusion (adapted from Purves et al., 2008). (C) Schematic representation of the functions of the proteins involved in synaptic vesicle fusion, ranked by sufficiency for fusion. SNAREs cause membrane fusion *in vitro*, but only at very high, non-physiological concentrations that lead to membrane rupture. Together with SM proteins (such as Munc-18-1 in mammals), they are responsible of physiological, constitutive membrane fusion in all eukaryotes. In synapses, this machinery is coupled to complexin and synaptotagmin to allow Ca²⁺-regulated vesicle fusion.

1.2.3 The presynaptic cytomatrix

Synaptic vesicles are embedded in a complex filamentous scaffold that organizes both the AZ and the synaptic vesicle cluster. Whereas the precise spatial arrangement of these structures is not yet known, several components of this presynaptic cytomatrix have been identified using biochemical techniques (Schoch and Gundelfinger, 2006; Wojcik and Brose, 2007).

The protein scaffold of the AZ plays a fundamental role in vesicle recruitment and exo- and endocytosis, as well as in regulating the changes in release during short and long term synaptic plasticity. Recently, it has been hypothesized that this AZ scaffold undergoes a profound remodeling upon synaptic activity (Hosoi et al., 2009; Wu et al., 2009). So far, only five protein families have been found to be enriched at the AZ in comparison to other neuronal compartments: RIMs, Munc-13s, Bassoon and Piccolo, ELKS/CAST/ERC and liprins- α . The AZ also contains proteins involved in vesicle fusion (SNAREs, Munc-18), cytoskeletal proteins (e.g. actin, tubulin), scaffolding proteins (e.g. CASK, Mint), voltage-gated Ca^{2+} channels or cell adhesion molecules (e.g. neurexin, cadherins). AZ proteins interact extensively with each other in this crowded environment, forming an interconnected network linked to synaptic vesicles.

RIMs have been hypothesized to play a central role in AZ organization because they bind directly or indirectly to many other synaptic proteins, such as Rab-3, Munc-13-1 or liprins- α (Südhof, 2004). As mentioned above, the tripartite complex Rab-3/RIM/Munc-13 has been proposed to act as a tethering factor that brings vesicles into proximity of the priming machinery (Dulubova, 2005; Weimer et al., 2006). RIM-1 α knockout mice are viable and show no major alterations in synaptic ultrastructure, but suffer from a 50% reduction in vesicle priming, impaired Ca^{+2} -dependend release and severe defects in short and long term plasticity leading to abnormal behavior (Schoch and Gundelfinger, 2006).

Genetic ablation of Munc-13s results in total arrest of neurotransmitter release due to priming defects (Augustin et al., 1999; Varoqueaux et al., 2002), and the differential expression of its isoforms controls short-term presynaptic plasticity (Rosenmund et al., 2002). Munc-13s priming action seems to rely on their ability to regulate SNARE complex assembly, probably via their interaction with tomosyn (Wojcik and Brose, 2007).

ELKS are necessary for localization of RIMs at the AZ and also take part in synaptic transmission (Kaeser et al., 2009; Takao-Rikitsu et al., 2004). Piccolo and Bassoon are structurally related and the largest of the AZ-specific proteins (420 and 530 kDa respectively). Piccolo is thought to provide a functional link between exo- and endocytosis, and Bassoon is implicated in synaptic assembly and functioning (Schoch and Gundelfinger, 2006). Liprins- α are also necessary for synapse formation and maintenance. Interestingly, recent research has also pointed out the importance of the synaptic adhesion molecules of the AZ in the regulation of the synaptic vesicle cycle (Gottmann, 2008).

Only a few proteins have been identified as organizers of synaptic vesicle clusters. Early biochemical and structural data (see 1.2.4) suggested that vesicles were linked

to each other and possibly to actin filaments via synapsin molecules (Hilfiker et al., 1999). Synapsins are the most abundant synaptic vesicle proteins, and are known to dissociate from membranes in a phosphorylation dependent manner. This fact led to a model in which synaptic stimulation would induce phosphorylation of synapsin, which would in turn dissociate from the vesicles and allow their mobilization towards the AZ. However, no causal relation could be established between synapsin dissociation and vesicle mobilization, and stimulation-induced mobilization was unaltered by the absence of synapsin (Gaffield and Betz, 2007). Some studies have suggested a role for α -synuclein (Murthy and De Camilli, 2003), Rab-3 (Südhof, 2004) or rabphilin (Gaffield and Betz, 2007) in vesicle clustering and/or mobilization, but no strong supporting evidence has been presented so far.

Thus, even though synapsins were the first synaptic vesicle proteins identified (De Camilli et al., 1983), their exact function is still unclear. Mutant mice lacking all three synapsin isoforms survive to adulthood, but display a decreased number of synaptic vesicles, neurotransmission deficits and dramatic changes in short-term plasticity, with different characteristics at excitatory and inhibitory synapses (Gitler et al., 2004). These findings indicate that synapsin might be needed to maintain vesicle integrity and/or mediate vesicle association with the AZ (Südhof, 2004).

Actin filaments are present around, rather than within, the synaptic vesicle cluster, indicating that they could play more of a *corralling* function avoiding vesicle dispersion into the axon (Cingolani and Goda, 2008). However, actin is not implicated in vesicle mobilization (Levitan, 2008). Actin has also been involved in synaptic vesicle recycling in lamprey reticular spinal synapses (Shupliakov et al., 2002), but the disruption of actin in hippocampal synapses does not have a major effect on recycling (Murthy and De Camilli, 2003).

1.2.4 Electron microscopy analysis of presynaptic architecture

The pioneering electron microscopy work on synapses in the 1950's (Estable et al., 1954; Robertson, 1953; Sjöstrand, 1953) provided definitive proof for the neuron doctrine by showing the discontinuity between pre- and postsynaptic terminals. Synaptic vesicles were first visualized in the fifties (De Robertis and Bennett, 1954; Palade and Palay, 1954), and were hypothesized to mediate the observed quantal nature of neurotransmitter release (Del Castillo and Katz, 1954). Later studies showed (*docked*) vesicles making direct contact with the AZ (Palay, 1956) and correlated neurotransmitter release with exocytosis (Heuser et al., 1979).

For these studies, EM samples were chemically fixed, dehydrated and heavy metal-stained. In such preparations, the AZ was reported to consist on a regular arrangement of electron densities termed the *presynaptic grid* (Gray, 1963; Pfenninger et al., 1969), and later work using similar techniques supported those observations (Phillips et al., 2001). However, these sample preparation protocols are known to induce aggregation and other artifacts (see 2.2), and such structures were not observed in cryo-fixed samples either by etching (Landis et al., 1988) or tomographic techniques (Siksou et al., 2007). Electron tomography (ET) has also been successfully applied to study the

AZ of chemically fixed ribbon synapses (Lenzi et al., 1999) and frog neuromuscular junctions (Harlow et al., 2001).

The filamentous matrix of the presynaptic terminal was first visualized by means of deep-etch, quick-freeze electron microscopy (Gotow et al., 1991; Hirokawa et al., 1989; Landis et al., 1988) (Figure 4A). These three studies reported the existence of filaments connecting synaptic vesicles to the AZ and short strands linking vesicles to each other or to longer filaments, but the morphology and organization of such structures was different in each case. It was proposed that the short strands consisted on synapsin (Hirokawa et al., 1989). More recent work (Siksou et al., 2007) (Figure 4B) also described an extensive network of filaments, but discarded a unique role of synapsin in their formation. However, the use of dehydrated and heavy metal-stained samples casts doubts on some of the structures observed in these studies, and consequently a clear picture of the organization and composition of the presynaptic cytomatrix is still missing.

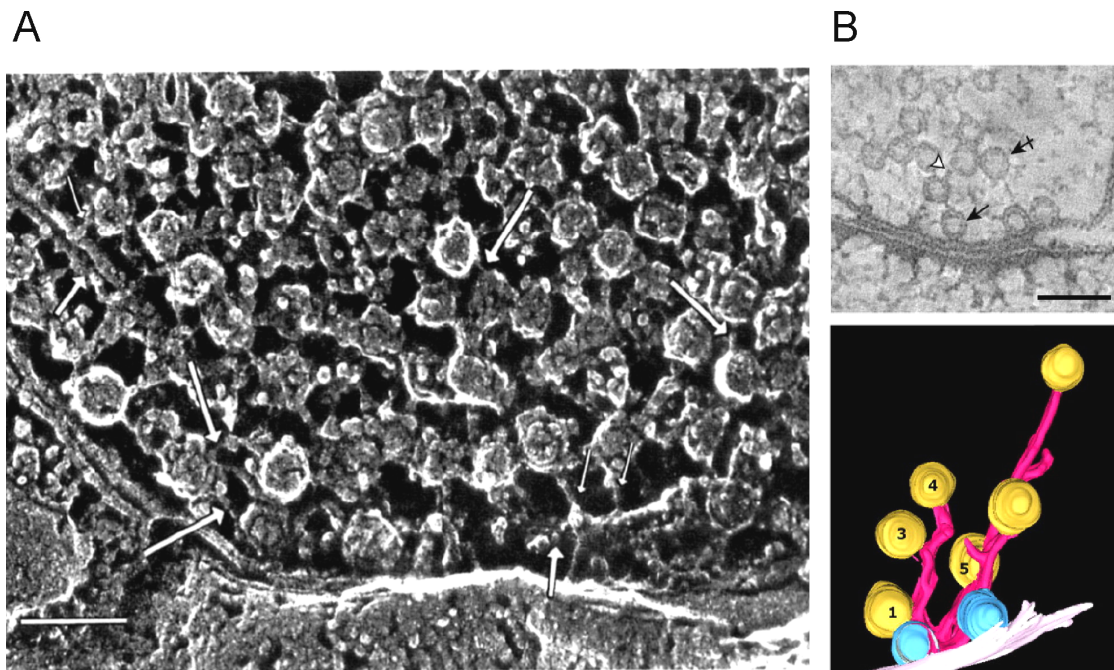


Figure 4 (A) Presynaptic terminal of a rat cerebellar mossy fiber visualized by quick-freeze, deep-etch EM. Short linking strands (thin short arrows) between synaptic vesicles and microtubules, and between synaptic vesicles (longer thick arrows) can be seen (adapted from Hirokawa et al., 1989). (B) Presynaptic terminal of the stratum radiatum of the rat hippocampal CA1 area prepared by freeze-substitution. (Up) Tomographic slice showing filaments linking vesicles to each other (white arrowhead) and docked vesicles making direct contact with the active zone (black arrow). (Down) 3D visualization of the long filaments (pink) that link synaptic vesicles (yellow) to the AZ (light pink). Docked vesicles are shown in blue (adapted from Siksou et al., 2007). Scale bars: 100 nm.

2 Electron Microscopy and Tomography

2. Electron Microscopy and Tomography

Electron microscopes take advantage of the short wavelength of electrons ($\sim 10^{-3}$ nm for the usual range of accelerating voltages) to allow imaging of biological and other specimens up to sub-nanometer resolution. The current section covers the basic aspects of electron microscopy relevant to this work.

2.1 Transmission Electron Microscopy

2.1.1 Components of transmission electron microscopes

The first electron microscope was built by Ruska and Knoll in 1931, and the first serially produced, commercial unit was launched by Siemens eight years later (Ruska, 1986). It consisted of a vertical column hosting an electron source, three electron lenses (condenser, objective and projector), a specimen chamber and a photographic device on the image plane of the system. High vacuum was established in the column to allow the free propagation of electrons. In order to withstand the vacuum, biological samples had to be chemically fixed and dehydrated. Current electron microscopes offer great advances compared to the early models, but still share the same basic design and working principles (Figure 5) (Reimer and Kohl, 2008; Williams and Carter, 1996):

a) Electron gun

The electron gun produces and accelerates the electrons. Three types of electron guns are used in modern microscopes: thermoionic, Schottky emission and field-emission guns (FEGs). The data presented in this work was collected in two FEG-equipped, 300 kV microscopes: CM300 (Phillips, The Netherlands) and Tecnai Polara (FEI, The Netherlands). In spite of their higher cost, FEGs are the technology of choice as they produce an electron beam with high brightness and high spatial and temporal coherence. These guns consist on a needle-shaped W cathode and two anodes. The first anode has a positive potential of few kV with respect to the tip, the so-called *extraction voltage*, which allows the electrons to tunnel out of the tip. The second anode further accelerates the electrons up to 300 kV.

b) Illumination system

The illumination system comprises the condenser lenses and their respective apertures. Most electron lenses are magnetic, basically consisting of a magnetic coil that generates a strong magnetic field on a circular pole piece. The electrons travel through the central gap of the pole piece and are deflected by its magnetic field, in a manner similar to the deflection of light through optical lenses. Apertures are openings that exclude a certain fraction of the electrons in order to improve imaging conditions.

The above-mentioned microscopes were equipped with two condenser lenses, C1 and C2. The settings of C1 determine the *spot size* or demagnification of the electron source onto the specimen. The current through the C2 lens (*C2 intensity*) controls the size of the illuminated area on the specimen. This size is also limited by the C2 aperture, which acts to reduce the electron current and the convergence of the beam. In order to make the electron beam parallel to the axis of the condenser and objective system, two sets of deflection coils (gun shift/tilt and beam shift/tilt coils, situated above and below the condenser lens system respectively) are used.

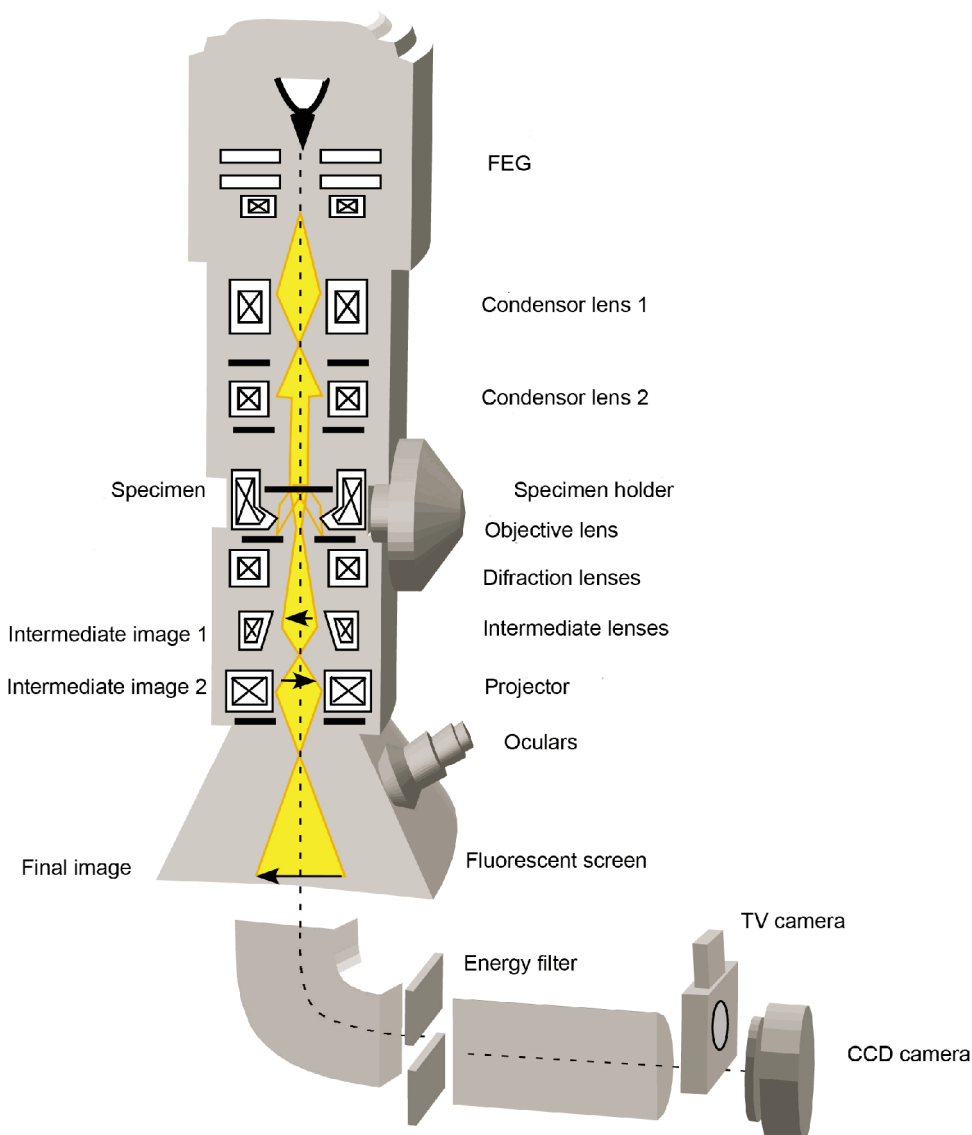


Figure 5 Schematic representation of the components of the Phillips CM 300 TEM in Martinsried (Schweikert, 2004).

c) Imaging system

The imaging system is formed by the objective, diffraction, intermediate and projector lenses and the objective aperture. The imaging system produces a magnified image that can be observed at the fluorescent screen of the microscope or captured by a detector.

When the electrons reach the sample, some of them are transmitted unscattered, while other are scattered by interactions with the sample, giving rise to image contrast (see 2.1.2). In the CM300 and Polara microscopes, the sample is sandwiched between the two coils of the objective lens, which produces a pre-magnified image (20-50 x). The image is further magnified by the intermediate and projector lenses to the final desired value (typically 20,000- 40,000 x for this work). In this *imaging mode*, the object plane of the intermediate lens coincides with the image plane of the objective lens. The objective aperture can be inserted in the back focal plane of the objective lens to remove electrons diffracted at high angles, improving image contrast. Alternatively, in *diffraction mode*, the back focal plane of the objective lens acts as the object plane of the intermediate lens, and the diffraction lens is used to image the diffraction pattern.

d) Image detection system

For direct viewing, electron microscopes are normally equipped with a fluorescent screen in the image plane of the optical system. The fluorescent coat of this screen produces light upon impact of electrons.

Traditionally EM images were recorded in photographic plates. This recording medium is still widely used, but CCD (*charged coupled device*) cameras are increasingly popular, as they offer comparable performance, superior versatility and immediate image access, making possible the automation of data collection. CCD cameras consist on a scintillator coupled to a MOS/CMOS chip via fiber glass. The electrons hit the scintillator and are converted into photons, which then enter the fiber glass and arrive to the CCD chip, where they are transformed into an electronic signal that can be read and transmitted to a computer.

Often, before reaching the CCD, the beam goes through a *post-column energy filter*, a magnetic prism that deflects the electrons in different angles according to their energy. For this work, the energy filter was operated in the so-called *zero-loss mode*, which only allows electrons that suffered minimal energy loss (~ 10 eV) to reach the CCD, thus enhancing image quality (Grimm et al., 1996). The energy filter introduces an additional magnification factor of 1.9 for 23,000 x magnification in CM300 and 1.3 for 34,000 x magnification in Polara (magnifications that were used almost in all cases for this work).

e) Other TEM systems

Vacuum system. High vacuum ($\sim 10^{-5}$ Pa) needs to be established in the microscope column to avoid electron scattering from gas particles. Furthermore, FEGs are extremely sensitive to surface contamination and require even higher vacuum ($\sim 10^{-9}$ Pa). Thus, thanks to a complex system of pumps, ambient pressure on the sample is reduced by ten orders of magnitude upon insertion in the column (atmospheric pressure $\sim 10^5$ Pa). Cryogenic shields, connected to an external supply of liquid-N, further reduce in-column contamination in CM300 and Polara.

Sample stage. EM samples are typically mounted on a metallic grid of ~ 3 mm in diameter. TEMs are equipped with a sample-loading system designed to properly position the grid inside the objective lens, allow lateral movement of the sample and minimize drift and mechanical instabilities. For cryoelectron tomography, the sample stage is equipped with a computerized goniometer that allows rotation along the holder axis, while the temperature is kept below -140° C (liquid-N/He cooling) to avoid sample devitrification. CM300 is designed for the use of cryo side-entry holders, whereas in the Polara the specimen is held in the column by a mechanism independent of the insertion system, providing greater thermal and mechanical stability.

2.1.2 Image formation: Phase contrast

The interaction with the atoms of the sample results in a change of trajectory (*scattering*) of some of the incident electrons (Frank, 2006; Reimer and Kohl, 2008). Thus, darker and lighter areas are created in the image plane, giving rise to *image contrast*³. Scattering can be elastic or inelastic, depending on whether or not the kinetic energy of the incident electron is conserved. TEMs can provide high resolution because elastic scattering is a highly localized interaction between the incident electrons and the region occupied by the screened Coulomb potential of the nucleus. Inelastic scattering is much less localized⁴, and therefore it does not give rise to high resolution information. Inelastically scattered electrons have a much narrower angular distribution than those scattered elastically, and thus most of them go through the objective aperture. Moreover, inelastic scattering dominates for the light atoms of biological materials (Reimer and Rossmessemer, 1989)⁵, and energy filtering devices may become necessary to remove the inelastic component (see 2.1.1).

The extent of the scattering is usually quantified by the so-called *mean free path*, which measures the mean distance that an electron can travel without being scattered in a certain medium. For vitreous ice at liquid-N temperature and an accelerating voltage of 300 kV, the elastic and inelastic mean free paths are 450 and 180 nm respectively (Schweikert, 2004).

³ *Contrast* is defined as the relative difference in intensity between two neighboring areas that renders them distinguishable.

⁴ The main mechanisms contributing to inelastic scattering are plasmon and interband excitations.

⁵ $\frac{\sigma_{in}}{\sigma_{el}} \approx \frac{20}{Z}$, where σ_{in} and σ_{el} are respectively the inelastic and elastic cross-sections and Z the atomic number

Elastic scattering results in a phase shift of the incident wave. Assuming that the wave travels in the z direction, the phase shift is

$$\phi(\vec{r}) = \int C(\vec{r}, z) dz$$

where $\vec{r} = (x, y)$ and $C(\vec{r}, z)$ is the 3D Coulomb potential distribution within the object. Therefore, an incoming plane wave $\psi_0 = \exp(ikz)$, where k is the wave number, is modified according to

$$\psi = \psi_0 \exp[i\phi(\vec{r})]$$

It is often assumed that the interaction between the incident beam and the object is weak (*weak phase object approximation*). Therefore $\phi(\vec{r}) \ll 1$ and we can write

$$\psi = \psi_0 \left[1 + i\phi(\vec{r}) - \frac{1}{2}\phi(\vec{r})^2 + \dots \right]$$

This expression is normally truncated after the second term, implying that the wave that exits the object can be expressed as the interaction of the unscattered wave (ψ_0) and a much smaller scattered wave with a $\pi/2$ phase shift (following term).

The Fraunhofer approximation of the diffraction theory assumes that the observer is far away from the object and close to the optical axis (conditions that always hold in transmission electron microscopes). In this approximation, a Fourier transform of the object is formed in the back focal plane of the objective lens:

$$\psi_{bf}(\vec{k}) = \mathfrak{F}\{\psi(\vec{k})\}$$

where \vec{k} is the spatial frequency. However, the defocusing and the lens aberrations (normally only the objective lens is considered) introduce an additional phase shift given by $\gamma(\vec{k})$:

$$\psi_{bf}(\vec{k}) = \mathfrak{F}\{\psi(\vec{k})\} \exp[i\gamma(\vec{k})]$$

In polar coordinates ($k = |\vec{k}|$, $\phi = \arctan(k_x, k_y)$):

$$\gamma(k, \phi) = \frac{\pi}{2} [C_s \lambda^3 k^4 - 2\Delta z \lambda k^2]$$

where C_s is the spherical aberration coefficient and Δz the defocus (this formula assumes that axial astigmatism has been corrected). After going through the objective aperture, an image is formed at the image plane of the objective lens. This image is the inverse Fourier transform of the wave in the back focal plane:

$$\psi_i(\vec{r}) = \mathfrak{F}^{-1}\left\{\mathfrak{F}\{\psi(\vec{k})\} O_a(\vec{k}) \exp[i\gamma(\vec{k})]\right\}$$

$$O_a(\vec{k}) = \begin{cases} 1 & \text{for } k = \theta / \lambda \leq \theta_1 / \lambda \\ 0 & \text{elsewhere} \end{cases}$$

where θ_1 is the angle corresponding to the radius of the objective aperture. The observable magnitude is the intensity distribution of ψ_i :

$$I(\vec{r}) \sim |\psi_i(\vec{r})|^2$$

And under the weak phase object approximation, it can be shown that

$$\Im\{I(\vec{r})\} \propto \sin \gamma(\vec{k})$$

The function $\sin \gamma(\vec{k})$ is known as the *phase contrast transfer function* (CTF) and represents the influence of the settings and characteristics of the microscope (especially the objective lens) in the observed image. The CTF oscillates, implying different transmittance for different spatial frequencies, with some frequencies that are not transmitted at all (zeros of the CTF, Figure 6). Thus, the observed image is not a completely faithful representation of the actual object.

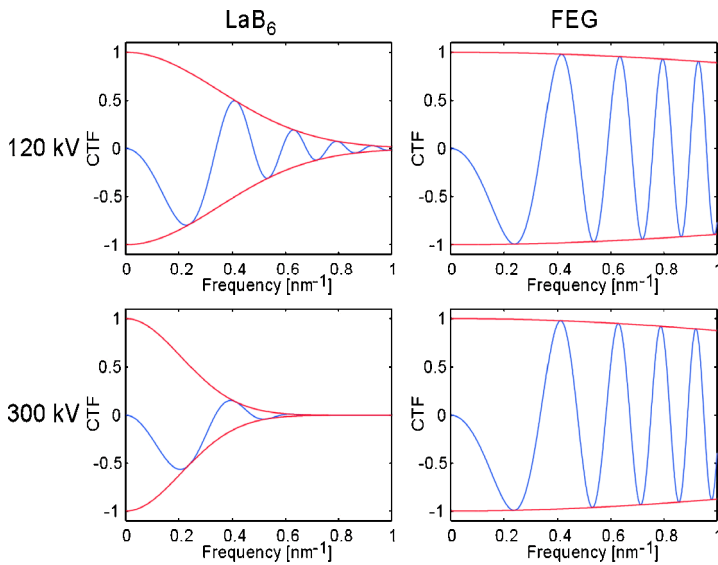


Figure 6 Theoretical CTFs (blue) and their envelopes (red) for LaB6 TEMs (left column) and FEG microscopes (right column), for acceleration voltages of 120 kV (top row) and 300 kV (bottom row). Additionally: illumination aperture $\alpha = 0.2$ mrad and $\alpha = 0.02$ mrad for LaB6 and FEG, respectively; energy width of the incident beam $E = 3$ eV and $E = 0.8$ eV for LaB6 and FEG, respectively; defocus values $-2.6 \mu\text{m}$ at 120 kV and $-4.5 \mu\text{m}$ at 300 kV, chosen such that the first zero of the CTF occurs at $(3 \text{ nm})^{-1}$ (Lučić et al., 2005a).

Furthermore, the previous expressions have been developed assuming monochromatic illumination and perfect coherence of the electron source. In reality, electron sources have a certain energy spread and coherence is limited due to finite source size. These two factors result in an envelope function $E(k)$ that dampens the CTF at higher frequencies. Thus

$$\Im\{I(\vec{r})\} \propto E(\vec{k}) \sin \gamma(\vec{k})$$

and $E(k) = E_i(k)E_e(k)$, with $E_i(k)$ representing the effect of the partially coherent illumination and $E_e(k)$ accounting for the finite energy spread. In microscopes equipped with a FEG, the value of both components of the envelope function remains close to unity for high spatial frequencies, effectively not limiting the resolution (O'Keefe, 1992) (Figure 6). However, it should be mentioned that other elements, such as the settings of the C1 condenser lens may also influence the envelope function.

In the usual defocus range, the value of the CTF is very small for low spatial frequencies, and thus it acts as a high-pass filter. It also functions as a low-pass filter (limiting the resolution) because image interpretation beyond the first zero is complicated due to the oscillating contrast, unless algorithms for CTF correction are applied. In the case of sharply declining envelope functions, high frequencies are not transmitted at all. Therefore, the main effect of the CTF is a band-pass filtering.

Thus, even though the de Broglie wavelength of electrons accelerated at 300 kV is $\sim 0.020\text{\AA}$, the imperfections of the instruments allowed sub-angstrom resolution only in very few cases (Batson et al., 2002). For biological specimens, resolutions of a few angstroms have been achieved by crystallographic (Gonen et al., 2005) or single particle approaches (Yu et al., 2008).

In this work, biological specimens preserved in vitreous ice (see 2.2) were examined. In such samples, even though phase contrast is the main mechanism contributing to image formation, it is not the only one. For the expressions derived above, it was assumed that all interfering waves had the same amplitude. However, some electrons are “subtracted” from contributing to phase contrast, either because they are elastically scattered at high angles and thus removed by the objective aperture, or because they are inelastically scattered. This implies that the amplitudes of the interfering waves change locally, giving rise to *amplitude contrast*. Thus, the generalized expression of the Fourier transform of the intensity in the image plane becomes

$$\Im\{I(\vec{r})\} = A(\vec{k}) \sin \gamma(\vec{k}) + B(\vec{k}) \cos \gamma(\vec{k})$$

where $A(\vec{k})$ and $B(\vec{k})$ represent the respective contributions of phase and amplitude contrast. For unstained specimens preserved in a thin layer of vitreous ice, the contribution of the amplitude term is in the order of 7% at 100 kV, 5% at 200 kV and 4% at 300 kV (Baker and Henderson, 2010; Smith and Langmore, 1992; Toyoshima and Unwin, 1988), whereas for negatively stained samples on a carbon support film it may reach 35% (Erickson and Klug, 1971). It is important to note that the

introduction of the $\cos \gamma(\vec{k})$ term implies non-zero intensity for low frequencies ($k \approx 0$), mitigating the high-pass filtering effects of the CTF.

2.2 Sample preparation

As previously mentioned, biological samples cannot withstand the high vacuum present in the column of the EM in their native, fully hydrated state at room temperature. Furthermore, the samples need to be thin (normally $<1\mu\text{m}$), as the penetration depth of electrons is limited. “Conventional” preparation procedures for EM focus in stabilizing dehydrated biological structures (Dawes, 1971). Usually, cells or tissues are chemically fixed by glutaraldehydes and osmium tetroxide, which cross-link biomolecules and prevent collapse and degradation after cell death. Then, the water in the sample is substituted by an organic solvent (*dehydration*), such as acetone or ethanol, which is subsequently replaced by a resin (*infiltration*). Once the tissue has been infiltrated, the resin is polymerized, resulting in a solid block that can be sliced into sections of a few hundred nanometers. Even though osmium tetroxide is already an electron dense compound, additional heavy metal stains might be used before (*en-bloc* staining, using uranyl acetate) or after infiltration (*poststaining* with uranyl acetate or lead citrate) in order to enhance contrast. In these samples amplitude contrast is the main mechanism of image formation (Hawkes, 2005).

Such preparation procedures are relatively simple, but may result in severe artifacts. In first place, chemical fixation and dehydration are harsh treatments causing structural rearrangements, aggregation and leakage of cytoplasmic components. Also, since stain molecules are visualized instead of the biological structures, micrograph interpretation might be biased by the non-uniform association of the stain to the biological material (McIntosh, 2001). In fact, the interactions between staining agents and biological structures are poorly understood, and often a mixture of negative and positive staining (staining of the structure outline and staining of the structure itself, respectively) is found, further complicating the interpretation of the data.

The development of physical fixation by rapid freezing as an alternative to chemical methods constituted a major breakthrough, as it provided optimal structural preservation (Taylor and Glaeser, 1974). Biological structures are frozen at extremely high cooling rates ($\sim 10^5$ K/s) that achieve water vitrification at temperatures below -140°C . In this way freezing is fast enough to avoid ice crystal formation, which would lead to toxic solute effects and cell damage, as crystalline ice occupies larger volume than liquid water. In vitrified frozen-hydrated samples the arrangement of water molecules is similar to that of the liquid phase, and therefore the artifacts introduced are minimal and the structures are preserved in a close-to-life state (Dubochet et al., 1988).

Samples thinner than $10\mu\text{m}$ can be vitrified by rapid immersion in a cryogen, such as liquid ethane cooled at liquid-N temperature (77K), in a procedure known as *plunge freezing* (Dubochet et al., 1988). This method is useful for vitrification of samples in suspension, such as protein complexes or sub-cellular fractions, as well as for adherent cells grown directly on EM grids. The basic plunge freezing setup consists

on a small liquid ethane dewar immersed in a bath of liquid-N, and a set of tweezers clamped on a mechanical arm. An EM grid containing the sample in aqueous solution is mounted on the tweezers, the excess liquid is blotted away in a few seconds with the aid of filter paper, and the grid is plunged into the cooled liquid ethane. The grid is then transferred to liquid-N and placed into a special gridbox for storage or direct insertion into the EM. Dedicated holders can keep the grid at temperatures below -140°C inside the EM column, allowing the visualization of vitrified frozen-hydrated samples in EM.

Due to the poor thermal conductivity of water, the cooling rate achieved by plunge freezing is not sufficiently high for thicker specimens, such as blocks of tissue. Thus, in order to avoid ice crystal formation, high-pressure freezing (HPF) becomes necessary. In HPF machines the sample is inserted into a small holder, which is subjected to 210 MPa and cooled by jets of liquid-N at the same time. The high pressure prevents ice crystal formation, and allows the vitrification of specimens up to 200 μm in thickness (Studer et al., 2008).

For EM observation of fully hydrated, high-pressure frozen samples *cryosectioning* becomes necessary. This very delicate procedure consists on obtaining thin (50-100 nm) sections of a frozen sample using a diamond knife mounted on a cryomicrotome at liquid-N temperature. Cryosections suffer from severe compression⁶, knife marks caused by irregularities on the knife edge, cracks, crevasses and chatter. However, careful a selection of the sectioning parameters can reduce to some extent these artifacts and render sections amenable for EM observation (Al-Amoudi et al., 2005)⁷.

2.2.1 Radiation damage and noise

Naturally, vitrified frozen-hydrated samples also present drawbacks. In first place, alterations might be introduced during vitrification. For plunge frozen samples, the evaporation of buffer from the sample deposited on the EM grid prior to freezing can cause an increase in solute concentration and temperature changes (Stewart and Vigers, 1986). However, this problem can be circumvented by the implementation of an environmental chamber for the plunging device. Also, the mechanical stress induced by blotting might cause flattening or damage of cellular structures. On the other hand, only very small amounts of sample can be loaded into HPF holders, requiring invasive dissection in the case of tissue or substrate detachment in the case of adherent cells. The use of cryoprotectants might also become necessary for vitrification of samples especially rich in water, such as nervous tissue (Zuber et al., 2005, see 4.1.4). It is also important to note that the handling of vitrified specimens

⁶ Plastic sections are usually floated in a liquid surface to permit surface tension forces to restore the sections to almost their original dimensions after being compressed during cutting. However, this process is not possible for cryosections that must remain at all times at liquid-N temperatures.

⁷ After HPF it is also possible to dehydrate the sample, stain it with heavy metals and embed it in plastic for EM observation at room temperature. This procedure is known as *freeze-substitution*, and combines improved structural preservation by avoiding chemical fixation with the convenience of handling and imaging samples at room temperature (Murk et al., 2003). However, dehydrated and stained freeze-substituted samples still suffer from important artifacts (Al-Amoudi et al., 2004).

needs great care, as they must be kept at liquid-N temperature at all times. Thus, special (and costly) sample holders and transfer devices need to be used, and microscope design must allow cryo-imaging without significant contamination.

But the major challenge posed by vitrified samples is their high sensitivity to radiation damage by the electron beam. Inelastic scattering events break chemical bonds, leading to the formation of very reactive free radicals that initiate harmful secondary reactions. Even though this process does not depend on the temperature, the real extent of the damage (given by the loss of mass and diffusion of free radicals) is very much reduced by cooling the specimen to liquid-N temperatures (77 K). Further cooling to liquid-He temperatures (~4 K) did not prove advantageous for cryo-EM (Comolli and Downing, 2005; Iancu et al., 2006).

Consequently, in vitrified samples the electron dose per micrograph is constrained to very low values, resulting in shot noise that reduces the signal-to-noise ratio (SNR)⁸. The imperfections of CCD cameras also increase the noise level, which is in turn the ultimate limitation for resolution, rather than the instrument itself. The dose used in data acquisition depends on the desired resolution: for electron crystallography secondary and tertiary structures should be preserved, and electron dose should be consequently kept below $10 \text{ e}^-/\text{\AA}^2$ (Henderson, 1995). For cryo-electron tomography (cryo-ET), where resolution is not better than a few nanometers, doses of 50-100 $\text{e}^-/\text{\AA}^2$ are acceptable. Excessive doses result in major damage manifested by the onset of bubbling (Heide and Zeitler, 1985).

2.3 Cryo-Electron Tomography

Tomographic techniques provide a three-dimensional reconstruction of the object of study from a series of two-dimensional images. In the case of electron tomography, the sample is rotated under the electron beam by the stage goniometer, and images are recorded at specified angles (forming a *tilt series*). To a very good approximation, these images are 2D projections of the object (Hawkes, 2005), and can be computationally combined into a faithful 3D reconstruction (Figure 7) (Radon, 1917). Furthermore, the *dose fractionation theorem* guarantees that, if a certain electron dose is distributed over several projections, the voxels of the resulting reconstruction have the same statistical significance as the pixels of a single image recorded with the same total dose (Hegerl and Hoppe, 1976; McEwen et al., 1995).

Many decades after Radon's work, the first three-dimensional structures were obtained by EM (Derosier and Klug, 1968; Hart, 1968), while early tomographic attempts were presented a few years later (Hoppe et al., 1974). However, ET performed manually was a cumbersome operation that usually required an excessive electron dose. These difficulties were overcome in the 90's with the advent of computer-controlled microscopes equipped with CCD cameras, allowing the

⁸ $SNR = \frac{\sigma_S^2}{\sigma_N^2}$, where σ_S^2 and σ_N^2 are respectively the variance of signal and noise. The SNR is a

function of the spatial frequency: $SNR = SNR(\vec{k})$

implementation of automated data acquisition schemes (Dierksen et al., 1992; Koster et al., 1992) that could be successfully applied to vitrified specimens (Dierksen et al., 1993; Grimm et al., 1997). Nowadays, cryo-electron tomography is a powerful technique for cellular investigations, as it combines optimal sample preservation with 3D structural information.

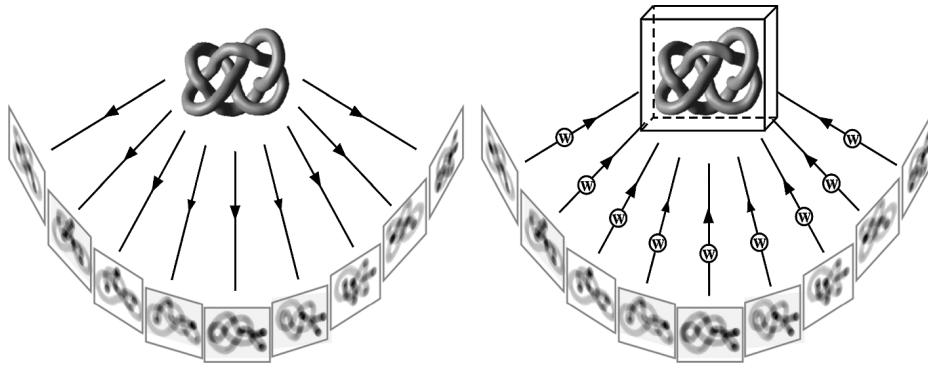


Figure 7 Principle of tomography. (Left) Projections images from an object are collected at different angles. (Right) A three-dimensional reconstruction is obtained usually by weighted (W) back-projection (Lučić et al., 2005a).

2.3.1 Automated data acquisition

For cryo-ET, due to the mechanical instabilities of the goniometer and the radiation sensitivity of the specimen, automated data acquisition procedures must fulfill the following criteria: i) the object of interest must remain in the field of view throughout the whole tilt series, ii) all images must be recorded under comparable imaging conditions and iii) the total electron dose must be kept under tolerable limits (*low dose* mode). These conditions are usually implemented in three basic steps, normally performed at every tilt angle:

1. Tracking: a very low dose image is recorded to determine and correct the lateral displacement of the specimen, by comparison with the image recorded at the previous tilt angle.
2. Autofocus: image defocus is determined from the relative displacement of the object measured in two micrographs acquired at different beam tilts (Koster et al., 1989; Ziese et al., 2003).
3. Exposure: recording of the projection image.

For further reduction of beam damage, the tracking and focusing operations can be performed at a certain distance along the tilt axis from the exposure spot. Also, the development of more sophisticated and stable TEM stages, such as that of the Polara microscope, reduces the need for tracking and focusing at every tilt angle as shifts during acquisition are much smaller.

If all projections were recorded with the same electron dose, images at high tilt angles would have lower intensity because of the effective increase of sample thickness in the direction of the beam. Therefore, a compensating factor of $1/\cos\alpha$ is commonly introduced for the exposure time, where α represents the tilt angle (this correction is derived from geometrical considerations of slab-shaped samples).

2.3.2 3D reconstruction

In order to correct for the imperfections of the tracking procedure, the recorded projections need to be *aligned*, i.e. brought to register in a common reference system. Usually small gold fiducial particles are deposited on the sample, so that their positions can be tracked throughout all projections either manually or automatically. Thus, the positional shifts of each projection with respect to a reference projection are measured and corrected. Some marker alignment routines can also correct for rotation or magnification changes that might have occurred during acquisition (Mastronarde, 2005). Alternatively, the alignment can be performed by cross-correlation algorithms that compare each image with the next. These algorithms are more sensitive to the high level of noise of cryo-ET projections, but do not suffer from potential irradiation-induced displacements of the fiducial markers (Brandt, 2005).

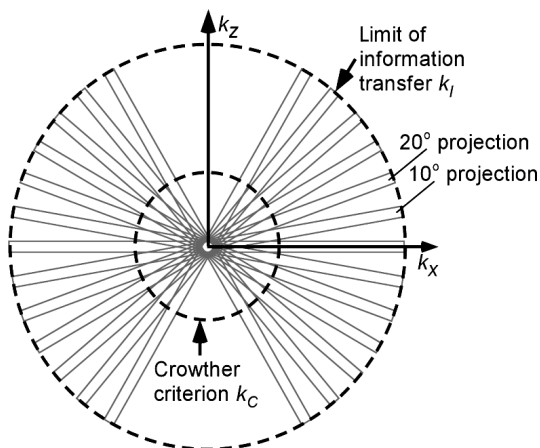


Figure 8 Sampling of the Fourier space. A projection of an object with thickness d corresponds to a central slice of thickness $1/d$ in Fourier space. Consequently, the three-dimensional information of the specimen (outside of the missing wedge) is gathered homogeneously only up to frequency k_c (Lučić et al., 2005a).

Aligned projections can be merged into a single volume using different algorithms. Even though the most commonly used reconstruction methods work in the real space, it is conceptually useful to analyze this problem in the Fourier space. The Fourier transformation of a projection corresponds to a central slice of the Fourier transformation of the 3D reconstruction. The thickness of this slice is $1/d$, where d is the size of the object. As can be seen in Figure 8, this fact carries the following implications:

- i) spatial frequencies are not evenly sampled, with higher frequencies being underrepresented
- ii) the angular increment between projections determines the extent of the frequency sampling (k_c)

- iii) due to the tilting geometry, some regions of the Fourier space are not sampled at all
- iv) no information is effectively transmitted beyond a certain frequency k_l

The design of current specimen holders limits the tilt range to $\pm 70^\circ$. This implies that certain directions are left unsampled and a *missing-wedge* of information in the Fourier space is created (Figure 9), causing anisotropic resolution (Midgley and Weyland, 2003). Assuming perfect alignment, the resolution along the tilt axis (r_x) is the resolution of the projections. For the direction perpendicular to the tilt axis, the resolution (r_y) also depends on the sampling strategy, as summarized by the Crowther criterion (Crowther et al., 1970):

$$r_y = \frac{\pi d}{N} = d \Delta \alpha$$

where N represents the number of projections, d the size of the object and $\Delta \alpha$ the angular increment. In practice, the tilt angle should not be smaller than $1-1.5^\circ$ in order to have projections with sufficient electron dose for a successful alignment and keep series recording times within reasonable limits. Also, this relation was derived for cylindrical specimens perpendicular to the tilt axis and for a constant tilt increment, and therefore its validity for cellular specimens of poorly defined size is limited. Finally, elongation occurs in the direction of the electron beam due to the missing-wedge of information. Thus

$$r_z = r_y e_{yz}$$

$$e_{yz} = \sqrt{\frac{\alpha_{\max} + \sin \alpha_{\max} \cos \alpha_{\max}}{\alpha_{\max} - \sin \alpha_{\max} \cos \alpha_{\max}}}$$

where α_{\max} is the maximum tilt angle. In conclusion

$$r_x \neq r_y \neq r_z$$

Therefore, the resolution is not well defined in electron tomography, and no mathematical tools to measure it reliably have been developed yet. So far only estimates can be obtained (Cardone et al., 2005; Penczek, 2002; Unser et al., 2005), giving values in the order of 5 nm for cryo-electron tomograms.

More elaborated tilting geometries, such as double-axis tilting (Penczek et al., 1995) (Figure 9), can reduce the amount of missing information and thus lead to a more faithful reconstruction. However, double-axis cryo-ET cannot yet be performed routinely, as it presents important technical difficulties.

The most common reconstruction algorithm in ET is the *weighted back-projection* (WBP), where the projections are projected back to form a three-dimensional reconstruction (Figure 7). In order to compensate for the non-uniform frequency sampling, different weighting functions can be applied. In the case of *analytical* weighting, the weight is proportional to the frequency, resulting in an artificial boost

of high frequency information (and noise). In *exact* weighting, the sampling density of the Fourier space is estimated according to the size of the object. This is normally not a well defined parameter, and consequently this scheme should be used with caution.

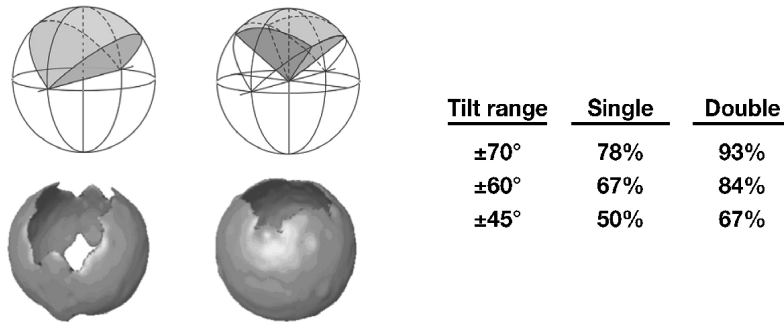


Figure 9 Single- and double-axis tilting. (Up) Portions of the Fourier space not sampled due to the limited tilt range. In single-axis tilting (left) and double-axis tilting (right) a “missing wedge” and in a “missing pyramid” are respectively formed. (Down) Simulated reconstructions of a hollow sphere with the tilting schemes from above. The table contains percentage of the Fourier space covered for different tilting schemes (Lučić et al., 2005a).

In this work, the simultaneous iterative reconstruction technique (SIRT, Gilbert, 1972) was also used. In SIRT, the reconstruction is seen as an optimization problem. Initially, a reconstruction is performed by unweighted back-projection. New projections are obtained from this volume and compared to the original projections. The algorithm minimizes the differences between them over several iterations, which normally require much more computer power than WBP. As no weighting is applied, in these reconstructions low frequencies are represented more fairly.

2.3.3 Tomogram analysis

Due to the wealth of information contained in cryo-electron tomograms and their low SNR, data interpretation is not a straightforward process. In first place, *denoising* algorithms (Frangakis and Förster, 2004) are sometimes useful to identify the features of interest more clearly. These algorithms subtract the noise but also a part of the signal, and consequently they should be employed carefully. In this work, tomograms have been denoised using *non-linear anisotropic diffusion* (NAD, Fernandez and Li, 2003; Frangakis and Hegerl, 2001), which enhances features such as membranes with minimal loss of detail. After denoising, segmentation procedures⁹ can be applied to the tomogram to highlight the regions of interest. For this study, a special segmentation algorithm has been developed in order to study the presynaptic cytomatrix (see 5.3).

⁹ *Segmentation* can be defined as the partition of the data into different regions, each with different properties. For example, in cellular tomograms the plasma membrane, the organelles and the protein complexes can be extracted as separate components. Image segmentation is, in general, a key step towards the quantitative interpretation of image data (Soille, 2003).

3 Aims of This Study

3. Aims of This Study

The primary goal of this work was to investigate the native 3D structure of the mammalian presynaptic cytomatrix by cryo-electron tomography (cryo-ET), in order to gain insights into its organization and possible roles in the synaptic vesicle cycle. This constituted a significant challenge, as presynaptic terminals have hitherto never been analyzed by means of cryo-ET. In particular, the following issues needed to be addressed:

1. **Establishment of an optimal experimental system.** The aim was to find a biological model that would (i) be technically suitable for cryo-ET, (ii) faithfully reproduce the native structure of the presynaptic cytomatrix and (iii) be amenable to pharmacological manipulations. This involved the investigation of various synaptic preparations, namely cortical synaptosomes, primary neuronal cultures and cryosections from organotypic slices (all obtained from rat).
2. **Development of computational methods for the quantitative analysis of presynaptic architecture.** Cryo-ET offers a high resolution view into native cellular structures, which are often described in a qualitative manner. However, objective and quantitative analysis methods are necessary to provide deeper understanding of the biological processes. In particular, such methods are essential for the detection and study of the hundreds of small filaments forming the presynaptic cytomatrix in each terminal.
3. **Recording of tomographic datasets of synapses in different functional states and analysis of the alterations of the presynaptic cytomatrix.** Once the experimental model and the analysis method were established, the presynaptic cytomatrix was studied both in resting synapses and in synapses under different pharmacological treatments that modified their functional state. The comparison of both conditions provided insights into the role of the presynaptic cytomatrix in synaptic communication.

4 Materials and Methods

4. Materials and Methods

4.1 Sample preparation

4.1.1 Synaptosomal extraction

Cerebro-cortical synaptosomes were extracted from 6-8-weeks-old male Wistar rats as described in (Dunkley et al., 1988; Godino et al., 2007) in accordance with the procedures accepted by the Max-Planck-Institute for Biochemistry. In brief, anesthetized animals were decapitated and the cortex was extracted and homogenized with up to seven strokes at 700 rpm in a Teflon-glass homogenizer in homogenization buffer (HB: 0.32 M sucrose, 50 mM EDTA, 20 mM DTT, 1 tablet of Complete mini EDTA-free protease inhibitor cocktail (Roche) per 10 ml [pH 7.4]). The homogenate was centrifuged for 2 min at $2,000 \times g$ and the pellet was resuspended in HB and centrifuged for another 2 min at $2,000 \times g$. Supernatants from both centrifugations were combined and centrifuged for 12 min at $9,500 \times g$. The pellet was resuspended in HB and loaded onto a three-step (3%, 10%, 23%) Percoll (Sigma) gradient in HB without protease inhibitor cocktail. The gradients were spun for 6 min at $25,000 \times g$ and the material accumulated at the 10/23% interface was recovered and diluted to a final volume of 100 ml in Hepes-buffered medium (HBM: 140mM NaCl, 5 mM KCl, 5 mM NaHCO₃, 1.2 mM Na₂HPO₄, 1 mM MgCl₂, 10 mM glucose, 10 mM Hepes [pH 7.4]). Percoll was removed by an additional washing step with HBM by centrifugation for 10 min at $22,000 \times g$, the pellet was resuspended in HBM and immediately used in the experiments. All steps were carried out at 4°C (Figure 10).

4.1.2 Glutamate release assay

The viability of synaptosomes was confirmed by glutamate release assay (Godino et al., 2007; Nicholls and Sihra, 1986). A synaptosomal solution of 1 mg/ml in HBM was supplemented with 1 mg/ml BSA and incubated 1 h at 37°C. 1.33 mM CaCl₂, 1 mM NADP⁺ and 50 U/mL of glutamate dehydrogenase were added and the increase in fluorescence due to the reduction of NADP⁺ upon addition of 30 mM KCl was measured, at excitation and emission wavelengths of 340 nm and 460 nm respectively (LS50 spectrometer, Perkin-Elmer). The curves were calibrated by the addition of 4 μM glutamate. Control experiments to determine the non-exocytic component of glutamate release were performed in the absence of Ca²⁺.

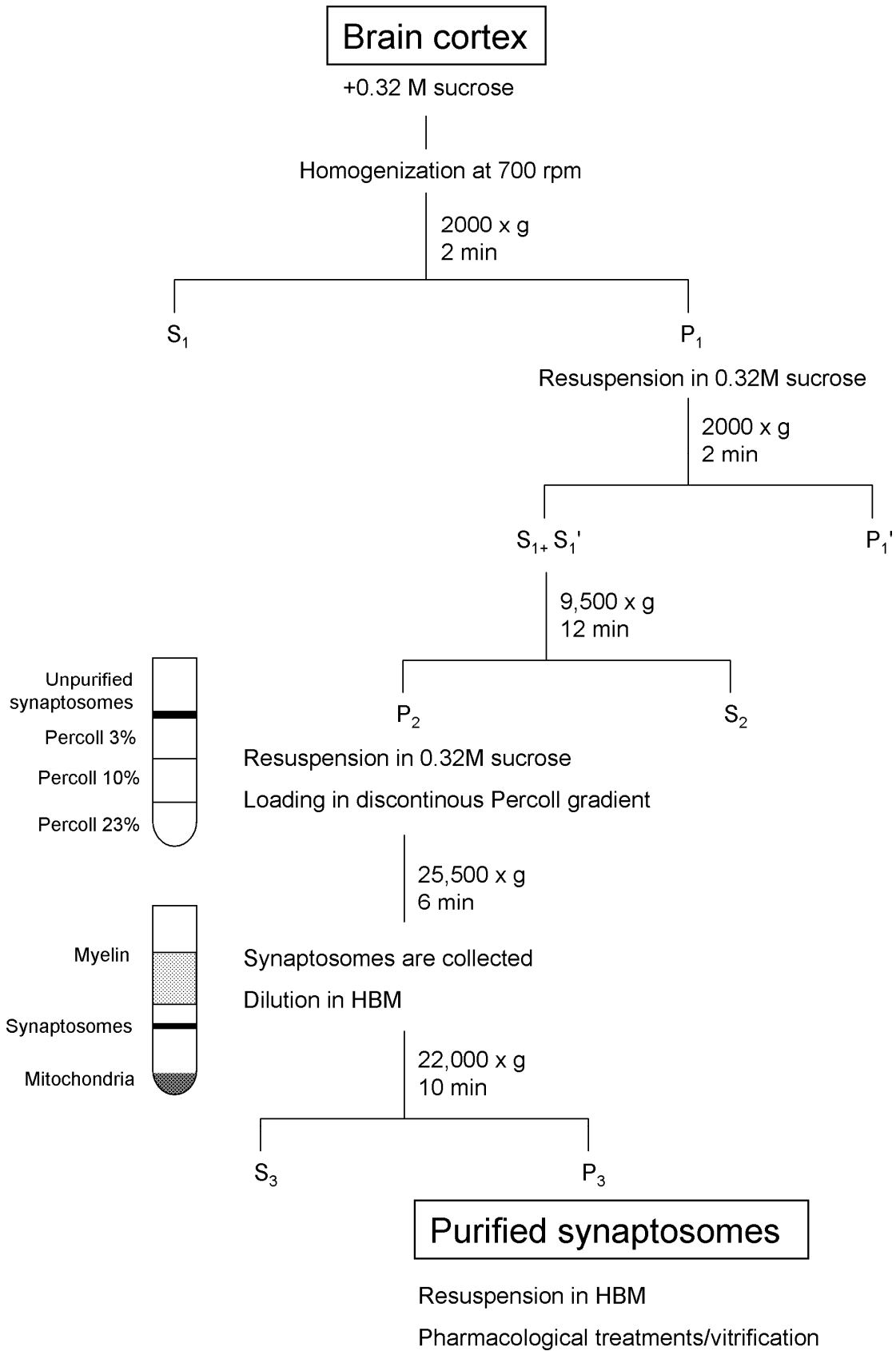


Figure 10 Summary of the synaptosome extraction procedure (adapted from Godino, 2006).

4.1.3 Pharmacological treatments and vitrification of synaptosomes

Synaptosomes were diluted to ~ 1 mg/ml protein concentration determined by Bradford assay (BioRad), incubated for 1 h at 37°C and vitrified. Pharmacological treatments were applied before vitrification by incubating synaptosomes (i) 1 min with 30 mM KCl; (ii) 1 min with 100 or 300 mM hypertonic sucrose. Synaptosomes in 300 mM HTS were not analyzed; (iii) 2 h with 200 nM TeTx (Merck), omitting the 1 h pre-incubation; (iv) 15 min with 1 μ M okadaic acid (OA, Merck); (v) 90 min with 10 μ M jasplakinolide (Merck). In the case of synaptosomes treated with phalloidin (Merck), the drug (100 μ M) was added to the homogenization buffer as it is membrane impermeable. Synaptosome extraction and vitrification was carried on normally from there on.

Additionally, synaptosomes inoculated with herpes simplex virus 1 strain wildtype 17 (Maurer et al., 2008) for 60 minutes on ice and 2, 30 or 60 min at room temperature were included in the study of synaptic vesicle fusion. In this case, sample preparation and data acquisition were performed by Ulrike Maurer (Department of Molecular Structural Biology, Max Planck Institute of Biochemistry, Martinsried, Germany).

For vitrification, a 3 μ l drop of 10 nm colloidal gold (Sigma) was deposited on plasma-cleaned, holey carbon copper electron microscopy grids (Quantifoil) and allowed to dry. A 3 μ l drop of synaptosomal suspension was placed onto the grid, blotted with filter paper (Whatman #4) and plunged into liquid ethane. Vitrified grids were either transferred directly to the microscope cryo-holder or stored in liquid-N.

4.1.4 Hippocampal slice cultures, high pressure freezing and cryosectioning

Transverse hippocampal slices (400 μ m thick) were prepared from 6–7-day-old Wistar rats and maintained for 10–15 days in culture as described previously (Stoppini et al., 1991). They were high-pressure frozen after a 5 min immersion in medium supplemented with 20% dextran (40 kDa) and 5% sucrose according to (Zuber et al., 2005).

Thin sections (50–80 nm feed) were obtained as described previously (Zuber et al., 2005) with a Leica UC6/FC6 cryo-ultramicrotome and a 35° cryo-immuno diamond knife (Diatome). Sections were transferred onto 400 \times 100 Mesh grids (Agar Scientific), coated with a thin layer of carbon. Subsequently, PbSe Core EviDots (Evident technologies) fiducial markers were applied on the sections according to (Masich et al., 2006). Slice culture, high-pressure freezing and cryosectioning were performed by Benoît Zuber (MRC Laboratory of Molecular Biology, Cambridge, UK).

4.1.5 Hippocampal neurons in culture

Gold finder EM-grids (type NH2A by Plano, Wetzlar, Germany) coated with Quantifoil (TM) R2/2 were sterilized in ethanol for 10 min, then washed in H₂O, and transferred to culture dishes. Both grids and dishes were coated with 1 mg/ml poly-l-lysine (in water) for 1 day, washed in D-MEM medium (Gibco 61965), and placed in D-MEM with B27 supplement prior to plating. Whenever a liquid had to be removed completely from a dish during washing and medium exchange steps, grids were transferred into another dish containing the appropriate liquid in order to prevent grids from drying. Sideways submersion of grids into the media greatly reduced the risk of ablation of the sensitive grid coating.

Primary hippocampal neuronal cultures were dissected from E18 Sprague–Dawley rats in accordance with the procedures accepted by Max-Planck Institute for Neurobiology, and dissociated as described previously (Goslin and Banker, 1991). Briefly, hippocampal neurons were dissected from embryos and were dissociated after incubation for 30 min in an EDTA/trypsin solution (0.25% trypsin, 1 mM EDTA). After washing with D-MEM and 10% FBS, neurons were plated on the poly-l-lysine coated dishes and EM grids (kept in the dishes). Cultures were kept at 37 °C in 5% CO₂ and investigated at 6-7 days in vitro (DIV). Neuronal cultures were carried on by Frank Voss (Max-Planck-Institute for Neurobiology, Martinsried, Germany).

The grids were imaged in HBSS in glass-bottom culture dishes (MatTek P35G-1.5-7-c-grid) mounted in a chamber at 35 °C with a Zeiss Axiovert 200M inverted light microscope equipped with motorized stage and using a Zeiss air 10× Plan-Neofluar Ph1 objective with 0.3 N.A., a Zeiss air 20× Achroplan Ph2 objective with 0.4 N.A. Images covering a whole grid were recorded using Mosaix and z-stack modules of Zeiss Axio Vision 4.1 software.

4.2 Cryo-Electron Tomography

Tilt series were collected under a low-dose acquisition scheme (Koster et al., 1997) using Phillips CM300 and FEI T30 Polara microscopes operated at 300 kV. Both microscopes were equipped with a field emission gun, a 2k×2k Gatan CCD camera, a Gatan post-GIF energy filter operated in the zero-loss mode and a computerized cryo-stage designed to maintain the specimen temperature below -150°C. Tilt series were recorded typically from -60° to 60° with 2° angular increment. Pixel sizes were 0.68 (CM300) and 0.66 nm (Polara) at the specimen level and the defocus was set to -9 μm. The total dose was kept below 80 e⁻/Å².

Tilt series were aligned using gold beads as fiducial markers and three-dimensional reconstructions were obtained by weighted back-projection using the TOM toolbox (Nickell et al., 2005). During reconstruction the projections were binned twice (final pixel size 2.64 and 2.72 nm) and low-pass filtered at the post-binning Nyquist frequency. Voxel intensities were normalized between -1 (black) and +1 (white). The tomograms were subsequently denoised by anisotropic non-linear diffusion

(Fernandez and Li, 2003). Simultaneous iterative reconstruction technique (SIRT) was used in some cases (see 5.2.6).

4.3 Data analysis

The morphological properties, location parameters and gray-scale values were determined for all synaptic vesicles, tethers and connectors of each synapse separately. For the analysis of vesicle distribution (5.2.2), the part of the interior of the presynaptic terminal occupied by synaptic vesicles was divided into 1 pixel-thick layers according to the distance to the AZ, and the fraction of layer volume occupied by vesicles was measured. Possible bias due to differences in size among individual synapses was thereby avoided. In all other cases involving vesicle distance to the AZ (Figure 20, Figure 22, Figure 25, Figure 27), the distance of the vesicle center to the AZ was used. All parameters, except those related to vesicle clusters were analyzed only in the first 250 nm from the AZ, as vesicles in this region are the main candidates to participate in exocytosis during relatively short stimulations. For cluster analysis the whole presynaptic terminals were considered. The outer membrane diameter of vesicles was measured, and only those with diameter of 20-60 nm were considered as synaptic vesicles and included in the analysis. The numbers of analyzed tomograms, synaptic vesicles, connectors and tethers are summarized in Table 1.

Sample	Number of experiments	Number of tomograms	Total number of vesicles	Total number of connectors	Total number of tethers
Untreated synaptosomes	3	7	841	2721	166
100 mM HTS	1	4	518	1935	45
300 mM HTS	1	3	-	-	-
30 mM KCl	3	6	333	389	4
1 μ M OA	2	6	550	1353	12
200 nM TeTx	1	4	542	1110	42
Organotypic slices	2	3	198	306	14
Total		33	2982	7814	283

Table 1 Number of experiments, tomograms, synaptic vesicles, connectors and tethers analyzed for each group of samples. Synaptosomes treated with 300 mM HTS presented a highly perturbed morphology and were thus not analyzed.

The length of connectors and tethers was estimated based on the positions of contact voxels, where the contact voxels of a connector are those that contact the vesicle membranes (those that contact the vesicle membrane and the AZ in the case of tethers, Figure 11AI). In order to take curvature into account, the length was calculated as the sum of straight-line distances between (centers of) contact voxels and a middle voxel (a voxel belonging to the connector/tether that is equidistant from the two membranes, Figure 11AII). A more intuitive estimate of connector/tether lengths would be to measure the lengths from edge to edge (Figure 11AIII). However this is well defined

only for straight connectors/tethers, in which case edge-to-edge lengths are one voxel size (~2.7 nm) longer than estimates presented here. For example, a straight linear connector reported here to have length of 5.4 nm is composed of three voxels (since distance between centers of the first and the third voxel is two voxel sizes) and would have edge-to-edge length of 8.1 nm.

The redundancy of connectivity clusters formed by vesicles interlinked by connectors, i.e. the fraction of connectors that can be removed without separating the cluster into disconnected parts, was calculated from the Euler characteristics. *Hierarchical clusters* based on the Euclidean distance between vesicles were compared with connectivity clusters. Two standard hierarchical clustering methods were used: average and single linkage. For single linkage, the distance between two clusters is defined as the distance between the two closest vesicles belonging to the two clusters (this linkage is specially suited to describe elongated or chain-like clusters). For average linkage the distance between two clusters is calculated as the average distance between all pairs of objects in both clusters (this method is more appropriate to describe globular clusters). The inter-cluster distance parameter was chosen so that the number of hierarchical and connectivity clusters would be the same. A similarity coefficient of hierarchical and connectivity clusters was calculated using the variation of information approach (Meila, 2007). This method was shown not to depend on the number of elements that are clustered and to distinguish similar clusters adequately. The ratio between similarity coefficients of single- and average-linkage clusters (< 1 for more globular clusters and > 1 for more elongated clusters) was used as a measurement of similarity to connectivity clusters. Figure 11B shows different cluster types according to their shape and connector redundancy.

For the analysis of connectivity, clustering, tethering and vesicle size and distribution, values calculated for each treatment were combined and statistically analyzed to generate the results shown in Figure 19, Figure 20, Figure 21, Figure 22, Figure 25, Figure 27. Averages were calculated over all measurements of a specific property. For example, the fraction of volume occupied by vesicles was averaged over synapses and connector length over connectors. Student's t-test was used for statistical analysis of values that appeared to be normally distributed (e.g. vesicle radius) and Kruskal-Wallis test (non-parametric) for values deviating from the normal distribution (e.g. number of tethers/connectors per vesicle). When values fell into discrete bins (e.g. fraction of connected and non-connected vesicles) the Chi-square test was used. In all cases, confidence levels were calculated using two-tailed tests. The confidence values were indicated in the graphs by * for $p < 0.05$, ** for $p < 0.01$ and *** for $p < 0.001$.

Electron density of vesicle lumen was calculated in tomograms reconstructed by WBP as well as by SIRT. In both cases the luminal density was normalized in respect to the vesicle membrane density. The colocalization of proximal synaptic vesicles and structures protruding from the AZ was assessed by the correlation between vesicle locations and electron density of the cytoplasm in the first 8 nm from the AZ.

The segmentation and analysis software was written in Python programming language using the numerical and scientific packages NumPy and SciPy (www.scipy.org). It was executed under Linux on Opteron-based architecture, with a typical single processor run-time for one synapse of several hours.

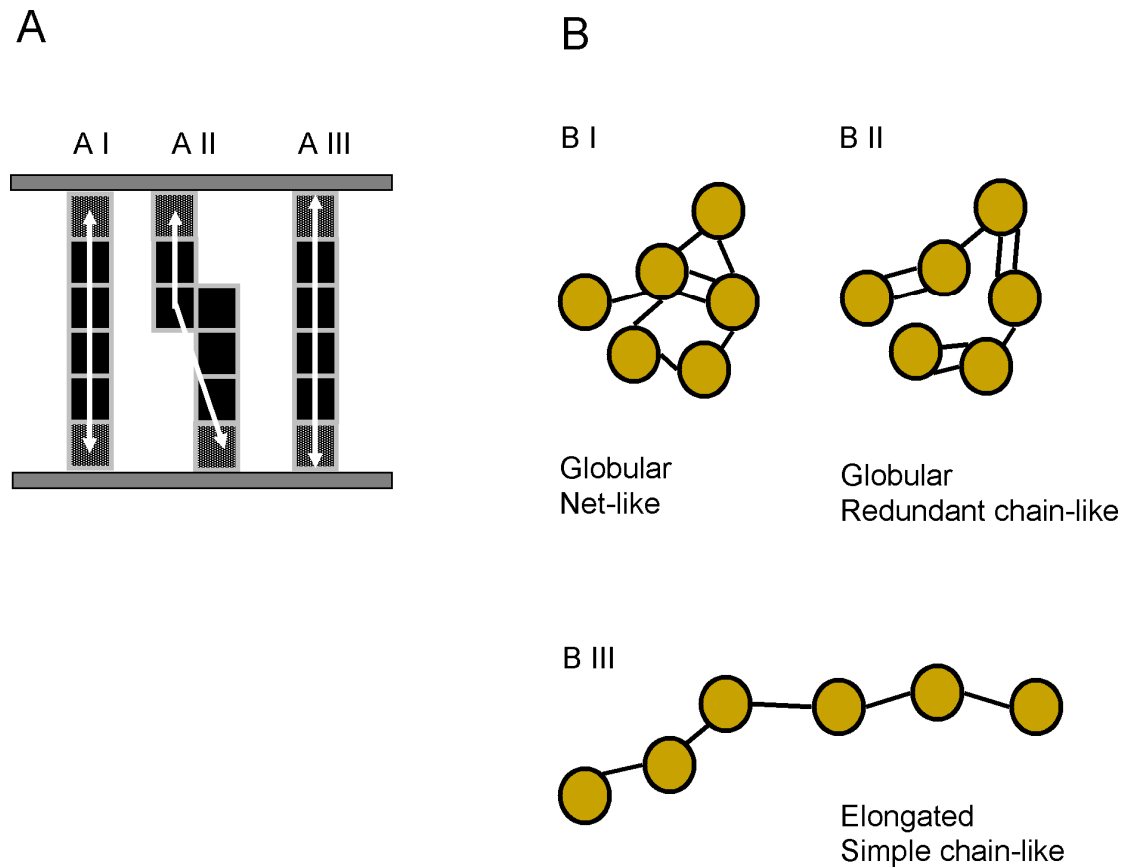


Figure 11 Morphological analysis. (A) Segment length can be estimated from the center (A I, straight segments; A II curved segments) or edge (A III) of contact voxels (black boxes with white pattern). Voxels belonging to the segment (black boxes), SV or AZ membrane (grey straight lines), distance calculated (double white arrows). (B) Different cluster types according to shape and connector (link) redundancy. Synaptic vesicles (yellow circles), connectors (black bars). 3 out of 8 (2 out of 7), 3 out of 8 (none) and none (none) connectors (links) are redundant for B I, B II and B III clusters respectively.

5 Results

5. Results

5.1 Establishment of the experimental system

In current neurobiological research, three preparations are preferred for the study of synaptic transmission in central mammalian synapses *in vitro*: synaptosomes, brain slices and primary neuronal cultures. These preparations are all amenable for cryo-ET and were consequently examined.

Synaptosomes are a cell fraction of purified synapses, consisting of resealed presynaptic terminals often attached to a portion of the postsynaptic cell (Whittaker, 1993). These structures perform metabolic activity, maintain a normal resting membrane potential and, under stimulation, carry out synaptic vesicle exo- and endocytosis in a physiological manner for extended periods of time. As they can easily be subjected to pharmacological manipulations, synaptosomes are widely used as a model for neurotransmitter release (Harrison et al., 1988; Nicholls and Sihra, 1986). Furthermore, synaptosomes are ideal candidates for cryo-ET examination as their thickness is normally below 0.5 μm . For this study, rat cortical synaptosomes were used.

The synaptosomal fraction was traditionally isolated using a continuous sucrose gradient (Whittaker, 1993), which subjected synaptosomes to very high osmolarity conditions. In contrast, the method introduced by (Dunkley et al., 1986; Nagy and Delgado-Escueta, 1984) is based on a Percoll gradient and maintains isoosmolarity at all times. Percoll is washed in the last step and the samples can be incubated and vitrified in physiological saline buffer (see 4.1.1). Also, this extraction procedure takes less time, reducing the possibility of sample deterioration.

The Percoll gradient method was modified according to (Godino et al., 2007) for optimized synaptosome preservation. In particular, resuspension steps were done very carefully as they are likely to damage the cell membrane. Not only all steps were carried at 4°C, but all tubes and tools were cooled and soaked in buffer before being used. Finally, synaptosomes were incubated for ~1 h at 37°C before being vitrified in order to recover their physiological function. Synaptosomes should always be vitrified shortly following their extraction, as they retain their functionality only for a few hours. It was found that a synaptosome concentration of ~ 1mg/ml of protein was optimal for plunge freezing.

Synaptosome integrity and functionality was monitored by their ability to release neurotransmitter by Ca^{2+} -dependent exocytic mechanisms. In agreement with previous studies (Godino et al., 2007; Nicholls and Sihra, 1986), glutamate release was typically of 1 nmol/mg min (Figure 12).

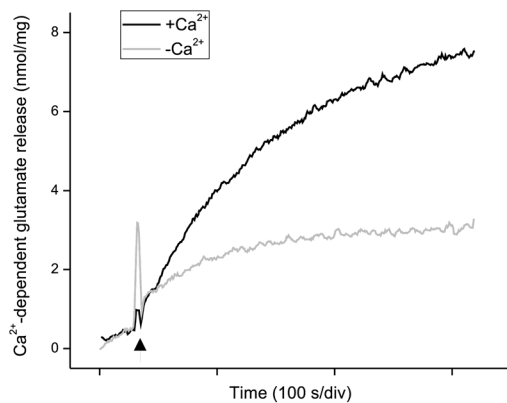


Figure 12 Glutamate release assay. Representative traces show the response of synaptosomes upon injection of 30 mM KCl (arrow), in the presence (black) or absence (grey) of 1.33 mM CaCl_2 . The peak observed upon KCl injection is a common artifact due to the introduction of air bubbles that does not affect the measurement.

Vitrified synaptosomes usually formed large aggregates on the EM grid. These aggregates were in general too thick for cryo-ET, but their periphery was accessible¹⁰ (Figure 13). Synaptosomes were also found in isolation or forming part of smaller groups. The majority of structures observed were presynaptic terminals that did not have a postsynaptic partner, as described by (Dunkley et al., 1988). Isolated synaptic vesicles, mitochondria and other membrane-bound structures were also found. Synapses were visually identified by the presence of a presynaptic terminal containing synaptic vesicles separated from the postsynaptic side by a very regular spacing of ~ 25 nm between pre- and postsynaptic terminals (the synaptic cleft).

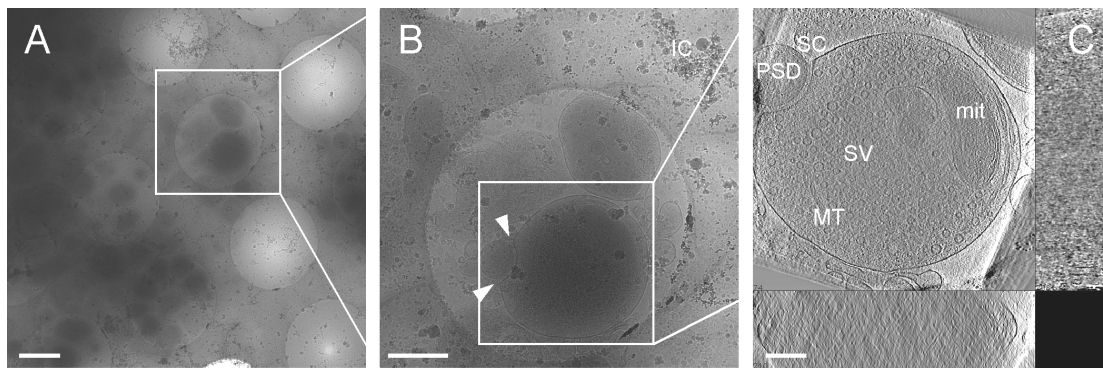


Figure 13 Images of synaptosomes at different magnifications. (A) Overview of synaptosomes on an EM grid. (B) Synaptosome in a hole of the Quantifoil carbon film. The synaptic cleft is marked by two white arrowheads. Ice crystals (IC). (C) 2.7 nm-thick tomographic slices in xy, xz and yz. Synaptic vesicles (SV), postsynaptic density (PSD), synaptic cleft (SC), mitochondrion (mit), microtubule (MT). Scale bars: (A) 1000 nm, (B) 500 nm, (C) 200 nm.

Choosing adequate candidates for tomography was usually a time consuming process. Together with the relative low occurrence of synapses, good eye sight was required to

¹⁰ Sample thickness (t) can be estimated by $t/\Lambda = \ln(I_{unf}/I_{flt})$, where Λ is the mean free path of elastically scattered electrons (see 2.1.2) and I_{flt} and I_{unf} are the respective filtered and unfiltered average intensities of the image (Egerton and Leapman, 1995).

spot suitable candidates using a minimal electron dose. For successful tomography and optimal SNR, synapses had to be located on the holes of the Quantifoil carbon film, in areas of sufficiently thin ice and that could be tilted ideally to $\pm 70^\circ$. Often, neighboring biological structures, ice crystal contamination or the grid bars themselves limited the tilt range. Also, in order to allow fiducial marker alignment, a sufficient number of gold particles had to surround the sample. Considering an average tilt series recording time of ~ 70 min, it was hardly possible to obtain more than 5 series per microscopy session, with at least half of the time consumed in searching.

Synaptosomes also present limitations, as they have been severed from the cell body and subjected to potentially damaging centrifugation steps. Organotypic slices, sections of brain tissue kept in culture, provide a good alternative. In these cultures cells continue to differentiate and develop a tissue structure that closely resembles that observed *in vivo*. In fact, organotypic slices are often the system of choice for electrophysiological studies (Gähwiler et al., 1997).

The vitrification of organotypic slices, typically several microns thick, required high-pressure freezing. Furthermore, due to their high water content, cryoprotective agents such as sucrose and dextrane became necessary, resulting in increased osmolarity (additional ~ 300 mOsm) and reversible effects on the physiological properties of the slice (Zuber et al., 2005). The vitrified tissue was cryosectioned (cut at liquid-N temperature) yielding cryosections 50-80 nm thick. These sections suffered from cracks and cryosectioning-induced compression, and their thickness limited the volume that could be studied. Surface artifacts, such as crevasses and knife marks (Han et al., 2008), were also present but did not substantially affect tomographic studies.

Performing electron tomography on cryosections adds yet another level of difficulty in comparison with plunge frozen samples, due to their poor adhesion to the EM grid and instability under the electron beam. It was often the case that whole ribbons would jump out of the supporting grid after being exposed to doses $< 1e^-/\text{\AA}^2$. Also, small cracks in the section would develop into large holes under a moderate electron dose. Consequently, the electron dose had to be reduced for the recording of tilt series of cryosections, typically to values of $\sim 40e^-/\text{\AA}^2$. Due to the very limited thickness of the sections, the SNR of the tomograms was comparable, and often superior, to that of synaptosomal tomograms.

The location of synapses within the cryosections was also a difficult task due to their very low contrast, but it could be guided by the cellular architecture of nervous tissue (Figure 14, Figure 15). Regions of the tissue with higher abundance of synapses were characterized by the presence of multiple thin (< 500 nm wide) neuronal processes, often containing synaptic vesicles (Figure 14A). These likely corresponded to areas of contact between dendritic and axonal trees of electrically connected neurons. On the contrary, synapses were rarely found in the vicinity of the cell body or in regions with numerous myelinated axons (Figure 15C). The structure of the myelin layers could be distinguished much more clearly than in conventionally prepared samples (Figure 15D) (Zhang et al., 2005).

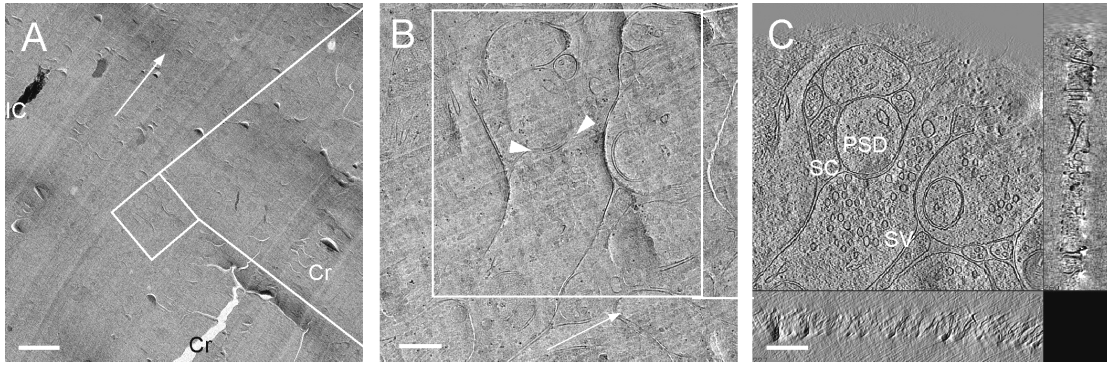


Figure 14 Images of a synapse in a hippocampal cryosection at different magnifications. (A) Overview of a cryosection. Ice crystals (IC), cracks (Cr), cutting direction and knife marks (long thin white arrows). (B) Close-up to a synaptic contact. The synaptic cleft is marked by two white arrowheads. (C) 2.7 nm-thick tomographic slices in xy, xz and yz. Synaptic vesicle (SV), postsynaptic density (PSD), synaptic cleft (SC). Scale bars: (A) 1000 nm, (B, C) 200 nm.

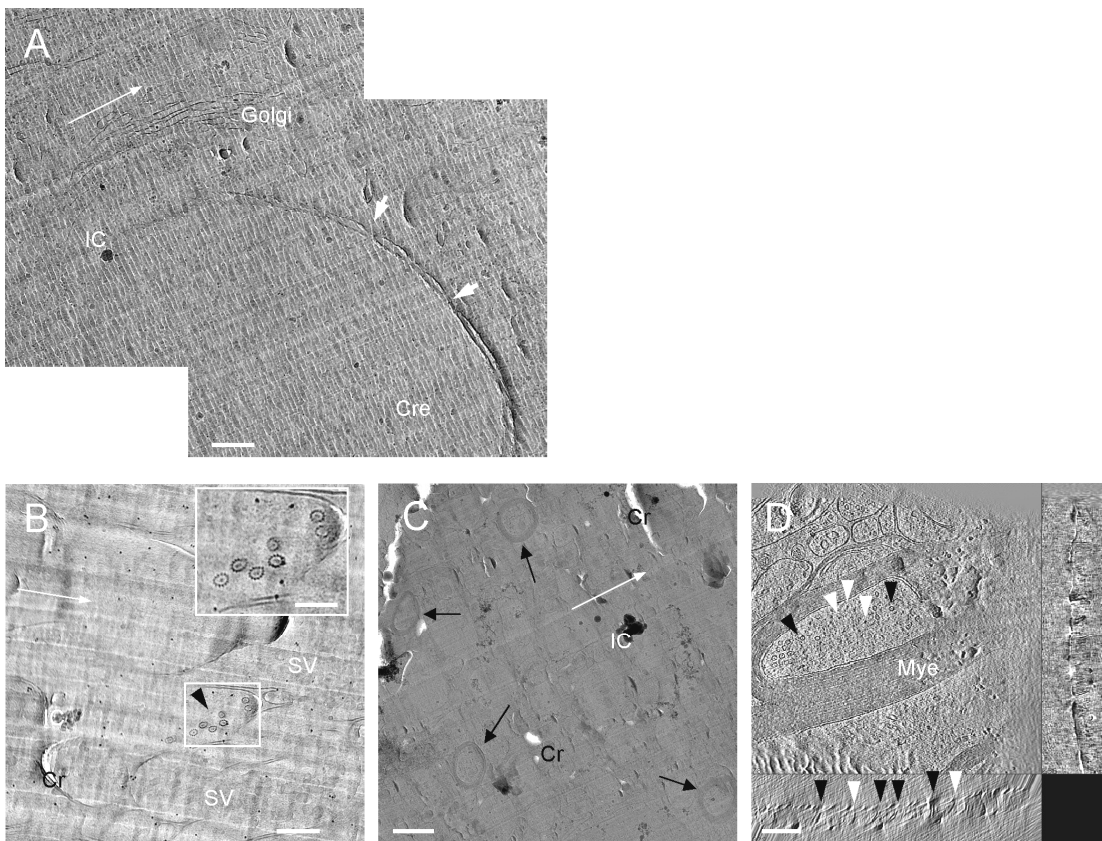


Figure 15 Images of non-synaptic structures in hippocampal cryosections. Ice crystals (IC), cracks (Cr), cutting direction and knife marks (long thin white arrows), crevasses (Cre), cutting direction and knife marks (long thin white arrows). (A). Cell nucleus, Golgi apparatus, nuclear pore complexes (short thick white arrows). (B) Axonal cross section. Synaptic vesicles (SV), microtubules (black arrowheads). Individual microtubule protofilaments are visible (inset). (C) Overview of an area with multiple myelinated axons (black arrows). (D) 3.3 nm-thick tomographic slices in xy, xz and yz of a myelinated (Mye) axonal process containing microtubules (black arrowheads) and intermediate filaments (white arrowheads). Scale bars: (A, B, D) 200 nm (B inset: 100 nm), (C) 1000 nm.

Lastly, primary cultures of dissociated rat hippocampal neurons (Meberg and Miller, 2003) were also studied. These cultures are suitable for cryo-ET investigation, as the cells can grow directly on EM grids (Figure 16A) and present thin processes amenable for direct imaging (Figure 16B-D) (Lučić et al., 2007). In this system, synaptogenesis is initiated after 3 DIV (Fletcher et al., 1994), but still after 7 DIV immature synapses greatly outnumber mature ones (Ahmari and Smith, 2002). After 10-15 DIV there is already a considerable number of mature synapses (Ziv and Garner, 2004), but neuronal processes grow in thickness and number preventing direct access to synapses by EM. Thus, cultures are usually sectioned after fixation and plastic embedment for conventional EM (Bartlett and Banker, 1984; Schikorski and Stevens, 2001).

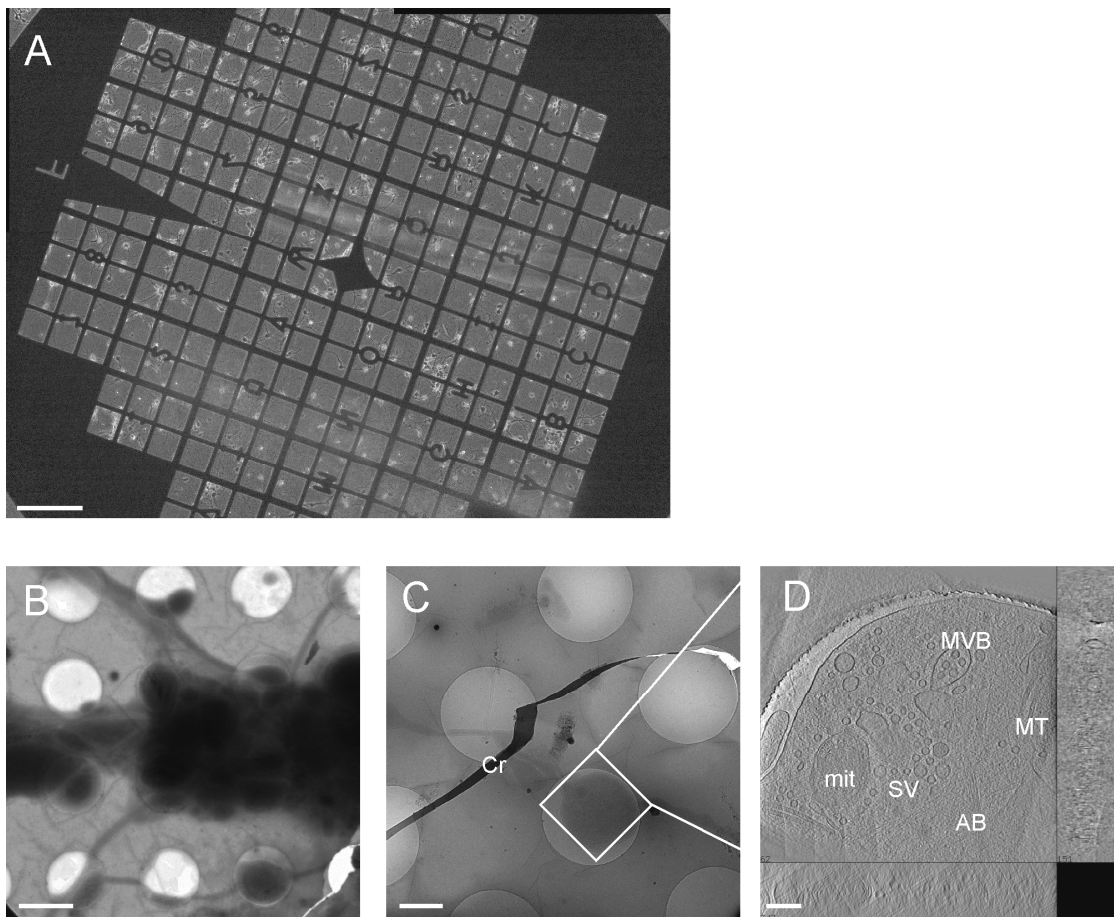


Figure 16 Images of 6DIV neuronal cultures. (A) Light microscopy, phase contrast image of neurons cultured on an EM grid. (B) Overview of vitrified neuronal cultures in EM. The darkest areas are too thick for tomography. (C) Overview of a thin axon amenable for tomography. Crack in the Quantifoil carbon film (Cr). (D) 3.3 nm-thick tomographic slices in xy , xz and yz . Synaptic vesicles (SV), mitochondrion (mit), microtubule (MT), actin bundle (AB), multivesicular body (MVB). Scale bars: (A) 200 μm , (B) 2 μm , (C) 1 μm , (D) 200 nm.

Interesting morphological features could be observed in neuronal cultures (5.4.2), but synapses were generally not accessible. Consequently, the analysis of the presynaptic ultrastructure reported in this work focused in synaptosomes and organotypic slices, where synapses could be more easily located.

5.2 The presynaptic cytomatrix in cortical synaptosomes and hippocampal organotypic slices

In total, thirty-three tomograms of cryo-preserved presynaptic terminals from untreated rat cerebro-cortical synaptosomes, synaptosomes subjected to different pharmacological treatments and rat hippocampal organotypic slices (Table 1) were analyzed by the automatic procedure described below (5.3). Observations from other tomograms that were not quantitatively analyzed have also been included in this section.

Synaptosomes were subjected to pharmacological treatments aimed at either causing synaptic vesicle release or modulating it. Exocytosis was induced by (i) the application of hypertonic sucrose (HTS) leading to the release of the RRP (Rosenmund and Stevens, 1996), and (ii) high concentrations of KCl, mobilizing both the RRP and the reserve pool (Ashton and Ushkaryov, 2005; Rizzoli and Betz, 2005). Neurotransmitter release was modulated by (i) incubation with tetanus toxin (TeTx), a clostridial neurotoxin that prevents SNARE complex formation and synaptic vesicle fusion by cleaving the vesicular SNARE protein synaptobrevin/VAMP (Schiavo et al., 2000), and (ii) the phosphatase inhibitor okadaic acid (OA), which alters the phosphorylation state of synapsin (Jovanovic et al., 2001) and increases vesicle mobility (Betz and Henkel, 1994) and neurotransmitter release (Sim et al., 1993). Additionally, synaptosomes were treated with the actin-stabilizing drugs phalloidin (Cooper, 1987) and jasplakinolide (Holzinger, 2009) to investigate possible roles of actin in synaptic vesicle organization. Both drugs prevent monomer dissociation from actin filaments, and can thus have an overall polymerizing effect.

Different methods for 3D tomographic reconstruction were tested in order to optimize the visual detection of the elements of the presynaptic cytomatrix. The results for weighted backprojection (WBP) with analytical weighting were visually superior to those obtained by WBP with exact weighting or by simultaneous iterative reconstruction technique (SIRT). WBP-reconstructed tomograms were subsequently denoised by anisotropic non-linear diffusion (AND), resulting in a significant enhancement of the features of interest.

5.2.1 Morphology of frozen-hydrated presynaptic terminals

As expected for samples preserved in vitreous ice, membranes had smooth and continuous appearance without signs of aggregation and deposition of the cytoplasmic material (Figure 17). Presynaptic terminals had diameters from 0.4 to 1 μm (enclosing volumes from 0.03 to 0.3 μm^3), typically hosting 100-500 synaptic vesicles (Figure

17A, synaptosomes and Figure 17C, organotypic slices). Clathrin-coated vesicles were occasionally observed (Figure 17G). The AZ had a typical length of 200 - 400 nm. The terminals often contained mitochondria, and occasionally cytoskeletal elements such as microtubules or actin, consistent in appearance with those observed in other preparations (Garvalov et al., 2006; Medalia et al., 2007).

Interestingly, OA treatment induced the formation of bundles of long (> 100 nm) actin filaments. The bundles were generally observed further than 300 nm from the AZ and oriented nearly parallel to it (Figure 17B). A substantial amount of long actin filaments could be occasionally observed in synaptosomes extracted in the presence of the actin polymerizing drug phalloidin (100 μ M) (Figure 17E), but treatment with 10 μ M jasplakinolide for 90 min did not have noticeable effects on actin. These results indicate that, even though actin might be abundant in the presynaptic terminal, most of it is in globular, non-polymerized form (G-actin). In contrast, actin filaments were often seen in postsynaptic terminals (Figure 17D).

The use of cryoprotectants was necessary to ensure vitrification of the organotypic slices, resulting in an increase in osmolarity of \sim 300 mOsm (see 5.1). Synaptic morphology in slices was consequently compared with synaptosomes under different hypertonic solutions (100 mM and 300 mM HTS), accounting for the higher resistance of nervous tissue to hypertonicity compared to synaptosomes (Ashton and Ushkaryov, 2005). In agreement with that study, all synaptosomes treated with 300 mM HTS showed major morphological perturbations, with many endosomal or vacuolar compartments, elongated synaptic vesicles and lacking vesicles close to the AZ (Figure 17F). Synaptosomes treated with 100 mM HTS were visually indistinguishable from untreated synaptosomes and organotypic slices (apart from the cryosectioning-induced compression). The preparation procedures for synaptosomes and organotypic slice are entirely different (see 4.1.1 and 4.1.4 for comparison), and therefore it is unlikely that they introduce similar artifacts. Consequently, when compared with 100 mM HTS-treated synaptosomes, slices can serve at least as a partial control for alterations induced by synaptosomal preparation. In addition, the hypertonic treatment used for the subsequent analysis (100 mM HTS for 60 s) was previously shown to cause an exclusive and complete release of the RRP in synaptosomes (Ashton and Ushkaryov, 2005).

None of the treatments resulted in morphological changes indicative of damage, confirming synaptosome integrity. In fact, all these treatments have been extensively characterized in synaptosomes by previous studies. Specifically, the incubation of synaptosomes with 30 mM KCl was shown to induce massive neurotransmitter release over several minutes (Nicholls and Sihra, 1986), while higher KCl concentrations did not cause additional release (Marks and McMahon, 1998). Also, the treatment of synaptosomes with 200 nM TeTx for 2 h is consistent with the conditions shown to induce cleavage of synaptobrevin (Ashton and Dolly, 2000; McMahon et al., 1992). Synaptosomes have been incubated over several minutes with μ M concentrations of OA in order to alter the phosphorylation state of several synaptic proteins in a variety of studies (e.g. Lonart et al., 2003; Sim et al., 1993; Vaughan et al., 1997). At the concentration used here (1 μ M for 15 min), OA completely inhibits the activity of both protein phosphatases 1 and 2A (Cohen et al., 1990).

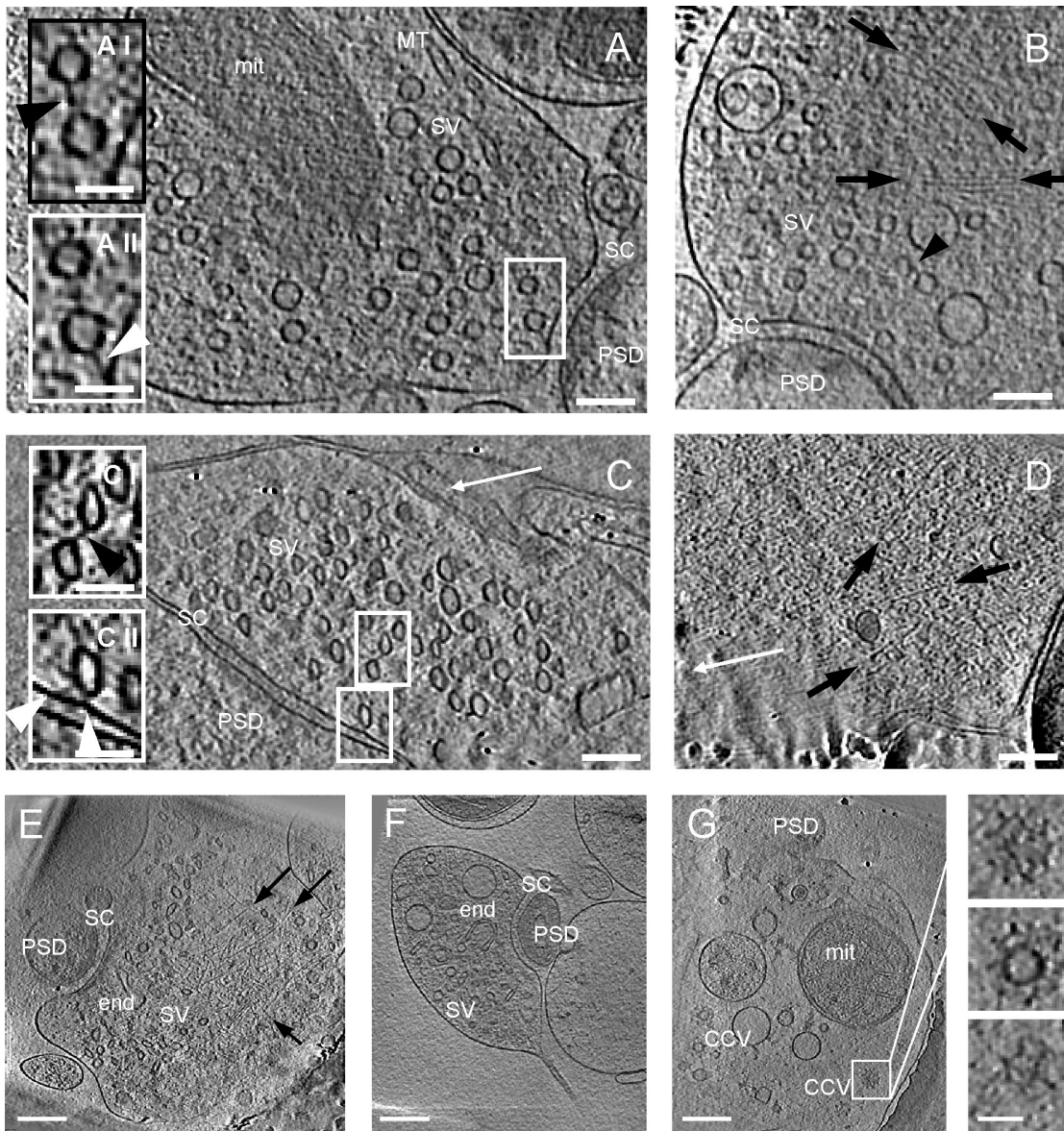


Figure 17 Presynaptic morphology visualized in tomograms of frozen-hydrated synapses. In all panels tomographic slices are 2.7 nm-thick. Synaptic vesicle (SV), mitochondrion (mit), microtubule (MT), synaptic cleft (SC), postsynaptic density (PSD), endosome (end), clathrin-coated vesicles (CCV). (A) Untreated synaptosome. A I: connector linking two vesicles (black arrowhead). A II: tether linking a vesicle to the AZ (white arrowhead; same vesicles as in A I at another z-slice). (B) OA-treated synaptosome showing presynaptic actin bundles (black arrows). (C) Organotypic slice. Synaptic vesicles are compressed along the cutting direction (long thin white arrows in C and D). C I: connector linking two vesicles (black arrowhead). C II: tethers linking a vesicle to the AZ (white arrowheads). (D) Postsynaptic terminal showing actin filaments (black arrows). (E) Synaptosome treated with 100 μ M phalloidin. (F) Synaptosome treated with 300 mM HTS. (G) Clathrin-coated vesicles in a lysed synaptosome. Insets show different tomographic slices of the boxed vesicle. Scale bars: 100 nm in main panels (A-D), 200 nm (E-G), 50 nm in insets.

In both synaptosomes and organotypic slices, numerous filamentous structures were present on the membrane of the synaptic vesicles, in agreement with the reported high density of membrane proteins (Südhof, 2004). Most vesicles were linked to at least one neighbor by short filaments up to 40 nm long (here termed connectors; Figure 17A I and Figure 17C I). Many vesicles were linked to the AZ by short filaments (tethers; Figure 17A II and Figure 17C II). Direct contact between cellular and vesicular membranes was observed only in a few cases (see 5.2.7).

However, the visual analysis of noisy cryoelectron tomograms is subjective and often inconsistent. In particular, the large numbers of connectors and tethers present in presynaptic terminals could not be reliably detected by visual inspection. Thus an algorithm was developed to allow an objective, comprehensive and quantitative analysis of presynaptic structure (see 5.3, Figure 18). For the following sections, connectors and tethers were detected and analyzed by this procedure.

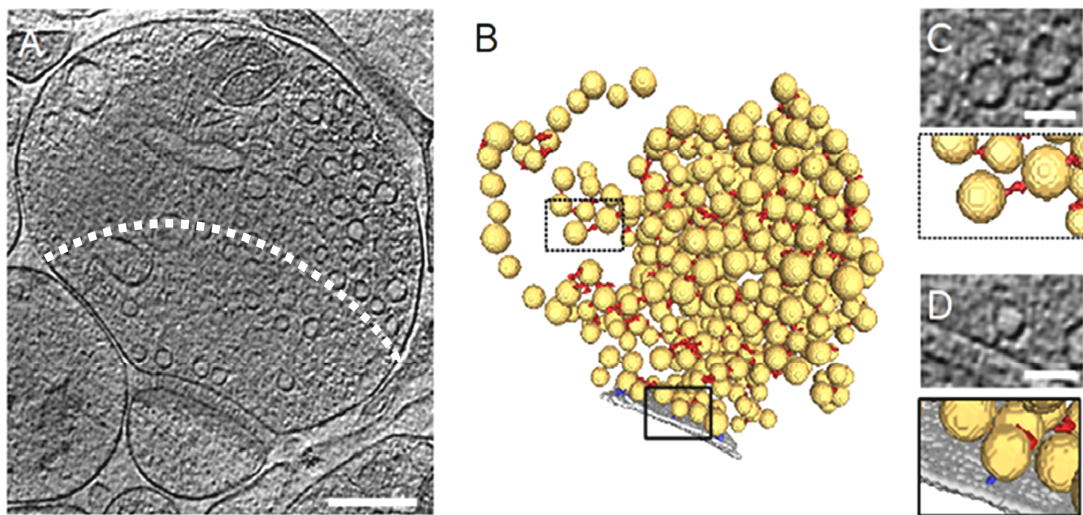


Figure 18 Segmentation procedure. (A) 2.7 nm-thick tomographic slice of a 100 mM HTS-treated synaptosome. The dashed line indicates the analyzed area (first 250 nm from the AZ). (B) 3D segmentation of synaptic vesicles (yellow), AZ (gray), synaptic vesicle connectors (red) and synaptic vesicle tethers (blue). (C) and (D) Tomographic slices showing a synaptic vesicle connector (C) and a tether (D) (upper panels) and their 3D visualization as detected by the automated segmentation procedure (lower panels). Scale bars: 200 nm (A) and 50 nm (C and D).

5.2.2 Inhomogeneity in the spatial distribution of synaptic vesicles

The distribution of vesicles in the presynaptic terminal was assessed by measuring the fraction of cytoplasmic volume occupied by vesicles for the first 250 nm from the AZ (Figure 18A). In every untreated synaptosome, synaptic vesicle concentration had a maximum close to the AZ and a minimum at a distance of 50–70 nm to it (Figure 19A, paired t-test, $p < 0.05$ between minima and maxima). The mean ratio between minima and maxima was 0.38 ± 0.18 . Further away from the AZ, vesicle concentration

increased again. Similar results were obtained for individual synapses in organotypic slices and HTS-treated synaptosomes, whereas vesicle distribution was clearly altered for KCl- and OA-treated synaptosomes. In these cases, vesicle concentration was lowest near the AZ and increased with distance.

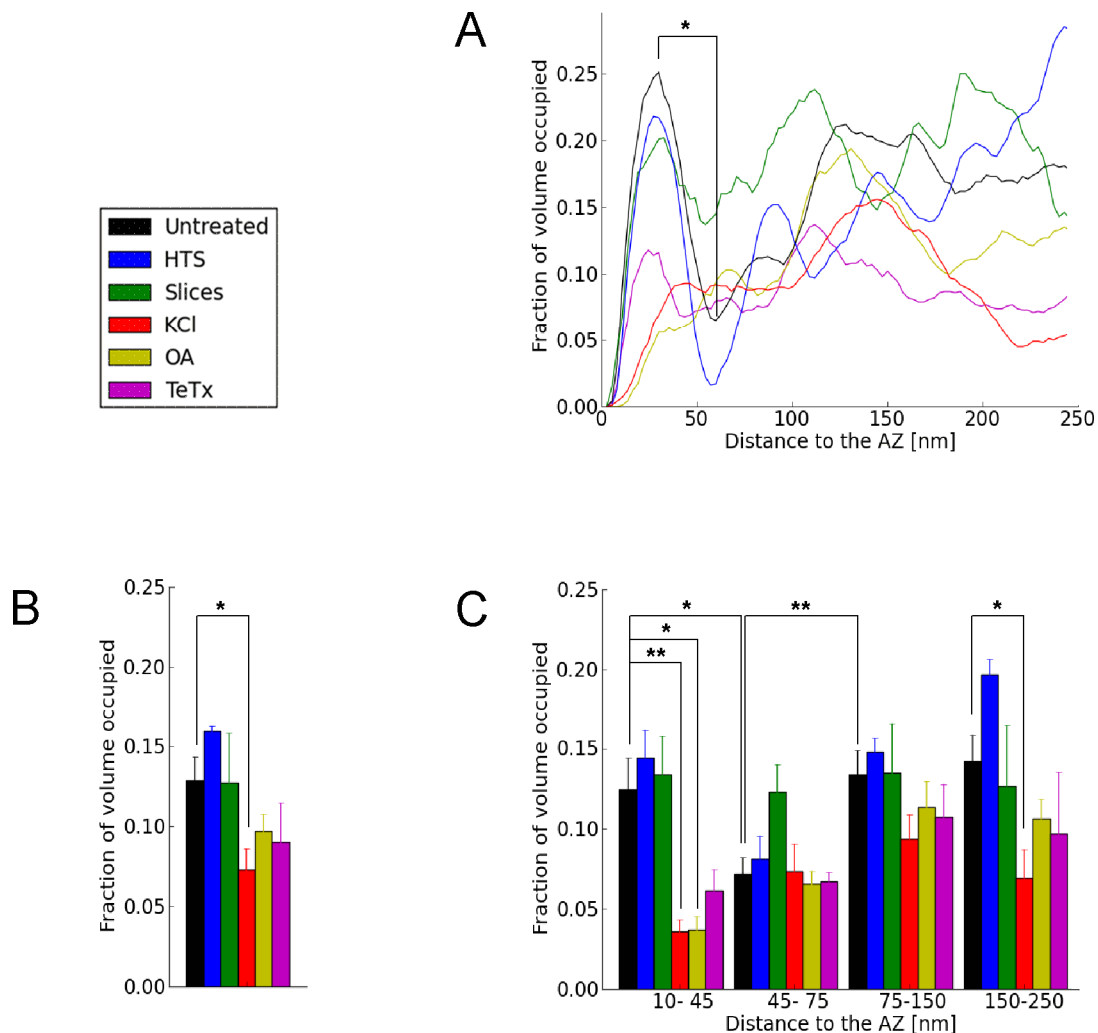


Figure 19 Synaptic vesicle distribution within presynaptic terminals depicted as the fraction of cytoplasmic volume occupied by vesicles. (A) Representative traces of individual synapses. (B) Vesicle concentration for the first 250 nm from the AZ. (C) Vesicle concentration vs. distance to the AZ. Plots show mean values and SEM (error bars). The confidence values are indicated by * for $p < 0.05$ and ** for $p < 0.01$. The number of presynaptic terminals analyzed for each treatment is shown in Table 1.

To facilitate quantitative data analysis, the presynaptic terminal was divided into four zones, according to the distribution of vesicles in untreated synaptosomes: proximal (0-45 nm from the AZ, where the maximum of vesicle density was located), intermediate (45-75 nm, containing the density minimum) and two distal zones of similar thickness further away from the AZ (first: 75-150 nm, and second: 150-250 nm). Taking all untreated synaptosomes together, synaptic vesicle concentration in the intermediate zone was significantly lower than in the proximal and distal zones

(t-test, $p < 0.05$ and $p < 0.01$ respectively, Figure 19C). In organotypic slices, each individual synapse showed an intermediate region of reduced vesicle concentration (Figure 19A). However, the location of this region was different in every synapse because not all sections were perpendicular to the cleft and because of the sectioning-induced compression. Thus, the region of reduced vesicle concentration was not evident upon averaging (Figure 19C).

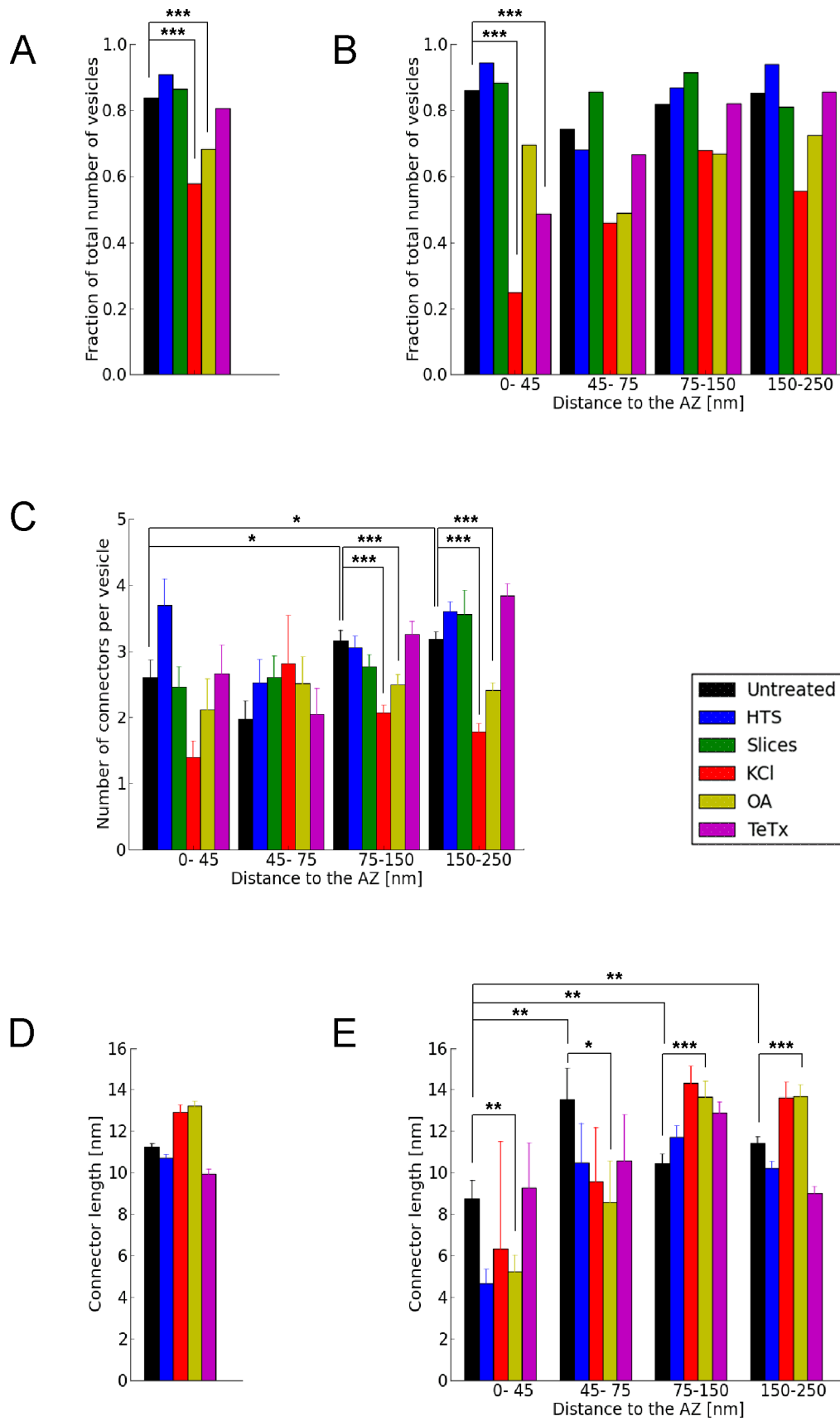
In KCl-treated synaptosomes, the overall vesicle concentration and the concentration in the proximal and second distal zones were significantly reduced compared to untreated synaptosomes (t-test, $p < 0.05$, Figure 19B; $p < 0.01$ and $p < 0.05$, Figure 19C, respectively). The concentration profile of OA-treated synaptosomes (Figure 19) was similar to that of the KCl-stimulated case. Thus, these data provides detailed structural evidence for the stimulating effect of OA, previously detected using biochemical methods (Sim et al., 1993).

5.2.3 Extensive interconnectivity of synaptic vesicles

The analysis of the interaction between synaptic vesicles and connectors gave very similar results for untreated, HTS-treated synaptosomes and organotypic slices. More than 80% of the vesicles were linked to one or more of their neighbors via synaptic vesicle connectors (Figure 20A). For untreated synaptosomes, this fraction did not change significantly with increasing distance from the AZ (Figure 20B), despite the significant variation of vesicle concentration (Figure 19C). The number of connectors per vesicle was slightly higher in the distal zones of untreated synaptosomes (Kruskal-Wallis (K-W) test, $p < 0.05$ in both cases, Figure 20C) and did not differ significantly from HTS-treated synaptosomes and organotypic slices. About half of the connected vesicles had more than two connectors (Figure 21A).

The fraction of connected vesicles (in the whole terminal, Figure 20A, as well as in the proximal zone, Figure 20B) and the number of connectors per connected vesicle in the distal zones (Figure 20C) were significantly reduced in KCl-stimulated synaptosomes compared to untreated ones (Chi-square and K-W test respectively, $p < 0.001$ in all cases). OA-treated synaptosomes gave very similar results, except that in the proximal zone the fraction of connected vesicles did not differ significantly from untreated synaptosomes (Figure 20B). In TeTx-treated synaptosomes, connectivity was reduced only in the proximal zone (Chi-square test, $p < 0.001$, Figure 20B).

Connectors length was estimated by measuring the distance between their contact points with vesicles (Figure 20D, see 4.3). Connector length was only slightly higher than the (minimal) distance between connected vesicles, indicating that the connectors were very close to spanning the shortest path between vesicles. Almost all the connectors were shorter than 40 nm, and in untreated synaptosomes 87% of them were shorter than 20 nm (Figure 21B). Nevertheless, some of the longer connectors might have been missed due to noise. Connector length was not analyzed for organotypic slices because it might have been affected by cryosectioning-induced compression.



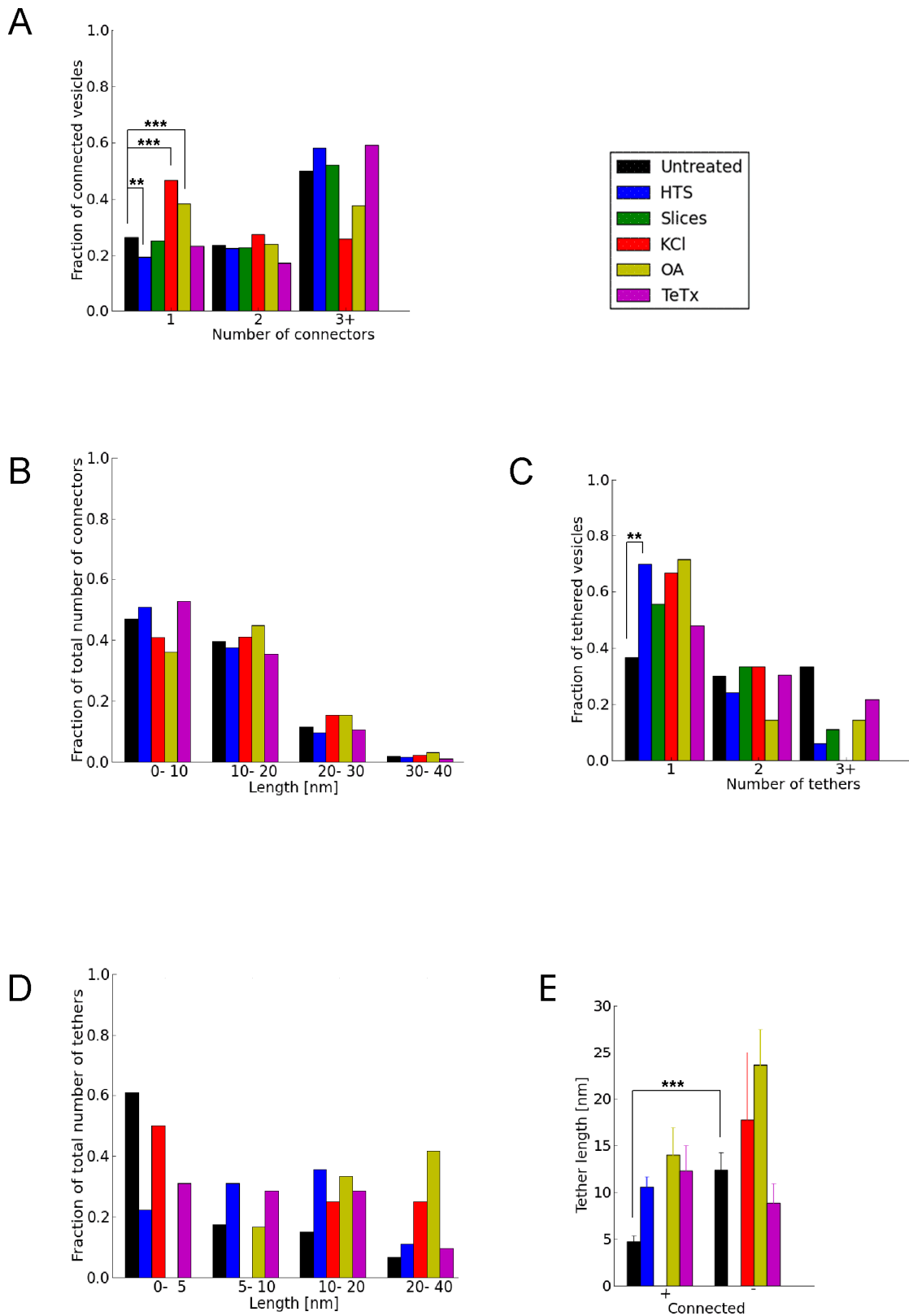


Figure 20 Synaptic vesicle connectors. (A) Fraction of connected vesicles for the first 250 nm from the AZ. (B) Fraction of connected vesicles vs. distance to the AZ. (C) Number of connectors per connected vesicle vs. distance to the AZ. (D) Connector length for the first 250 nm from the AZ. (E) Connector length vs. distance to the AZ. Plots show mean values and SEM (error bars). The confidence values are indicated by * for $p < 0.05$, ** for $p < 0.01$ and *** for $p < 0.001$. The numbers of vesicles (A, B) and connectors (C-E) analyzed for each treatment are shown in Table 1.

Figure 21 Length and number of connectors and tethers. (A) Histogram of numbers of connectors per connected vesicle. (B) Histogram of connector lengths. (C) Histogram of numbers of tethers per tethered vesicle. (D) Histogram of tether lengths. (E) Mean tether length for connected vesicles (left) and non-connected vesicles (right). The confidence values (calculated between histograms) are indicated by ** for $p < 0.01$ and *** for $p < 0.001$. The numbers of vesicles (A, C), connectors (B) and tethers (D, E) analyzed for each treatment are shown in Table 1.

The average connector length in untreated synaptosomes was significantly reduced in the proximal zone (K-W test, $p < 0.01$ in all cases, Figure 20E). OA treatment reduced connector length in the proximal and intermediate zones (K-W test, $p < 0.01$ and $p < 0.05$, respectively), but increased the length in both distal zones (K-W test, $p < 0.001$ in both cases). Taken together with the non-normal distribution of connector lengths (Figure 21B), these results suggest that more than one type of connectors is present and that OA has a differential effect on them.

5.2.4 Clusters of interconnected synaptic vesicles

Clusters of interconnected vesicles were defined as groups of vesicles all linked to each other via connectors. These clusters can be defined precisely and may underlie the closely packed groups of vesicles traditionally observed in EM. The study of such clusters revealed the influence of connectivity in vesicle distribution.

Typically, a presynaptic terminal contained more than twenty clusters of interconnected vesicles. Cluster size varied considerably, ranging from two vesicle clusters to large clusters of more than 50 vesicles. These large clusters dominated in untreated synaptosomes, comprising 61% of the connected vesicles (51% of all vesicles, Figure 22A). Figure 23A shows a visualization of the clusters of interconnected vesicles in an untreated synaptosome.

Under KCl stimulation large clusters were absent (Figure 22A) and the size of the largest cluster relative to the total number of vesicles in each terminal was reduced (K-W test, $p < 0.01$, Figure 22B). OA-treated synaptosomes showed an intermediate situation (Figure 22A), with the size of the largest cluster reduced compared to untreated ones (K-W test, $p < 0.01$, Figure 22B).

Clusters of interconnected vesicles extended considerably in the direction perpendicular to the AZ. In five out of seven untreated synapses at least one cluster spanned from the proximal to the distal zone. In contrast, this was observed only in

one out of six synapses treated with KCl. Vesicles in distal zones belonged to larger clusters than those in the proximal and intermediate zones (K-W test, $p < 0.001$ in all cases, untreated synaptosomes, Figure 22C). Compared to untreated synaptosomes, cluster size was reduced for KCl- and OA-stimulated synapses both in the proximal (K-W test, $p < 0.01$ in both cases) and distal zones ($p < 0.001$ in all cases), but clusters in OA-treated synaptosomes were still significantly larger than under KCl in the distal zones ($p < 0.001$). Note that spatial distribution of cluster sizes (Figure 22C) differed from that of vesicles (Figure 19) and vesicle connectivity (Figure 20B). All in all, synaptic vesicle clusters were significantly disrupted by KCl and to a lower extent by OA, even though both treatments caused a similar vesicle mobilization (Figure 19C).

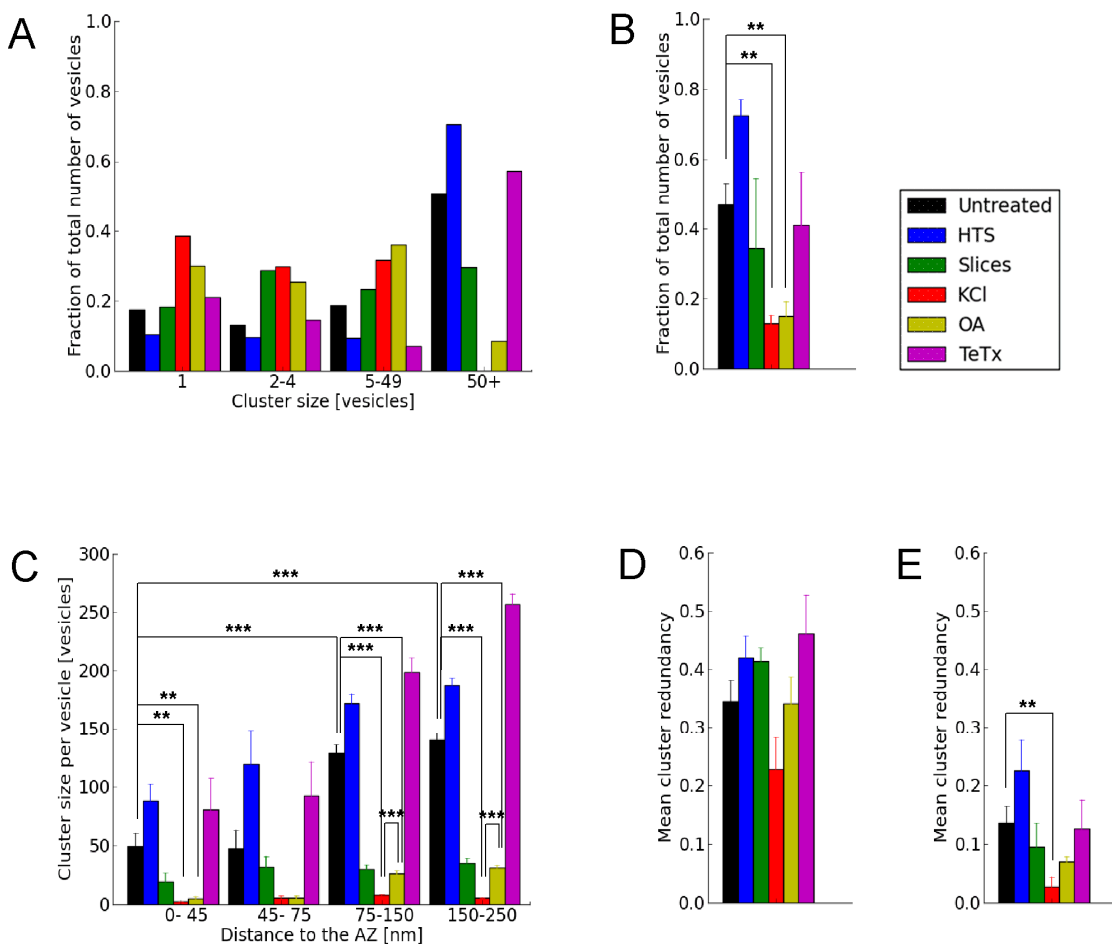


Figure 22 Synaptic vesicle clusters. (A) Histogram of cluster sizes (the size of a cluster is defined as the number of vesicles that belong to it). (B) Number of vesicles in the largest cluster as a fraction of the total number of vesicles. (C) Average size of the cluster each vesicle belongs to vs. distance to the AZ. (D) Redundancy for connectors when multiple connectors between two vesicles are considered (E) and ignored. Plots show mean values and SEM (error bars). The confidence values are indicated by ** for $p < 0.01$ and *** for $p < 0.001$. The number of vesicles analyzed for each treatment is shown in Table 1.

A more detailed analysis showed that vesicles were extensively interlinked within clusters, revealing a considerable degree of connector redundancy (see 4.3) (Figure 22D). When multiple connectors between two vesicles were treated as a single connector (termed *link*), only 14% of links could be removed without breaking clusters in the untreated case, compared with 3% after KCl treatment (K-W test, $p < 0.01$, Figure 22E). Also, a cluster shape index based on hierarchical clustering (taking values < 1 for globular clusters and > 1 for elongated ones, see 4.3) showed that in untreated synaptosomes clusters were predominantly elongated (index 1.7, t-test confidence level that it differs from 1.0, $p < 0.01$), while they were predominantly globular in the KCl case (index 0.88, t-test, $p < 0.05$), with no clear preference for the OA-treated synapses.

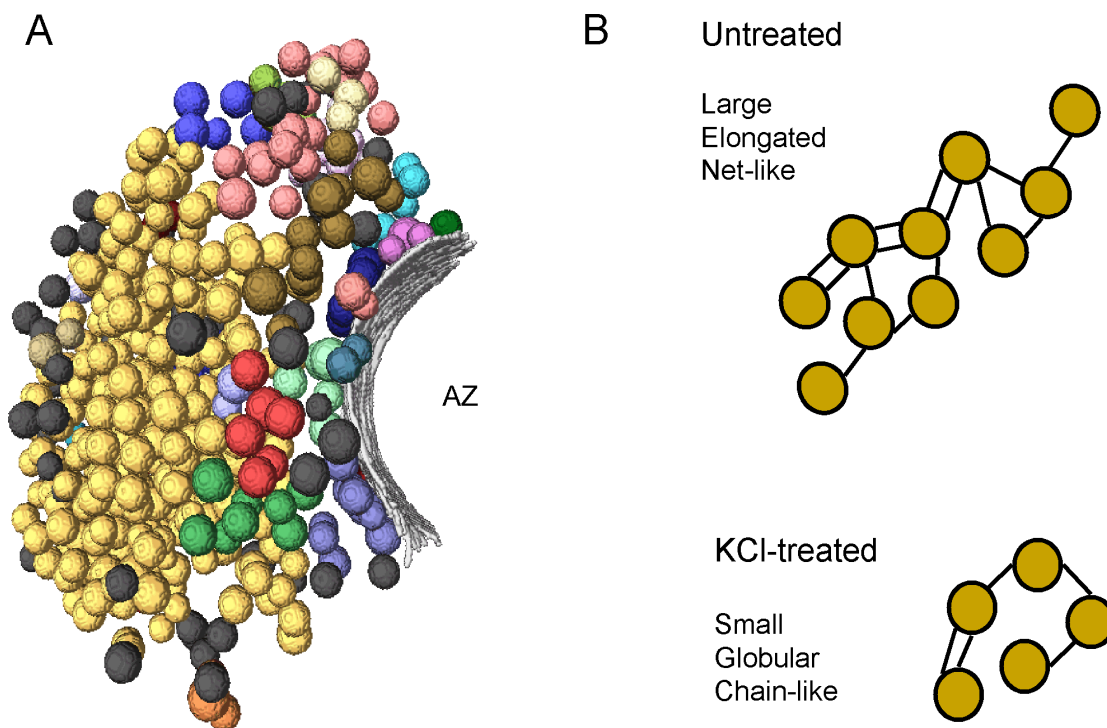


Figure 23 Morphology of synaptic vesicle clusters. (A) Visualization of synaptic vesicle clusters in an untreated synaptosome. Vesicles of the same color shade belong to the same cluster. Dark gray vesicles are not connected to others. (B) Topological analysis of clusters in untreated (up) and KCl-treated synaptosomes (down). According to the redundancy values from Figure 22D for connectors (Figure 22E for links), 5 out of 14 (2 out of 12) and 1 out of 5 (none) connectors (links) are redundant for untreated and KCl-treated synapses respectively.

In summary, clusters were large and elongated in untreated synapses, and the degree of connector and link redundancy revealed a net-like structure. In KCl-treated synapses clusters were small and globular, forming a chain-like structure with virtually no link redundancy. Figure 23B shows a quantitative representation of these two cluster types.

5.2.5 Tethering of proximal synaptic vesicles to the active zone

Filaments of variable length (Figure 24, Figure 25C) tethered the majority of the synaptic vesicles in the proximal zone to the AZ in untreated, HTS, TeTx-treated synaptosomes and organotypic slices, while tethering was significantly reduced for KCl and OA treatments (chi-square test, $p < 0.001$ in both cases, Figure 25A). All tethered vesicles were located in the proximal zone, and only rarely was there a direct contact between vesicle and AZ (see 5.2.7). Compared to untreated synapses, there was a significantly lower number of tethers per vesicle in the HTS-treated case, (K-W test, $p < 0.001$, Figure 25B), largely due to the low number of vesicles having more than two tethers (chi-square test, $p < 0.01$, Figure 21C).

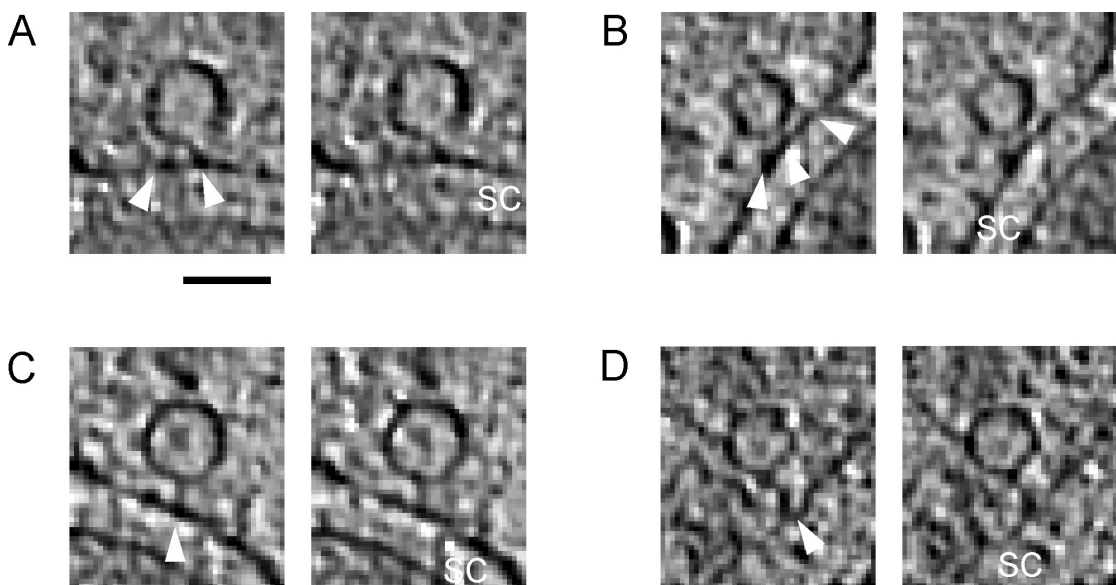


Figure 24 Short (< 5 nm; A, B) and long (> 5 nm; C, D) synaptic vesicle tethers (white arrowheads). Synaptic cleft (SC). Two consecutive 2.7 nm-thick tomographic slices are shown for each case. Scale bar: 50 nm.

HTS, TeTx and OA-treated synapses had a reduced number of short (< 5 nm) tethers (Figure 21D) that resulted in an increase of the average tether length (K-W test, $p < 0.001$ in all cases, Figure 25C). Thus, under hypertonic conditions, as well as TeTx treatment, tethered vesicles were held to the membrane by fewer tethers, and this reduction was mainly due to the loss of the short tethers. Images of short (A, B) and long (C, D) tethers are presented in Figure 24.

Conversely, when vesicles with more than two tethers were excluded from untreated synapses, the number of tethers per vesicle and the average tether length were indistinguishable from HTS- or TeTx-treated synaptosomes (Figure 25B and C). Therefore, these results showed that (i) vesicles released by HTS, i.e. those that form the RRP (Ashton and Ushkaryov, 2005), had a larger number of short tethers (more than two per vesicle, under these experimental conditions) and (ii) TeTx prevented the formation of short tethers.

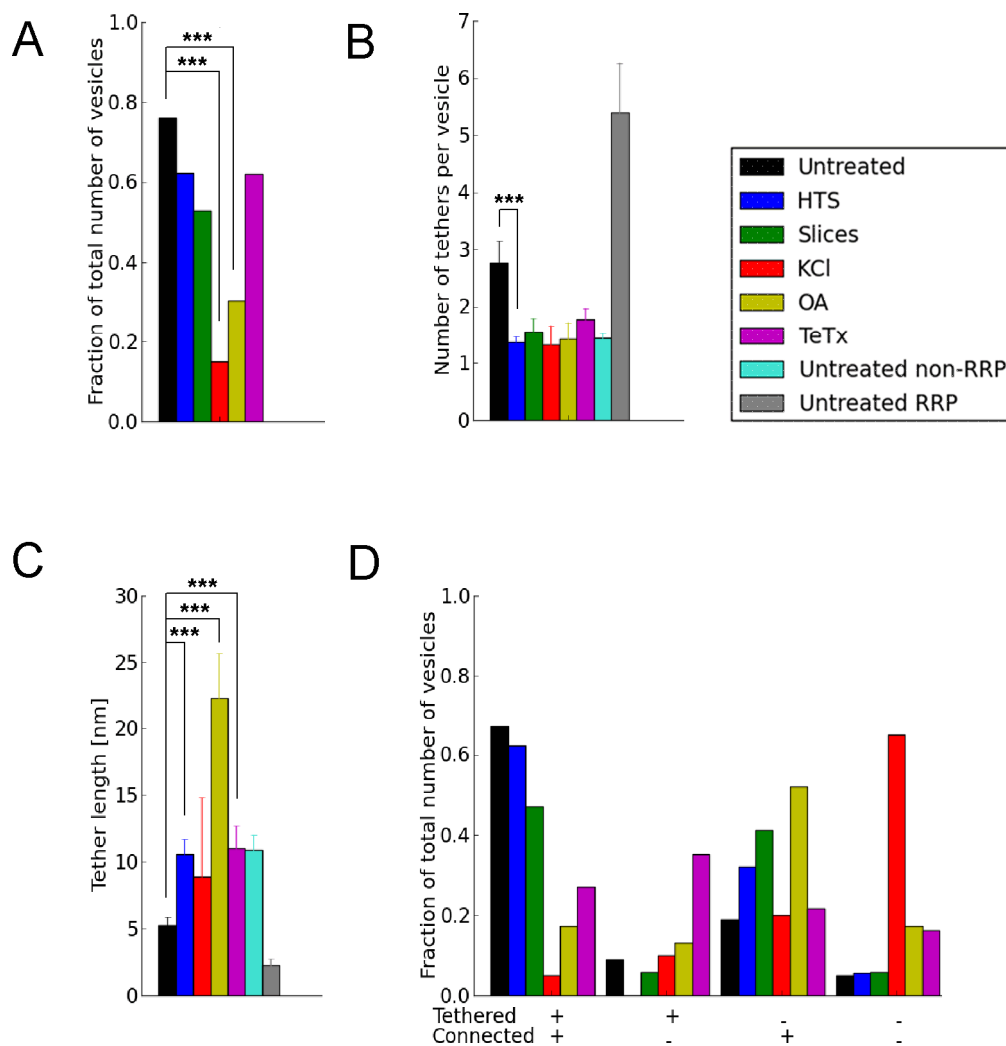


Figure 25 Synaptic vesicle tethers. (A) Fraction of proximal synaptic vesicles tethered to the AZ. (B) Average number of tethers per tethered synaptic vesicle. Untreated-RRP and untreated non-RRP: tethered vesicles with more than two and up to two tethers in untreated synaptosomes, respectively. (C) Tether length for all tethered vesicles. (D) Fraction of proximal synaptic vesicles as a function of tethering and connectivity. Plots show mean values and SEM (error bars). The confidence values are indicated by *** for $p < 0.001$. The numbers of vesicles (A, B, D) and tethers (C) analyzed for each treatment are shown in Table 1.

The relationship between tethering to the AZ and vesicle connectivity was also investigated. When vesicles were separated in categories according to their tethering and connectivity states, untreated and HTS-treated synaptosomes and organotypic slices showed a similar pattern (Figure 25D). Interestingly, tethers were significantly shorter for connected vesicles in untreated synaptosomes (K-W test, $p < 0.001$, Figure 21E), whereas tethering had no effect on connector length. Also, many tethered vesicles belonged to clusters of interconnected vesicles that reached the distal zones (21 of 60 tethered vesicles in 4 out of 7 untreated synapses), indicating a potential crosstalk between tethered and distal vesicles.

Tethers and other electron-dense structures emanating from the AZ that did not contact vesicles did not form regular patterns. Also, the positions of proximal vesicles and both types of densities were not correlated (Figure 26). It should be noted that the size of the cytosolic portion of the voltage-gated Ca^{2+} channels present at the AZ (Serysheva et al., 2002; Wolf et al., 2003) is beyond the resolution limit of this study.

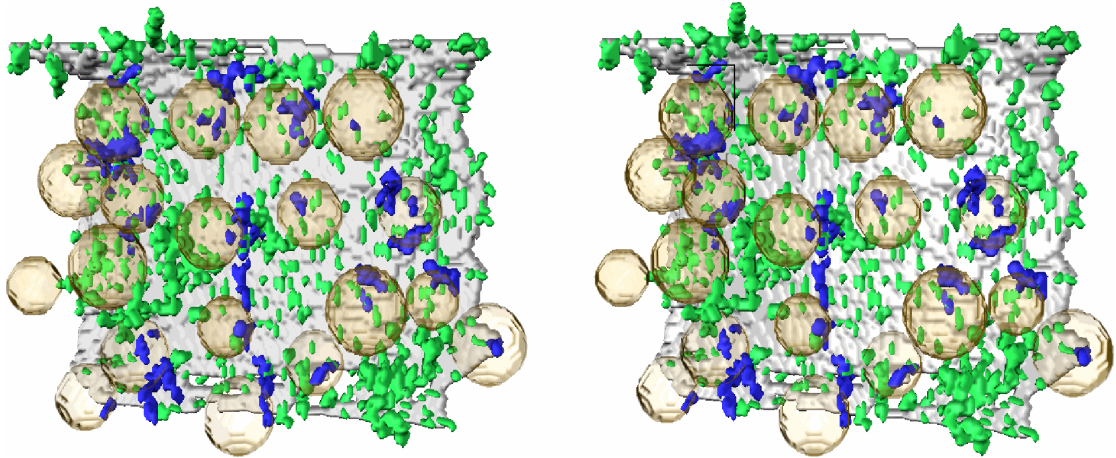


Figure 26 Stereo view of the mapping of the AZ membrane densities from the cytoplasmic side of a representative example of untreated synaptosomes: AZ (gray), proximal synaptic vesicles (partially transparent, yellow), synaptic vesicle tethers (blue), other protrusions of the AZ that do not contact the vesicles (green).

5.2.6 Synaptic vesicle size

Synaptic vesicle diameter in untreated synaptosomes was 41.6 ± 5.6 nm (mean \pm SD) and the distribution of diameters could be fitted by a Gaussian curve (Figure 27A). In untreated synaptosomes, vesicle diameter was slightly larger in the proximal zone than in all others (t-test, $p < 0.05$ in all cases, Figure 27C).

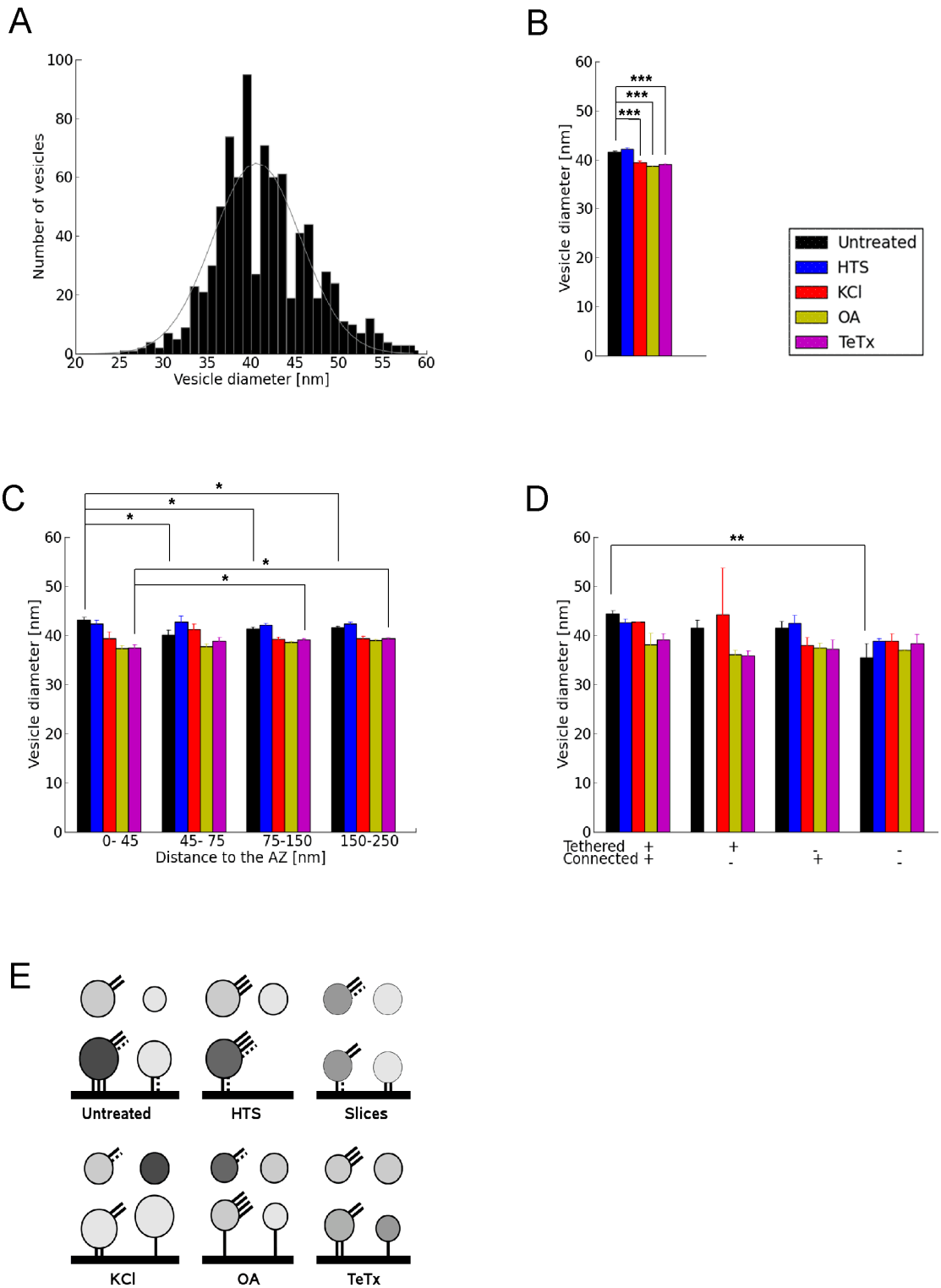
Synaptic vesicle diameter was significantly reduced for KCl, OA- and TeTx-treated synaptosomes (t-test, $p < 0.001$ in all cases; $\Delta V = -14\%$, $\Delta V = -20\%$ and $\Delta V = -17\%$ respectively, Figure 27B). This was not due to a difference in synapse type, since most of the analyzed synapses were excitatory (five out of six OA-treated, all TeTx-treated and six out of seven untreated synapses presented a strong postsynaptic density, see also 5.4.1). Interestingly, for KCl-treated synaptosomes there was no significant difference in the intermediate region with respect to the untreated case (Figure 27C).

In the proximal zone, the tethering and connectivity states of synaptic vesicles influenced vesicle diameter in untreated, HTS- and KCl-treated synaptosomes (Figure 27D). In untreated synaptosomes, tethered (connected) vesicles were larger than non-tethered (non-connected) ones. In particular, tethered and connected vesicles were much larger than non-tethered and non-connected (t-test, $p < 0.01$, $\Delta V = +100\%$,

Figure 27D). Considering the first 250 nm from the AZ, connected vesicles were only larger in OA-treated synapses (t-test, $p < 0.01$, $\Delta V = +11\%$, data not shown). As vesicles were significantly compressed in slices, their diameter was not measured. A semi-quantitative representation summarizing the values for vesicle size, connectivity and tethering for the different groups of samples is shown in Figure 27E. There was no correlation between tethering or connectivity and the electron density of the vesicle lumen, irrespective of whether WBP or SIRT were used for tomographic reconstruction.

These data suggests that the vesicles in the proximal region can be divided in two groups based on their size: (i) large, i.e. those tethered or connected in untreated and HTS-treated synapses and (ii) small, i.e. those non-tethered and non-connected in untreated and HTS-treated synaptosomes, as well as all vesicles from OA- and TeTx-treated synapses. There was no statistical difference between tethered and non-tethered vesicles from KCl-treated synapses due to the low number of proximal vesicles for this treatment.

Figure 27 Synaptic vesicle diameter. (A) Diameter histogram and the corresponding Gaussian fit. (B) Diameter for the first 250 nm from the AZ. (C) Diameter vs. distance to the AZ. (D) Diameter of proximal vesicles as a function of tethering and connectivity. Plots show mean values and SEM (error bars). The confidence values are indicated by * for $p < 0.05$ and ** for $p < 0.01$. The number of vesicles analyzed for each treatment is shown in Table 1. (E) Semi-quantitative representation of the properties of proximal synaptic vesicles shown previously. Four circles are depicted for each condition, representing non-tethered, connected vesicles (upper left), non-tethered, non-connected vesicles (upper right), tethered, connected vesicles (lower left) and tethered, non-connected vesicles (lower right). In each case, the diameter of the circle is linearly dependent on the vesicle diameter (except for organotypic slices, where synaptic vesicle diameter was not measured), and its filling grayscale value indicates the fraction of vesicles present in that category (white corresponds to 0 and black to 1). Connectors are represented as oblique lines emanating from the vesicles. The number of lines emanating from a vesicle indicates the average number of connectors per vesicle in that category (dashed lines represent half connector). The AZ is represented by thick horizontal lines. The number of lines linking a vesicle to the AZ represents the number of tethers. The distance between tethered vesicles and the AZ is proportional to the averaged measured value. Note that the lengths of tethers and connectors are not related to their measured values.



5.2.7 Direct membrane contact between synaptic vesicles and the active zone

In the synaptic preparations examined here, direct membrane-to-membrane contact between synaptic vesicles and the AZ was rarely observed and only found in tomograms of untreated synaptosomes. However, these contacts appeared to be more common in tomograms of synaptosomes inoculated with herpes simplex virus 1 (HSV-1; Maurer et al., 2008), which were included in this analysis. Vesicles associated with the AZ were captured either with an open pore (Figure 28A, N = 2) or making contact with an invagination of the AZ (Figure 28B, N = 4). Patches of AZ of unusually high, concave curvature (Figure 28C, N = 2), likely signatures of full-collapse fusion events were also observed. These snapshots (Figure 28) correspond well to the recently proposed steps of synaptic vesicle fusion (Figure 2 in Martens and McMahon, 2008).

Each of the two vesicles observed with an open pore at the AZ retained an almost spherical shape, forming an approximately cylindrical neck of ~ 19 nm in length and 14 nm outer diameter that contained an aqueous channel with a diameter of ~ 3 nm. Interestingly, both vesicles were connected to their neighbors and showed no signs of clathrin coating or dynamin rings.

A prominent L-shaped density was detected close to the AZ invagination for three out of four vesicles making membrane contact with the AZ (blue arrowhead in Figure 28B). The density consisted of two arms, one shorter (~ 14 nm) contacting the vesicle and a longer one (~ 17 nm) contacting the AZ. The arms formed angles between 100° and 140° , showing higher density at their junction. Remarkably, a similar L-shaped density was observed on the side of the necks for vesicles with an open pore (Figure 28A), but in this case the arm contacting the AZ was considerably fainter than the vesicular arm. Thus, such density was detected in five out of six examples of vesicles directly associated with the cell membrane. In contrast, it was not observed in any of fifteen randomly chosen tethered vesicles, indicating that the formation of the L-shaped density was preferentially correlated with the direct membrane contact between vesicles and the AZ (K-W test, $p < 0.001$).

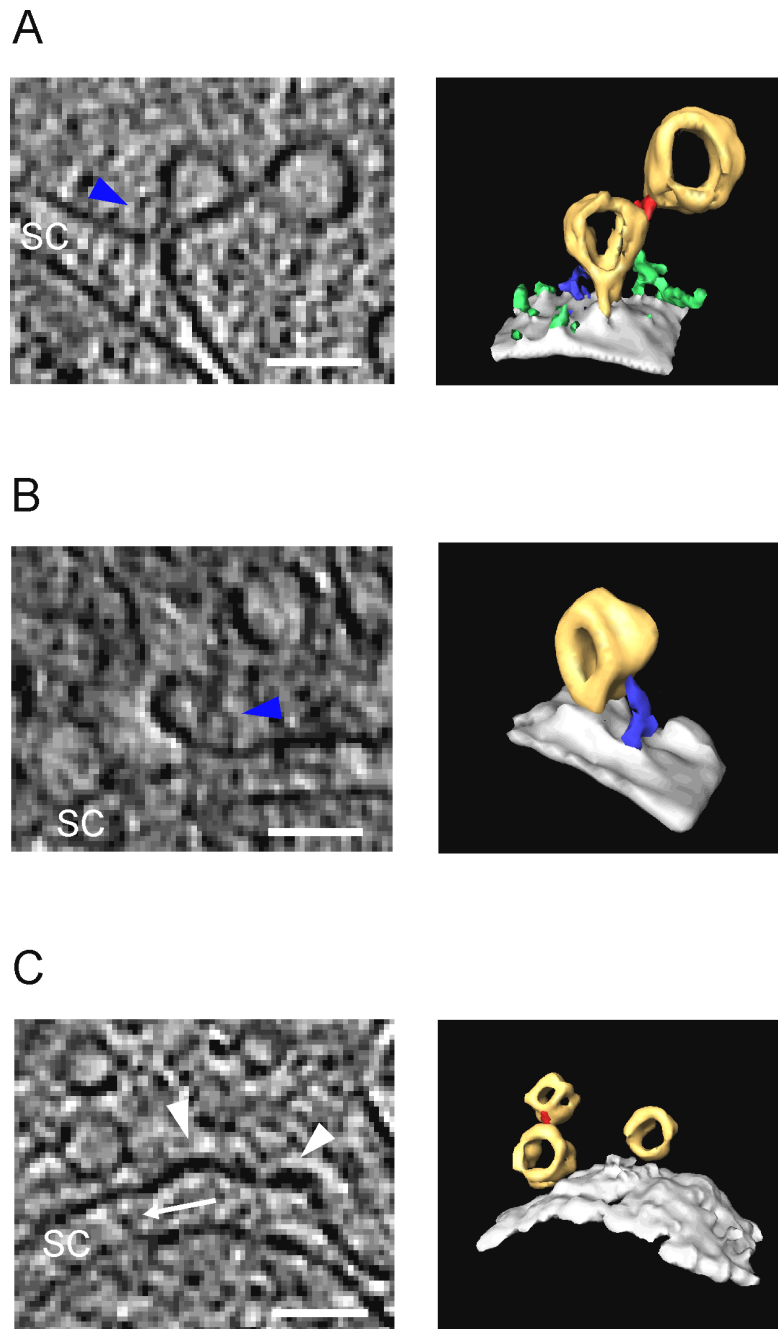


Figure 28 Direct membrane contact between synaptic vesicles and the AZ. Synaptic cleft (SC). 2.7 nm-thick tomographic slices are shown in the left and the corresponding direct 3D rendering of the EM densities on the right: synaptic vesicles (yellow), synaptic vesicle connectors (red), AZ (gray), synaptic vesicle-associated densities (blue), other AZ densities (green). (A) Synaptic vesicle with an open neck, which establishes continuity between the vesicular lumen and the extracellular space. An L-shaped density is visible close to the neck (blue arrowhead). (B) Synaptic vesicle making membrane contact with an invagination of the AZ. An L-shaped density is present close to the AZ invagination (blue arrowhead). (C) Regions of the AZ with high concave curvature (white arrowheads), likely signatures of full-collapse fusion events. A vesicle is tethered by a filament that traverses the presynaptic membrane and extends into the synaptic cleft (white arrow). Scale bars: 50 nm.

5.3 Computational procedures for the analysis of presynaptic architecture

In a previous study, Vladan Lučić presented an algorithm for the semi-automated segmentation of the complexes present in the synaptic cleft (Lučić et al., 2005b). This method required the manual delineation of pre- and postsynaptic membranes and of the space corresponding to the synaptic cleft using three-dimensional segmentation software such as Amira. Then, the algorithm would segment out the complexes found in the cleft region that were connected to both cellular membranes, and analyze their topological characteristics.

Analogously, connectors and tethers spanned the distance between two membranes, and preliminary tests indicated that they could be successfully detected by this algorithm. However, the process was extremely time-consuming, as it required the manual segmentation of the AZ, the vesicles and the portion of cytoplasm between each pair of vesicles (or between each vesicle and the AZ). Furthermore, the detection of connectors and tethers with this method was not comprehensive as it depended on the local background density.

A first step towards automation consisted in circumventing the manual segmentation of synaptic vesicles, which were substituted by spheres. For that, the position of the center of each vesicle and its radius were determined from the outline of the central xy slice. The number of connectors obtained at each threshold was similar for manually traced vesicles and spheres, indicating that spheres were a good approximation for vesicles (Figure 29), in agreement with previous reports (Harris and Sultan, 1995). Vesicles in cryosections were segmented by manually delineating their membrane in all xy slices, since they were elongated due to cutting-induced deformations.

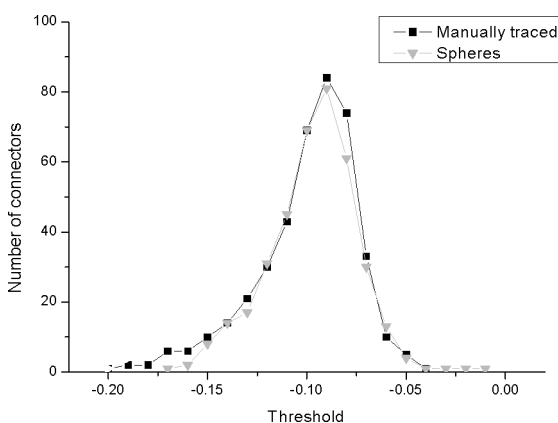


Figure 29 Number of connectors detected for manually traced vesicles (black squares) and spheres (grey triangles) within the significant threshold range for a representative synaptosome.

Connectors were defined as groups of neighboring voxels (with values below a given threshold) that contacted the membranes of two vesicles, and tethers as such groups of voxels contacting the AZ and one vesicle (Figure 30). Structures connecting more than two boundaries were not analyzed, as they were rare and generally did not correspond to visually identifiable filaments. Filamentous structures emanating from the AZ that did not contact any other material of the mask are referred as

*protrusions*¹¹ in this section. In order to speed up the computation, the search for connectors, tethers and protrusions was restricted to a portion of cytoplasm at a limited distance of vesicles and AZ (Figure 31A). The number of detected filaments was independent of the distance for values above 27 nm (10 voxels, Figure 31B), and consequently this distance was used thereafter.

The notion of “neighboring voxels” is also subjected to definition, as (cubic) voxels can contact their neighbors either with a face, an edge or a vertex. For vertex connectivity a large amount of structures that did not correspond to observable filaments was detected. There were only small differences between edge and face connectivity, but maximum agreement with visually clear filaments was reached for the latter.

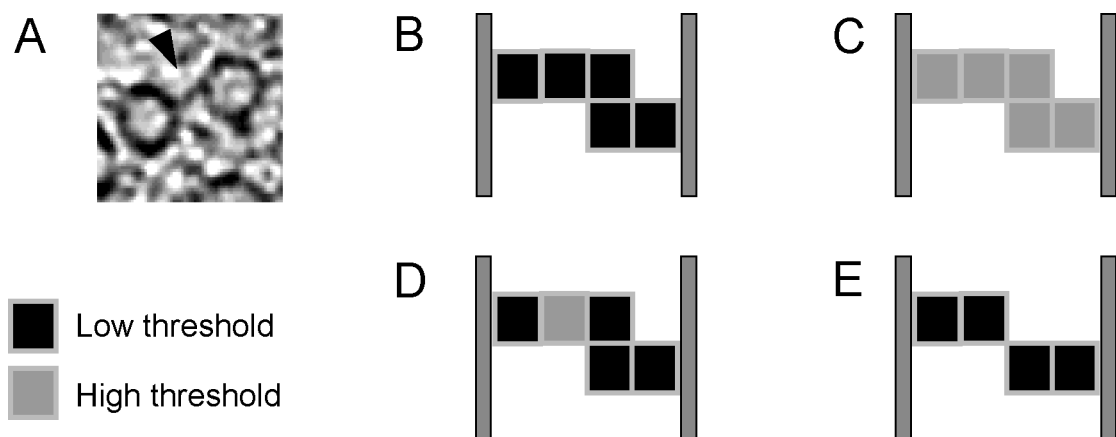


Figure 30 Schematic representation of the automated detection of segments. (A) 2.7 nm-thick tomographic slice showing a connector (black arrowhead) between two vesicles. (B-E) Segments consist of voxels (black/grey boxes) contacting two membranes (dark grey vertical lines). In (B), the segment is detected at low threshold. The segment in (C) is lighter, and therefore it is detected only at high threshold. The same is true for the segment in (D), where only one voxel is lighter than the rest (this typically occurs due to the noise). The structure in (E) is not detected as a segment at any threshold because voxels are separated into two disjoint groups (only voxels with faces that contact each other belong to a same group).

¹¹ The word *segment* will be used from here on to designate all the structures automatically detected by the algorithm (i.e., connectors, tethers and protrusions).

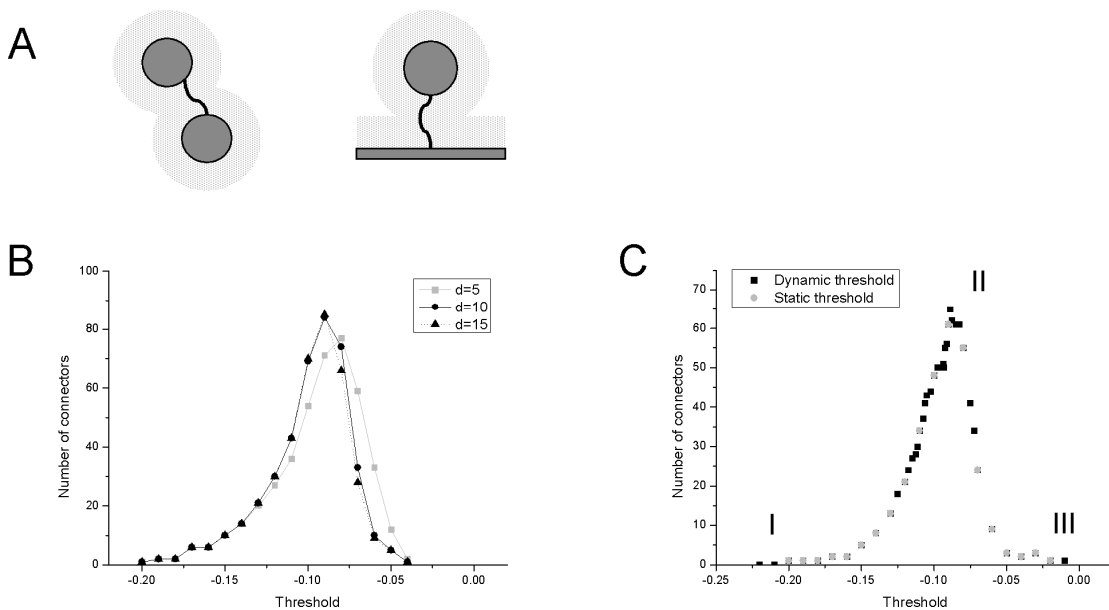


Figure 31 (A) Detection of connectors (left) and tethers (right). Synaptic vesicles (dark grey spheres), AZ (dark grey thick line), connectors and tethers (thin black lines), portion of cytoplasm where connectors and tethers were searched (light grey density around vesicles and AZ). (B) Dependence of connector number on the size (d , in voxels) of the portion of cytoplasm where connectors are searched, for a representative synaptosome within the significant threshold range. Voxel size: 20.1 nm^3 . (C) Number of connectors detected for a representative synaptosome using the fixed (grey) and dynamic (black) threshold schemes, within the significant intensity range. No segments were detected for very low thresholds (I) and the number increased exponentially as the threshold increased, eventually reaching a maximum (II). Further increasing the threshold reduced the number of connectors/tethers as they started to merge with each other. Beyond a certain high threshold value all the detected structures merged into a single segment (III).

5.3.1 Hierarchical classification of connectors and tethers

The number of detected segments depends on the chosen threshold. For very low thresholds (considering only very dark voxels), only a few structures were found, and they generally corresponded to actual filaments in the tomogram. However, many filaments slightly affected by noise were missed. For higher thresholds the number of detected segments was higher, but many of the segments detected at lower thresholds merged together, contacting several vesicles. Intermediate thresholds showed an undesirable mixture of the two cases, and consequently no single threshold provided an optimal representation.

The number of connectors/tethers detected at equidistant thresholds within the significant intensity range (from the lowest gray-scale values of a tomogram to the average gray-scale value) is shown in (Figure 31C). It can be seen that at extreme thresholds the difference in the number of detected segments between successive thresholds was small, whereas it changed considerably at intermediate thresholds. A large difference in the number of segments at successive thresholds could have negative consequences for the subsequent hierarchical classification of connectors and

tethers, and thus a dynamic threshold step was implemented, allowing a similar number of segments to be detected for every new threshold¹². This algorithm started detecting segments at the lowest threshold and moved towards higher grey-scale values, with a given threshold step. A tolerance measure (K) was introduced, so that the number of new detected segments between one threshold and the next should always remain smaller than K . If more segments were detected, an intermediate threshold was analyzed. This cycle was iterated until the number of new segments detected between each pair of thresholds was smaller than K . However, the dynamic and the fixed increment threshold schemes yielded essentially the same results (Figure 31C).

The morphological characteristics of individual segments also depended on the threshold, because segments grew in size with increasing thresholds, as more voxels had values below the new threshold. Eventually, as the threshold continued to increase, the segment merged with a neighboring one and was discarded if it contacted more than two membranes. When compared with the filaments observed by eye, the best visual impression usually corresponded to the lowest threshold value at which the segment was detected.

This idea allowed us to introduce a hierarchical classification scheme for connectors and tethers and protrusions. After analyzing all thresholds within the significant intensity range, each individual segment was stored at the lowest threshold where it was detected (Figure 32, Figure 33). Then, all segments detected at different thresholds were merged into a one single set, which combined the advantages of low and high thresholds. Furthermore, the exact threshold values had negligible influence as most of the segments were detected at intermediate thresholds. Thus, difficulties associated with uneven background levels, as well as the choice of a particular threshold were avoided.

In the case of protrusions of the AZ the opposite criterion was desirable: filaments were stored at the highest threshold in which they appeared, before merging with neighboring filaments. In this way, the full length of the filament could be consistently detected. In contrast, since connectors and tethers were limited by two membranes, their full length was already detected at the lowest possible threshold.

In summary, tomograms of presynaptic terminals were analyzed as follows:

1. A segmentation mask was created, in which the AZ was manually traced and synaptic vesicles were substituted by spheres of the corresponding diameter (vesicles in cryosections were segmented manually).
2. Filaments linking vesicles to each other (connectors) and to the AZ (tethers), as well as protrusions from AZ, were detected at all thresholds within the significant intensity range.
3. Segments were hierarchically classified and, in the case of connectors and tethers, stored at the lowest threshold in which they were detected. Protrusions were stored at the highest threshold possible before merging with other filaments.

¹² Alternatively, a very fine threshold step could have been used for the whole intensity range, but this approach would have been much more computationally expensive.

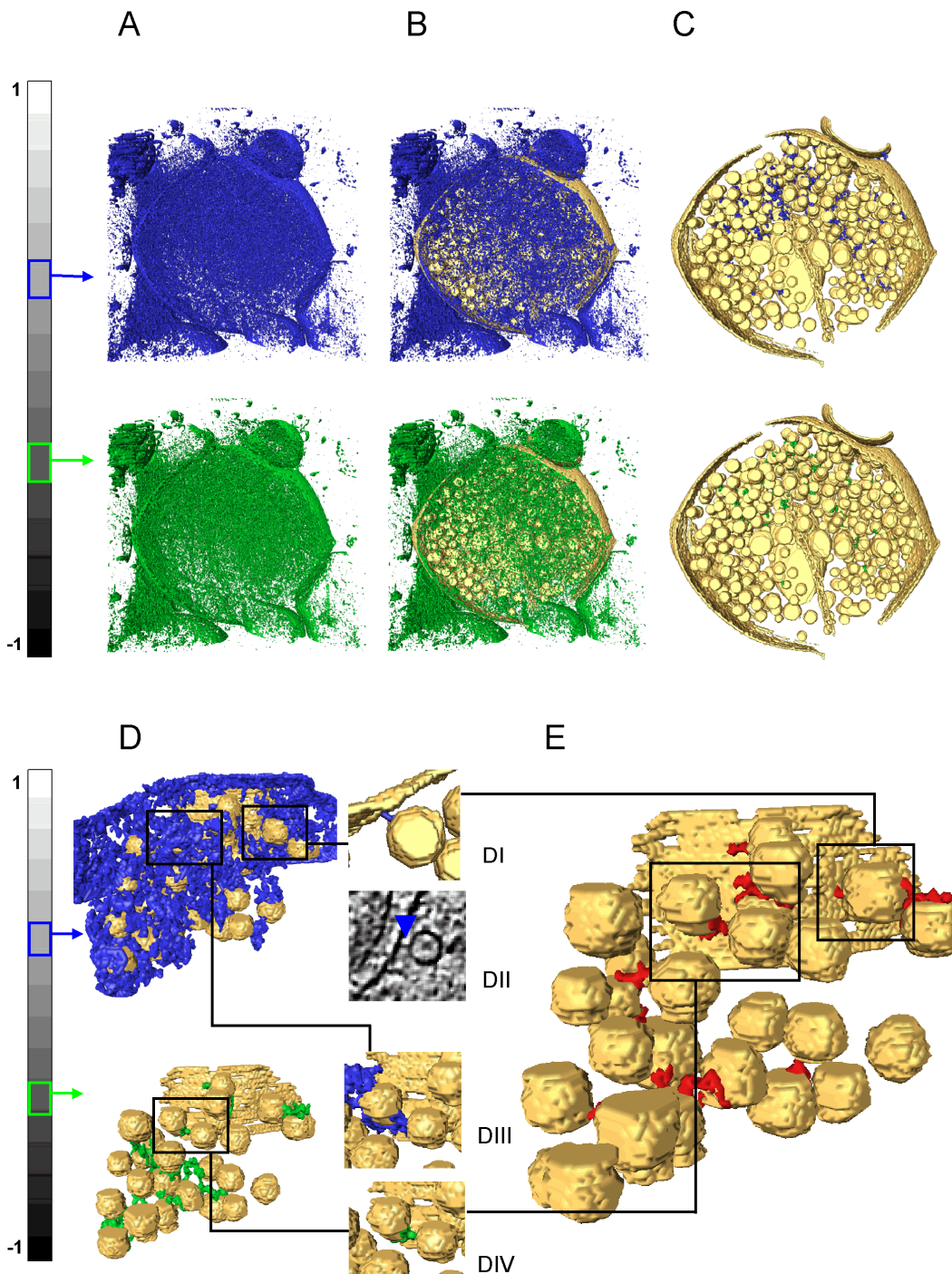


Figure 32 Hierarchical classification of connectors and tethers. (A) The tomogram is thresholded at discrete values within the significant intensity range. A higher (blue, above) and a lower (green, below) thresholds are shown. (B) The segmentation mask, showing the synaptic vesicles and the cell membrane (yellow), is superimposed on the thresholded data. In this particular mask vesicles were manually segmented and a mitochondria and a microtubule were also included, but were not considered for the detection of segments. (C) In this case, segments that connect at least two materials of the mask are kept. (D) Close up of the segments detected close to the AZ at lower (green) and higher (blue) thresholds. A clearly visible tether (DII) is detected only at the higher threshold (DI). A connector detected at the lower threshold (DIV) merged with neighboring segments at higher threshold (DIII). In the final set (E), each segment is stored at the lowest threshold where it was detected.

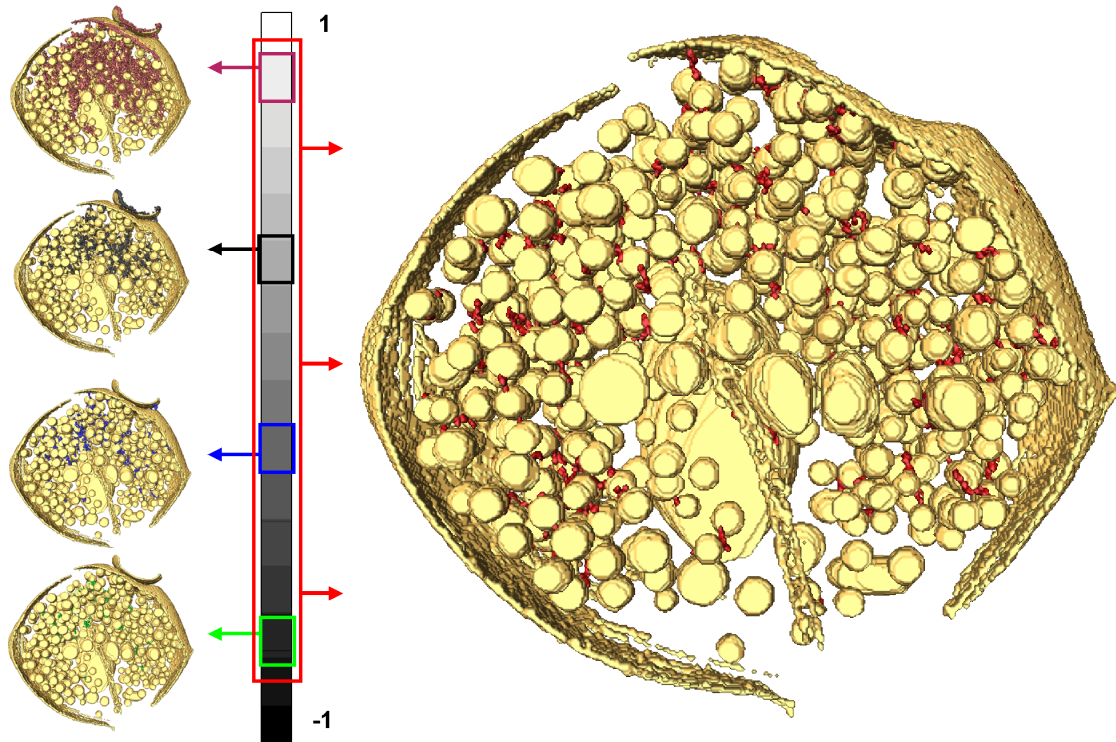


Figure 33 Alternative representation of the hierarchical classification of connectors and tethers. Segments were detected at different thresholds (left) and merged into a single set in which each segment is stored at the lowest threshold where it was detected (right).

For connectors and tethers, the procedure above resulted in segments that agreed well with the visually identified structures. However, when all segments that contacted at least one membrane (synaptic vesicle or the AZ) were considered, an additional classification step was required. A clear relationship was observed between the size of the segment (measured as volume in voxels) and its correspondence with visually identifiable structures in the tomograms. Thus, almost all small segments (≤ 150 voxels¹³) correlated well to filaments that could be visually detected (Figure 34A). In contrast, only few structures of volume up to 600 voxels did correspond to filaments observable in the tomogram. Larger structures invariably corresponded to false positives. As a conservative criterion, only segments smaller than 150 voxels can be considered to correspond to actual structures.

¹³ voxel volume was 20.1 nm^3 for tomograms recorded at CM300 and 18.4 nm^3 for Polara, see 4.2

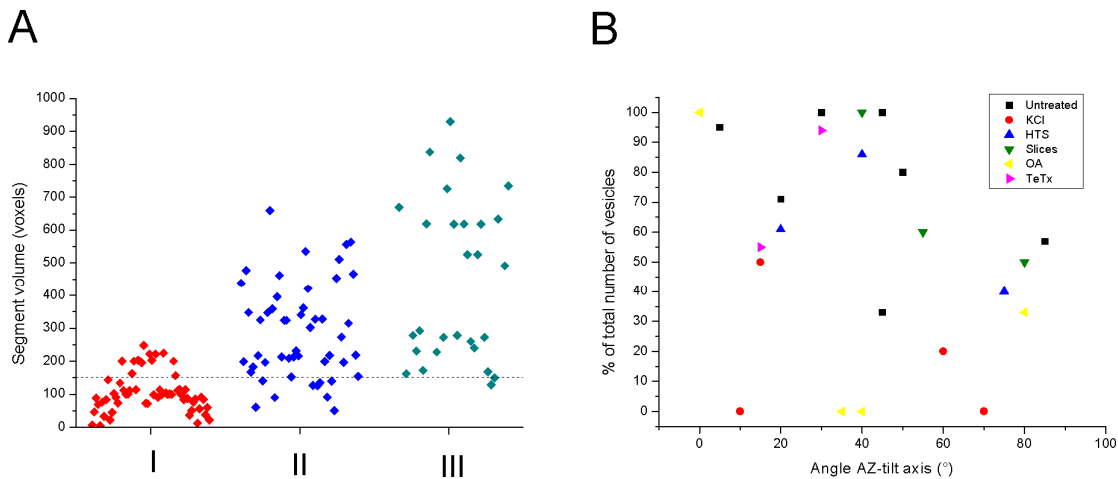


Figure 34 (A) Correspondence between detected segments and visually identified filaments, as a function of segment volume. Segments from group I (red) corresponded to clear filaments, group II (blue) to possible but unclear filaments and group III (green) did not correspond to filaments at all. The dashed line marks the established volume cut-off (150 voxels, voxel size: 20.1 nm^3). Data pooled from two representative synaptosome tomograms. In this case, segments contacting at least two membranes were considered. (B) Vesicle tethering as a function of the AZ angle with the tilt axis.

Other morphological criteria were also tested in order to detect false positives. For example, it was observed that segments with surface-to-volume ratio 1 (i.e., “thin” segments) invariably corresponded to visually identifiable connectors or tethers. However, the interpretation of slightly smaller ratios was unclear, and this criterion was consequently not used. The final set of connectors and tethers used for analysis (5.2) matched well the filaments visually observed in the tomograms (Figure 18).

In order to minimize the influence of the missing wedge, tomograms of synapses with different orientations of their AZs in respect to the tilt axis were recorded. The number of detected tethers showed only a weak and statistically non-significant dependence on the AZ orientation (Figure 34B).

All the procedures for segmentation and analysis described in this section were conceptually designed and tested by RF-B and Vladan Lučić, and implemented in Python by Vladan Lučić.

5.4 Observations on other neuronal structures

5.4.1 The postsynaptic density and the synaptic cleft

The vast majority of synaptic contacts in the brain are excitatory, using glutamate as neurotransmitter. Glutamatergic synapses are also called *asymmetric*, as in

conventional EM they are characterized by a strong postsynaptic density (PSD). In contrast, the PSD is not so distinct in inhibitory, *symmetric* synapses (Gray, 1959).

In more than 80% of vitrified, frozen-hydrated synaptosomes the PSD appeared as an electron dense band attached to the postsynaptic membrane (Figure 35A). The PSD was in all cases directly apposed to the presynaptic terminal and had similar extension to the AZ and the synaptic cleft. It was ~40-60 nm thick, but occasionally long protrusions were projected into the postsynaptic cytoplasm (Figure 35B). Circular structures of ~20 nm in diameter were embedded in the PSD, which were reminiscent of the calcium/calmodulin-dependent protein kinase II (CaMKII, Figure 35D, E) (Gaertner et al., 2004), the most abundant protein within the PSD (Kennedy et al., 1983b). Actin filaments often impinged the periphery of the PSD (Figure 35A). OA-treatment resulted in significant PSD dispersal (observed in 8 out of 13 OA-treated synaptosomes vs. none out of 9 untreated, Figure 35C), suggesting that this phenomenon could correspond to the structural rearrangements of the PSD induced by increased phosphorylation under prolonged synaptic activity (Dosemeci et al., 2002; Sheng and Hoogenraad, 2007).

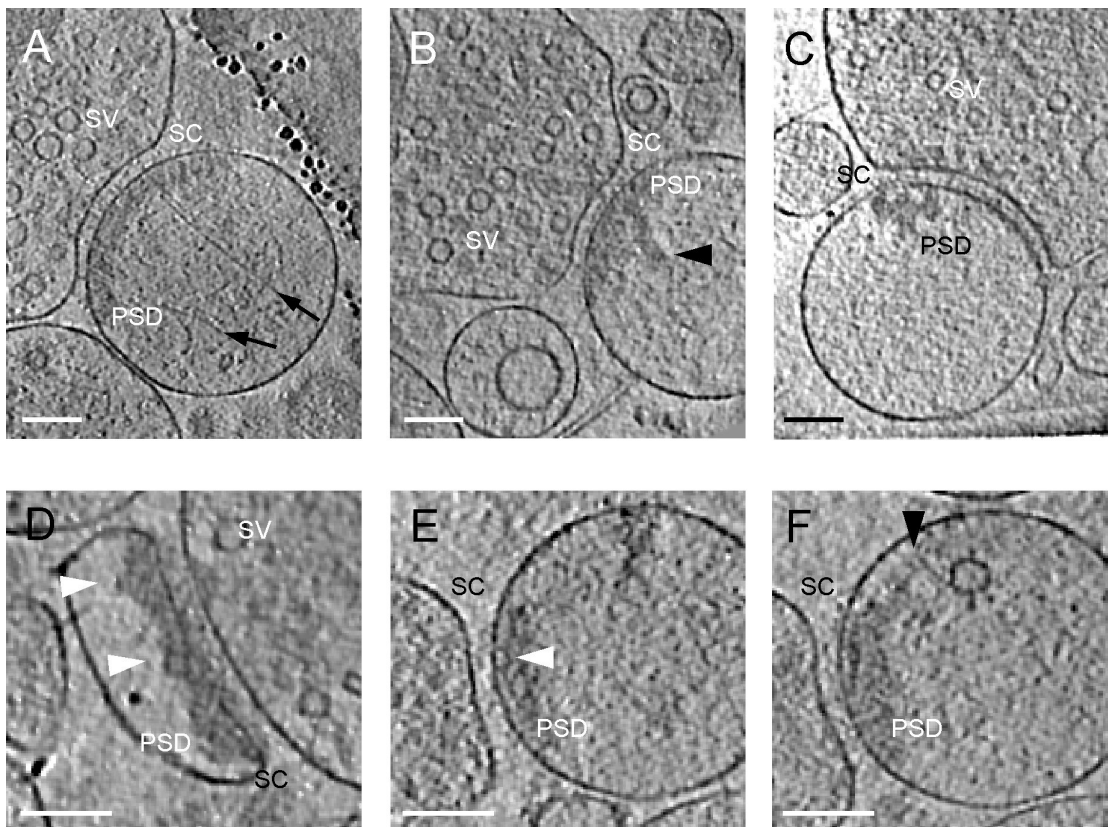


Figure 35 Observations on the PSD. In all panels tomographic slices are 2.7 nm-thick. Synaptic vesicle (SV), synaptic cleft (SC), postsynaptic density (PSD). (A) PSD of uniform thickness impinged by an actin filament (black arrows). (B) Protrusion of the PSD (black arrowhead). (C) PSD dispersal upon OA treatment. (D, E) Circular structures embedded in the PSD (white arrowheads). (F) Postsynaptic vesicle linked to the PSD (black arrowhead). Scale bars: 100 nm.

Membrane-bound structures, such as ER fragments, endosomes or multivesicular bodies were common in postsynaptic terminals. In the vast majority of terminals, small vesicles of ~50 nm of diameter were also present. These vesicles often contained electron dense particles in their lumen and prominent membrane densities. Occasionally, these vesicles were associated with cytoskeletal elements, and sometimes in direct contact with the PSD, suggesting that they could play a role in protein traffic to or from the PSD (Figure 35F).

Pre- and postsynaptic terminals were separated by the ~25 nm wide synaptic cleft. Numerous cell adhesion complexes are present in the cleft, forming a dense net-like structure (Lučić et al., 2005b). It was possible to clearly distinguish individual complexes (Figure 36A, B), some of which traversed the cell membrane and extended into the pre- and postsynaptic cytoplasm, even functioning as synaptic vesicle tethers (Figure 28C). This opens interesting possibilities, given the implication of cell adhesion molecules in the regulation of the synaptic vesicle cycle (Gottmann, 2008). Structures attached to the postsynaptic membrane reminiscent of the extracellular regions of glutamate receptors (Sobolevsky et al., 2009) were also observed (Figure 36C, D).

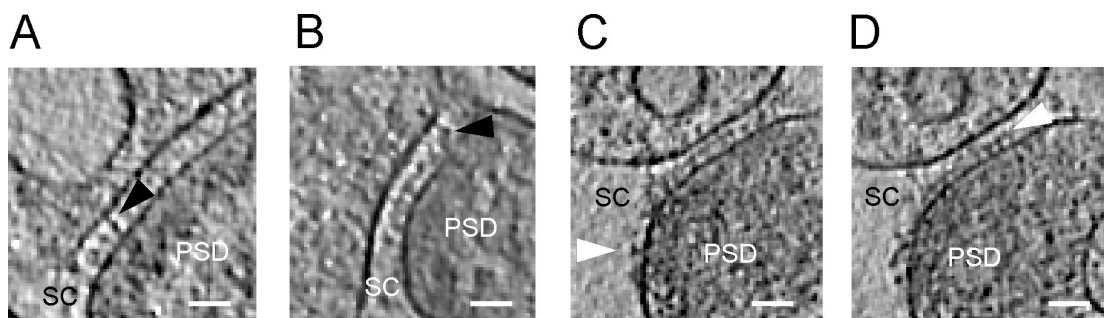


Figure 36 Observations on the synaptic cleft. In all panels tomographic slices are 2.7 nm-thick. Synaptic cleft (SC), postsynaptic density (PSD). (A, B) Individual molecular complexes in the synaptic cleft (black arrowheads). (C, D) Postsynaptic molecules reminiscent of glutamate receptors (white arrowheads). Scale bars: 50 nm.

5.4.2 Morphology of neurons in culture

In this study, frozen-hydrated neuronal cultures vitrified after 6-7 DIV were examined. At this stage, significant stretches of neuronal processes are still thin enough for EM investigation. In axons, varicosities (characterized in Sasaki-Sherrington et al., 1984) that contained large groups of synaptic vesicles were abundant. Other organelles such as mitochondria or multivesicular bodies were also present in these varicosities, often embedded in a very dense actin network (Figure 37A). Microtubules were observed in all neuronal processes and in axonal varicosities in particular. Interestingly, synaptic vesicles were connected to each other by similar filaments as those detected in mature synapses (Figure 37B-D; see 5.2.3), and they were sometimes linked to the actin cytoskeleton by similar strands (Figure 37E, F). In cryosections of organotypic slices,

groups of interconnected vesicles linked to microtubules by connectors were also found (Figure 37G).

In addition, a putative nascent synaptic contact was observed (Figure 38A). This structure was formed by an axon and a dendrite running parallel, separated by a ~25 nm space that contained electron dense material. However, the width of this space was not as homogenous as in mature synapses. In the axon, a high number of microtubules were present, together with several synaptic vesicles and endosome-like organelles, as described for forming synapses in (Ahmari et al., 2000). The vesicles were sparse but accumulated in the proximity of the cell membrane. Weak densities seemed to connect vesicles to each other or to the cell membrane, and some vesicles were also connected to longer, actin-like filaments (Figure 38B, C). Hundreds of electron dense complexes reminiscent of ribosomes (Ortiz et al., 2006) were present on the postsynaptic side, surrounded by numerous microtubules. This synaptic structure extended for approximately 1 μm . In the surrounding area the morphology of both axon and dendrite was markedly different, showing few synaptic vesicles and ribosomes (Figure 38D).

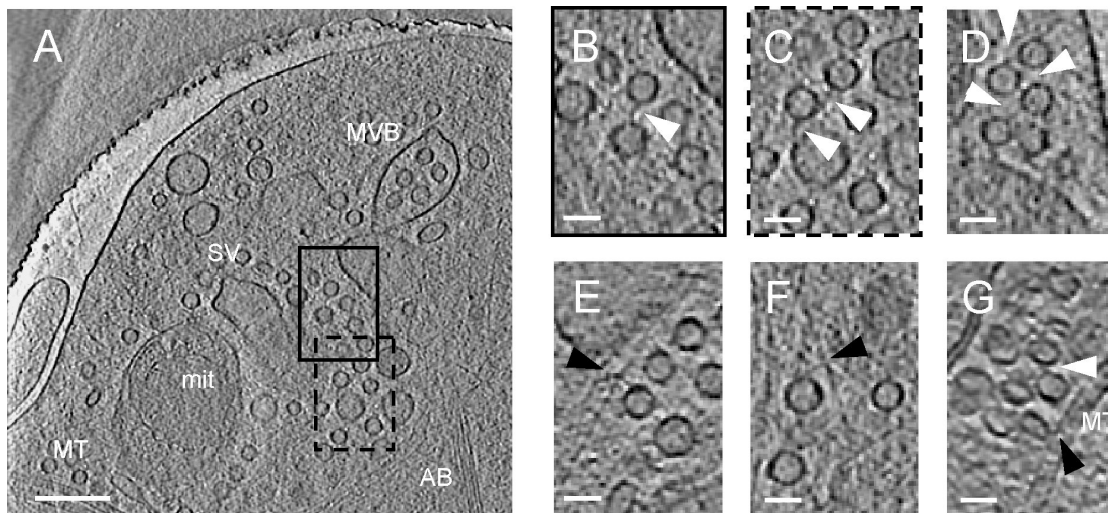


Figure 37 Vesicle connectivity in 6 DIV neuronal cultures. In all panels tomographic slices are 3.3 nm-thick. Synaptic vesicle (SV), mitochondrion (mit), microtubule (MT), actin bundle (AB), multivesicular body (MVB). (A) Axonal varicosity containing interconnected vesicles (B-D, white arrowheads), vesicles connected to actin (E, F, black arrowheads). (G) Interconnected vesicles (white arrowheads) connected to a microtubule (black arrowhead) in an organotypic slice. Scale bars: (A) 200 nm, (B-G) 50 nm.

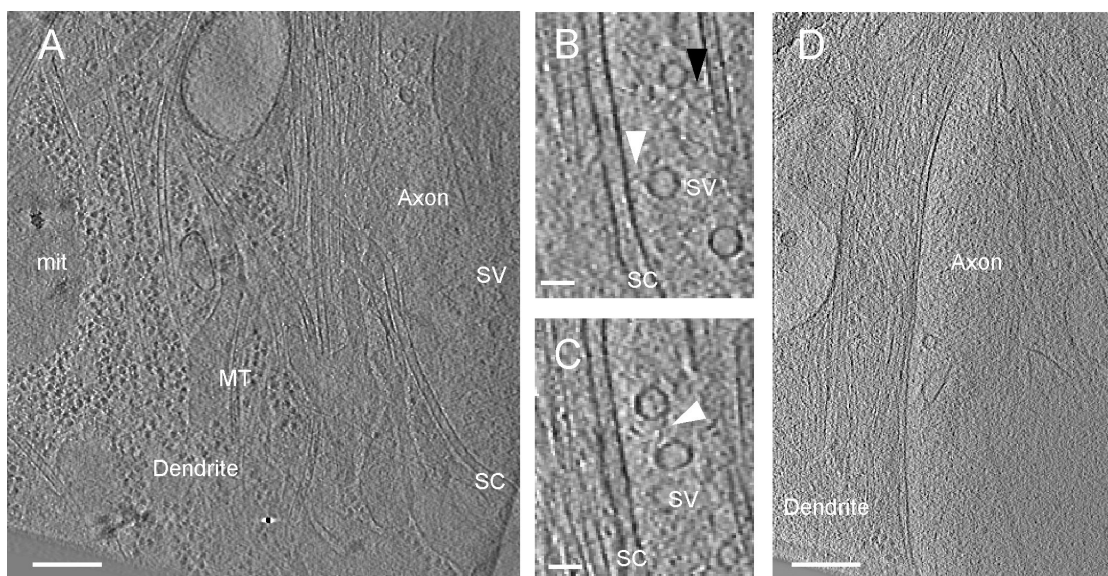


Figure 38 Putative nascent synapse in 6 DIV neuronal cultures. In all panels tomographic slices are 3.3 nm-thick. Synaptic vesicle (SV), mitochondrion (mit), microtubule (MT), synaptic cleft (SC). (A) Overview of the putative synaptic contact, showing numerous ribosome-like particles on the dendrite, separated of the axon by a regular synaptic cleft. (B, C) Vesicles in the presynaptic terminal. Weak densities act as connectors and tethers (white arrowheads) or link the vesicles to the cytoskeleton (black arrowhead). (D) Same axon and dendrite at $\sim 10 \mu\text{m}$ distance. Scale bars: (A, D) 200 nm, (B, C) 50 nm.

6 Discussion

6. Discussion

6.1 Morphology of frozen-hydrated neuronal preparations

The three most widely used models for synaptic transmission *in vitro*, namely cortical synaptosomes, hippocampal organotypic hippocampal slices and primary cultures of hippocampal neurons, were studied by cryo-ET. In all cases, artifacts arising from chemical fixation, dehydration and staining were avoided by means of sample vitrification.

Synapses were found in sufficient number in both synaptosome and hippocampal slice preparations, where synaptic ultrastructure could be observed in great detail. The individual components of the protein density of the synaptic cleft, as well as the fine structure of the postsynaptic density were imaged. However, this work focused on the analysis of presynaptic terminals, particularly on the interaction of synaptic vesicles with the presynaptic cytomatrix. Connectors and tethers were found to be the most abundant components of this cytomatrix, and longer filaments were scarce.

The analysis of vesicle distribution and connectivity for untreated synaptosomes, HTS-treated synaptosomes (under conditions corresponding to the increased osmolarity necessary for slice vitrification) and organotypic slices gave very similar results (e.g., Figure 19A, Figure 20A, B). When an effect of hypertonicity was detected, such as a reduced number of tethers, it was comparable in HTS-treated synaptosomes and organotypic slices (Figure 25). Furthermore, synaptosomes showed functional neurotransmitter release in glutamate release assays (Figure 12). Thus, these data strongly suggests that cryo-preserved synaptosomes complemented by cryosections of organotypic brain slices form a suitable experimental system for investigating both presynaptic architecture and vesicle release.

In primary cultures of hippocampal neurons at 10-15 DIV neurites form thick overlapping tangles that make synapses not easily accessible for cryo-ET investigation (Vladan Lučić, personal communication). In the younger cultures studied here, neurite outgrowth is limited and larger portions of the EM grid can be imaged. However, most synapses are not fully mature at this stage (Ahmari and Smith, 2002). In neurons cultured for 6-7 DIV, numerous axonal varicosities were observed containing abundant synaptic vesicles embedded in a dense cytoskeletal network (Figure 37). These structures could either correspond to immature presynaptic terminals or to packages of synaptic components being transported to synapses (Ahmari et al., 2000). Interestingly, a putative nascent synapse was also imaged (Figure 38). The pre- and postsynaptic terminals were separated by a ~25 nm gap (the width of the synaptic cleft in mature synapses). On the presynaptic side, synaptic vesicles accumulated close to the cellular membrane, whereas a very high number of electron dense particles, reminiscent of ribosomes, was observed on the postsynaptic side. The abundance of ribosomes in developing synapses is well established, as translation needs are specially high during the formation of the PSD (Palacios-Prü et al., 1988; Steward and Falk, 1986). These observations confirm the potential of cryo-ET for the study of not only mature, but also nascent synaptic structures.

6.2 Automated segmentation and analysis of presynaptic ultrastructure

The interpretation of EM data often relies on qualitative descriptions of the observed features. Cryo-ET provides optimal sample preservation combined with three-dimensional imaging, but in order to realize its full potential cryo-ET datasets need to be analyzed in a quantitative manner, as only rigorous statistical analysis can point out significant differences between groups of samples. For this work, a procedure for automated segmentation and data analysis was developed, allowing a comprehensive and quantitative description of the most prominent presynaptic features. By means of pharmacological treatments, relevant differences between synapses in different functional states were described.

Approaches based merely on the voxel grey scale values could not be applied directly to the segmentation of connectors and tethers because of the low SNR of cryo-tomograms and because structures bound to membranes would be segmented out together with the membranes themselves. Thus, a segmentation mask was created containing the membranous components of interest, i.e. synaptic vesicle membranes and AZ. Connectors and tethers were then detected as groups of neighboring voxels bridging two membranes and with intensities below a given threshold. Finally, a hierarchical classification selected the optimal threshold for each segment based on the local background level.

This approach offers similarities with the so-called *watershed transformation* (Soille, 2003). The watershed transformation considers a grey-scale image as a topographic surface, where darker regions represent points of higher altitude. Then, the surface is *flooded* from its minima, and dams that prevent the merging of different water basins are erected. Thus, the image is partitioned into *catchment basins* (flooded areas) and *watershed lines* (dams separating different basins, Figure 39)¹⁴. When directly applied to grey-scale images, watershed transformation often results in over-segmentation, as a high number of small basins are created around local minima. A major improvement can be obtained using the *marker-controlled* watershed transformation, in which the minima of interest are defined by the user. In the segmentation algorithm presented here, the minima of interest are preselected by the use of the segmentation mask and the connectivity condition, which restrict the possible watershed lines (connectors/tethers) only to those actually connecting two boundaries of the mask¹⁵. Then, the dataset is *flooded* (analyzed in a range of thresholds), and watershed lines at different *water levels* (thresholds) are selected as the basins fill up.

The validity of this segmentation procedure was confirmed by (i) the good correspondence between the structures observed in tomograms by visual inspection with those segmented automatically (Figure 18) and (ii) the fact that the distance between vesicles (in the case of connectors) or vesicles and AZ (tethers) was not determinant for the detection of either kind of filaments, as shown by the pharmacological effects on the abundance, distribution and morphology of connectors

¹⁴ The water level in each basin is the maximum possible before basins merge, implying that the water level can be different in different basins. Watershed lines can also be understood as the set of points where a drop falling there could flow towards several catchment basins.

¹⁵ Tomograms were denoised prior to segmentation (see 4.2), thereby also removing irrelevant minima.

(Figure 20B, E) and tethers (Figure 25A, C) that cannot be explained simply by changes in vesicle distribution (Figure 19C).

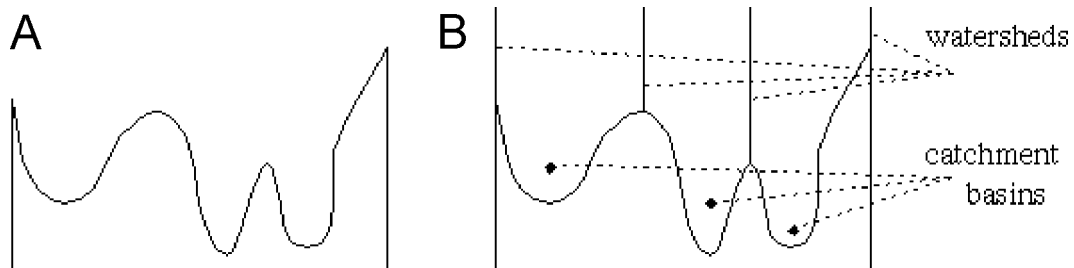


Figure 39 1D watershed segmentation. (A) Grey level profile of the data. (B) Watershed segmentation: catchment basins and watershed lines are formed in local minima and local maxima of grey level (altitude) respectively (<http://www.icaen.uiowa.edu/~dip/LECTURE/Segmentation3.html>).

On the other hand, due to the limited tilt range and high level of noise inherent to cryoelectron tomograms (Lučić et al., 2005a), it is possible that the numbers of connectors and tethers may have been underestimated by the segmentation procedure. Also, a bias towards shorter filaments was introduced during the hierarchical classification step, because only segments contacting exactly two membranes were analyzed. However, given the small number of longer filaments detected visually, it is not likely that this issue constituted a significant limitation.

6.3 The role of synaptic vesicle connectors in vesicle mobilization

Previous EM studies observed abundant filaments of different length in presynaptic terminals at rest, suggesting an important role of these structures in synaptic function. It was proposed that in resting synapses vesicles were linked to each other and/or to the cytoskeleton via short strands, which would be released upon synaptic activity to allow vesicle mobilization (Rizzoli and Betz, 2005). However, no experimental evidence for such proposal was presented so far, and the molecular identity of such strands remains uncertain. Whereas early studies identified these short filaments with synapsin (Hirokawa et al., 1989), recent work showed that some of them persisted in synapsin triple knock-out mice, indicating that other molecules must also be implicated in their formation (Siksou et al., 2007).

The analysis presented here showed that in resting synapses short (< 40 nm) connectors linked over 80% of vesicles to their neighbors, forming interconnected vesicle clusters of various size, ranging from few to more than 50 vesicles (Figure 20A, Figure 22A). Synaptic stimulation with KCl resulted in an overall reduction in synaptic vesicle concentration and connectivity and a major disruption of vesicle clusters in terms of size, connector redundancy and shape. A similar effect was observed under OA treatment, arguing that the removal of connectors is a

morphological correlate of the OA-induced dispersion of vesicles (Betz and Henkel, 1994) and increase in vesicle mobility (Kraszewski et al., 1996). Considering the absence of any other major structural elements in vitrified frozen-hydrated presynaptic terminals, these conclusions follow: i) synaptic vesicle clustering is mainly mediated by short connectors that link vesicles to each other rather than to a cytoskeletal matrix and that ii) the connectors are dynamic structures, and treatments known to increase vesicle mobility, such as KCl stimulation or OA-mediated elevation in phosphorylation levels, cause the removal of the connectors. In fact, the dynamic binding and unbinding of vesicles to each other via connectors may provide a mechanistic basis for the 'stick and diffuse' model (Shtrahman et al., 2005). Therefore, these data suggests that the connectors play a dual role, limiting vesicle dispersion in resting synapses and regulating vesicle mobilization for neurotransmitter release during synaptic activity.

The results of this study (Figure 20E, Figure 21B) suggest that there is more than one molecular species of connectors and indicate that OA has a differential effect on them. Alternatively, these data could be explained by multiple OA-dependent conformational states of one connector type, regulated by differentially localized factors. In any case, the decrease in the connectivity of proximal (but not distal) vesicles under TeTx (Figure 20B) implicates synaptobrevin in the formation of connectors in the proximal zone.

This work also provides an explanation for the observed transition of the OA effect on neurotransmitter release from facilitatory to inhibitory as a function of incubation time (Koss et al., 2007). After 15 min incubation with 1 μ M OA, actin bundles growing parallel to the AZ were visually identified (Figure 17B). Whereas OA might initially facilitate neurotransmitter release by partial removal of vesicle connectors, after longer incubation actin bundles growing parallel to the AZ would hinder mobilization of distant vesicles towards the AZ, resulting in net inhibition of release.

Differences in diameter between connected and non-connected vesicles were only minor for all treatments except OA, where connected vesicles were larger, suggesting that a target of OA is involved in the regulation of vesicle size

Lastly, the fact that vesicles were also interconnected in axonal varicosities shows that vesicle connectivity is a general mechanism for vesicle clustering, not restricted to mature synaptic contacts. This is consistent with previous reports indicating that groups of synaptic vesicles travelling along axons in young neuronal cultures were dissociated by OA (Kraszewski et al., 1995).

6.4 Active zone organization, tethering and synaptic vesicle progression towards fusion

At the ultrastructural level, the exact organization of the AZ remains controversial due to the disparity of results obtained using different EM sample preparation procedures. Thus, in chemically fixed, heavy-metal stained samples, docked vesicles were reported to accumulate around regularly arranged pyramidal densities (Phillips et al., 2001). In studies using high-pressure freezing followed by freeze-substitution and

staining, docked vesicles also clustered around electron-dense material on the AZ, but such structures did not form any regular pattern (Siksou et al., 2007). Numerous filaments but not focal densities were observed at the AZ in cryo-fixed, unstained, freeze-fractured samples (Landis et al., 1988). More recently, AZ filaments were also observed using freeze-substitution (Siksou et al., 2009b). The tomograms of vitrified, frozen-hydrated synapses studied here revealed that even though the AZ was rich in small densities, these densities were not arranged regularly and they did not cluster vesicles in their proximities (Figure 26).

Different studies present as well conflicting views on the way that vesicles proximal to the AZ associate, or *dock* to it. When chemical fixation and staining were used, docked vesicles were often reported to make direct membrane contact with the AZ, or even be hemifused with it (Zampighi et al., 2006). However, these results need to be interpreted carefully. In first place, fixatives introduce cross-linking artifacts and may alter the distribution of vesicles within the presynaptic terminal (Siksou et al., 2009a). Also, the biological structures are not observed directly but surrounded by a layer of stain of a certain thickness.

Thus, even though synaptic vesicle tethering to the AZ has been postulated to be a necessary step prior to docking, priming and fusion (Gerber et al., 2008; Verhage and Sørensen, 2008), the tethering and docking machinery have been elusive to EM methods based on chemical fixation (Schweizer and Ryan, 2006; Verhage and Sørensen, 2008). In cryo-fixed, dehydrated samples, direct membrane contact between vesicles and AZ (but not hemifusion) was reported, as well as tethering filaments of variable length (Siksou et al., 2007; Siksou et al., 2009b). In the tomograms of unstained, fully hydrated specimens of this study, membrane contact occurred only during vesicle fusion or fission. Most of the proximal vesicles of untreated synapses were tethered to the AZ by filaments shorter than 40 nm. Therefore, these results strongly suggest that the tethers described here are the main mechanism of synaptic vesicle association to the AZ and argue against hemifusion as a stable intermediate.

The RRP is functionally well characterized, but its morphological definition is still debated (Rosenmund and Stevens, 1996; Schweizer and Ryan, 2006; Verhage and Sørensen, 2008). In synaptosomes, incubation with 100 mM HTS for 60 s is known to cause the complete and exclusive release of the RRP (Ashton and Ushkaryov, 2005). The results of this work showed that synaptosomes under this hypertonic solution were distinguished from untreated ones by a reduced number of vesicles with more than two short (< 5 nm) tethers, indicating that such vesicles constitute in fact the RRP (Figure 25B, Figure 21C). Therefore, these results suggest that both the number and nature of the tethers are indicative of synaptic vesicle progression towards fusion.

Different types of tethers were present, as indicated by their wide range of lengths (Figure 21D). Furthermore, the quantitative analysis of mean number of tethers per vesicle and mean tether length (Figure 25B, C) yielded remarkably similar values for TeTx- and HTS-treated synaptosomes. Whereas longer tethers (> 5 nm) remained unaffected, short tethers were significantly reduced by TeTx action compared to the untreated case. This strongly suggests that TeTx prevents formation of the short tethers, most probably by synaptobrevin cleavage and subsequent abolishment of SNARE complex assembly. These results cannot clarify whether the fully assembled

SNARE complex constitutes the short tethers, but this hypothesis would be consistent with the notion that (primed) synaptic vesicles are located within 3-4 nm from the AZ upon SNARE complex formation (Martens and McMahon, 2008).

These results also support the lack of SNARE complex involvement in the formation of the longer tethers, as reported for other tethering systems (Sztul and Lupashin, 2006). In fact, SNARE-independent tethers of similar shape bind cargo vesicles to the endoplasmic reticulum (Tripathi et al., 2009), whereas tethering in mammalian synapses has been proposed to be mediated by the tripartite complex formed by Munc-13, RIM and Rab-3 (Dulubova, 2005; Wojcik and Brose, 2007). Nevertheless, the dimensions of the longer tethers suggest that they could mediate the stabilization of vesicles ~20 nm away from the cell membrane described in TIRF studies (Karatekin et al., 2008; Zenisek et al., 2000), necessary for SNARE complex assembly (Parpura and Mohideen, 2008). Finally, the drastic reduction of tethering observed during prolonged KCl stimulation could be a consequence of the recently proposed AZ disruption following exocytosis (Hosoi et al., 2009; Wu et al., 2009).

The observations reported here suggest the following structural model of synaptic vesicle exocytosis: (1) Initially, long, SNARE-independent filaments tether the vesicles to the AZ. (2) Long tethers give way to multiple shorter ones in an SNARE-dependent transition that makes the vesicle available for immediate release. (3) Upon establishment of membrane-to-membrane contact, exocytosis takes place. A similar model was recently proposed for the ER-to-Golgi vesicle traffic, in which transport vesicles are first tethered to the Golgi membrane by long SNARE-independent factors, and then brought into ~50 Å distance from the membrane to allow SNARE assembly and subsequent fusion (Kim et al., 2006).

In untreated synapses, proximal synaptic vesicles were larger than distal ones (Figure 27C). Furthermore, in the proximal zone tethered and/or connected vesicles were larger than non-tethered, non-connected vesicles (Figure 27D). Considering the involvement of tethering in vesicle release, one may speculate that the increase in size is correlated with vesicle progression towards exocytosis. Alternatively, different molecular compositions may determine vesicle size (Wojcik et al., 2004) as well as the exact sequence of steps leading to release (Verhage and Sørensen, 2008).

Six cases of direct membrane contact between a vesicle and the AZ were imaged (Figure 28A, B). The increased frequency of these events in synaptosomes incubated with HSV-1 could be due an elevation of cytoplasmic Ca^{2+} concentration upon interaction of the virus with the cellular membrane (Zhou et al., 2009). Since the association of the virus with the presynaptic membrane can take place at any point over an extended incubation period, it may be easier to detect exo/endocytic events upon freezing than 1 min after KCl stimulation. In two cases, a well defined, cylindrical neck was observed establishing continuity between the vesicular lumen and the extracellular space. These vesicles were located at the AZ and not coated, making it unlikely that they represent clathrin-mediated endocytosis. They may instead correspond to fusion events or, alternatively, to clathrin-independent endocytosis (such as in kiss-and-run mechanism), as suggested by their elongated necks. The direct membrane contact between vesicles and AZ was strongly correlated with the appearance of L-shaped densities consisting of two arms, one contacting the vesicle and the other one the cell membrane, reminiscent to those observed by

(Zampighi et al., 2006). Due to their large size, it is unlikely that they correspond to assembled SNARE complexes.

Each of the vesicles observed with an open pore was connected to a neighbor, indicating that the connectors may play an active role during exo/endocytosis. In fact, this observation could reveal an interplay between connectors and tethers. For example, it is believed that some unidentified mechanism exists to allow kiss-and-run by preventing full collapse fusion (Murthy and De Camilli, 2003). One could speculate that connectors play such role, acting as regulators of vesicle fusion. Thus, connected vesicles that remain linked to their neighbors would fuse by kiss-and-run as they could not undergo full collapse, whereas the removal of the connectors could favor this fusion mode. Alternatively, it is also possible to envision that when a connected vesicle fuses it may drag the next vesicle to the AZ by the action of the connector that links them. If so, the connector between two vesicles would become a (long) tether for the second one after the first one fused and connectors and long tethers would be formed by the same molecule(s).

6.5 Synaptic vesicle distribution in resting synapses is not homogeneous

Synaptic vesicle distribution in untreated terminals was characterized by similar vesicle concentrations in the proximal and distal zones, with a reduction in the intermediate region (45 to 75 nm away from the AZ, Figure 19C). A comparable distribution was observed in HTS-treated synaptosomes and individual synapses in organotypic slices. Nevertheless, this effect was averaged out in organotypic slices due to sectioning artifacts. KCl application resulted in a significant loss of vesicles in the whole terminal, more pronounced close to the AZ, as observed in other synaptic preparations (Janka and Jones, 1982).

Synaptic stimulation by OA or KCl resulted as well in a strongly significant decrease of vesicle size. Arguably, strong stimulation can deplete cytoplasmic glutamate, leading to the decrease in the amount of glutamate in vesicles (Edwards, 2007) and consequently to a smaller vesicle size (Atwood and Karunanithi, 2002). Vesicle size was also reduced by TeTx-treatment, which could impair endocytosis and vesicle maturation by synaptobrevin cleavage (Hosoi et al., 2009).

The very low abundance of presynaptic cytoskeletal elements may seem hard to reconcile with current views on the role of actin in presynaptic terminals, as well as with the non-uniform vesicle distribution reported here. However, because monomeric actin, transient or very short actin filaments that do not interlink vesicles could not be detected by the segmentation procedure, these results do not preclude the involvement of actin in processes such as scaffolding of regulatory molecules (Sankaranarayanan et al., 2003) or vesicle endocytosis (Bourne et al., 2006). Only treatment of synaptosomes with OA or the actin-stabilizing drug phalloidin resulted in substantial polymerization of long actin filaments, consistent with the reported presence of high amounts of actin in presynaptic terminals (Cingolani and Goda, 2008). In the case of phalloidin, this effect was only observed occasionally, likely due to the limited access to the cells of this membrane impermeable drug, added during

the homogenization step. The lack of such filaments in synaptosomal samples could be attributed to disruptions during the extraction procedure, but this is unlikely as they were also absent in organotypic slices, prepared by completely different methods. In fact, F-actin is known to play a limited role in adult presynaptic terminals (Zhang and Benson, 2001).

It was shown here that a great majority of vesicles in the whole terminal are connected to each other, whereas in the proximal zone they are both interconnected and tethered to the AZ. Thus, the lower vesicle concentration in the intermediate zone could be generated by the opposing dynamics of the AZ, attracting vesicles to the proximal zone via the tethering mechanism, and the large clusters of interconnected vesicles dominating the distal zones. Furthermore, the mobilization of distal vesicles towards the AZ could be mediated by the interplay between tethering and connectivity, as evidenced by clusters that reached from tethered vesicles to the distal zones, complemented with the free diffusion of non-connected vesicles (or those forming smaller clusters) through the intermediate zone.

Endocytosis takes place in the peripheral area surrounding the AZ (Heuser and Reese, 1973; Ringstad et al., 1999). Therefore, it is conceivable to think that newly endocytosed vesicles arrive to the intermediate zone, where they can be redirected to the AZ for a new round of exocytosis or join the distal clusters. Should there be a link between vesicle size and maturation, the fact that vesicle size is not reduced only at the intermediate zone in KCl-treated synaptosomes would support that hypothesis.

7 Outlook

7. Outlook

Several strategies could be envisioned in order to gain deeper understanding on the structural mechanisms that underlie neurotransmitter release. In particular, the combined use of advanced image processing techniques and new pharmacological approaches could reveal hints on the molecular identity of connectors and tethers.

Currently, subtomogram averaging is gaining momentum as a way to push tomographic resolution towards, or even below 20 Å. At this resolution fine structural detail can be appreciated and crystal structures of known proteins can be docked reliably (Briggs et al., 2009; Förster et al., 2005; Liu et al., 2008). Therefore, if connectors and tethers are sufficiently homogenous at the structural level, high resolution 3D averages could be obtained using these procedures. As an additional advantage in this case, the initial particle picking step has already been performed by the automated segmentation algorithm. From the microscopy point of view, double tilt tomography (Penczek et al., 1995), CTF correction (Fernandez et al., 2006; Xiong et al., 2009), as well as future advances in instrumentation (use of direct electron detectors, phase plates or aberration correctors) could also contribute to improve data quality.

The incubation of synaptosomes with the broad spectrum phosphatase inhibitor OA revealed that vesicle connectivity is, at least in part, regulated by phosphorylation. In order to pin down the molecules involved in this process, the use of more specific phosphatase inhibitors could be instrumental (Oliver and Shenolikar, 1998). On the other hand, protein kinases are also interesting targets for pharmacological manipulations. For example, the kinase inhibitor staurosporine prevents recruitment of vesicles from the reserve pool (Becherer et al., 2001) and vesicle clustering (Li and Murthy, 2001). CaMKII is implicated in phosphorylation of synapsin (Kennedy et al., 1983a), mediates vesicle mobilization (Levitan, 2008) and its inhibition leads to severe impairment of presynaptic function (Ninan and Arancio, 2004). Phosphorylation also plays a crucial role in synaptic vesicle association with the AZ. Thus, phorbol esters are known to increase the size of the RRP by means of PKC activation (Lou et al., 2008; Waters and Smith, 2000). The increase in vesicle docking induced by BDNF (brain-derived neurotrophic factor) is also likely to be mediated by phosphorylation processes (Tyler and Pozzo-Miller, 2001).

The most dramatic effects on vesicle docking and fusion have so far been observed with the use of clostridial neurotoxins, such as tetanus (TeTx) or botulinum (BoTx) toxins, which cleave the components of the SNARE complex blocking neurotransmitter release (Schiavo et al., 2000). SNARE complex assembly begins at the N-terminal region, progresses towards the C-terminus (i.e. towards the transmembrane domains) and is only completed upon Ca^{2+} influx (Giraudo et al., 2009; Sutton et al., 1998). The binding and cleavage sites of the clostridial neurotoxins are progressively hidden as the complex assembles (Figure 40). Thus, synaptobrevin can only be cleaved by TeTx when freely exposed, but it can still be attacked by BoTx-B while forming the pre-fusion, not fully assembled SNARE complex (Hua and Charlton, 1999).

Our results from TeTx-treated synaptosomes suggested, but could not confirm, that the short tethers were formed in fact by SNARE complexes. This is a crucial issue for the clarification of the ambiguous concept of vesicle *docking* to the AZ (Verhage and Sørensen, 2008; Wojcik and Brose, 2007) and for the understanding of the sequence of events that underlie synaptic vesicle fusion. A possible way to address it would be the treatment of synaptosomes with BoTx-B or TeTx under stimulation (in order to increase the amount of exposed synaptobrevin), which should translate into an even more significant reduction of the short tethers than with TeTx alone. These treatments could also shed light into the involvement of synaptobrevin in the formation of connectors in the proximal zone indicated by our results. Finally, it could also be interesting to use toxins that cleave the other components of the SNARE complex, such as BoTx-A (SNAP-25) or BoTx-C (syntaxin).

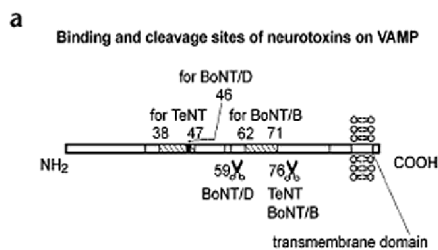


Figure 40 Cleavage and binding sites of clostridial neurotoxins on synaptobrevin (Hua and Charlton, 1999)

A genetic approach could in principle contribute as well to the identification of the molecules that form connectors and tethers. However, deletion of the genes of AZ proteins often results in non-viable animals that die at birth, complicating sample preparation (Augustin et al., 1999; Geppert et al., 1994; Schoch et al., 2001; Verhage et al., 2000; Washbourne et al., 2002). Furthermore, the high degree of redundancy of the system (Martens and McMahon, 2008; Wojcik and Brose, 2007) makes result interpretation difficult. Nevertheless, the manipulation of the expression levels of AZ proteins (Toonen et al., 2006a; Toonen et al., 2006b) and a handful of viable knockouts, such as those of RIM-1 α (Schoch et al., 2002) or synapsin (Gitler et al., 2004) offer interesting possibilities.

Actin is abundant in mature synapses, but its exact role remains unknown (Murthy and De Camilli, 2003). Our tomograms revealed that F-actin is scarce in presynaptic terminals, pointing to a more transient function. The incubation of synaptosomes with actin stabilizing (e.g., jasplakinolide) and destabilizing (e.g., cytochalasin) agents over different time periods could help to clarify this issue.

Finally, from the sample preparation point of view, further efforts towards consistent localization of synapses in primary cultures of hippocampal neurons would be desirable, as this system provides a great variety of options. These include genetic manipulation, the correlation of cryo-ET data with functional light microscopy studies (Lučić et al., 2007), or with electrophysiological recordings.

Abbreviations

1D	One-dimensional
2D	Two-dimensional
3D	Three-dimensional
AMPA	α -amino-3-hydroxyl-5-methyl-4-isoxazole-propionate
ATP	Adenosine-5'-triphosphate
AZ	Active zone
BDNF	Brain-derived neurotrophic factor
BoTx	Botulinum toxin
CaMKII	Calcium/calmodulin-dependent protein kinase II
CCD	Charged-coupled device
CTF	Contrast transfer function
DIV	Days <i>in vitro</i>
EM	Electron microscopy
ER	Endoplasmic reticulum
ET	Electron tomography
FEG	Field emission gun
HB	Homogenization buffer
HBM	Hepes-buffered medium
HPF	High-pressure freezing
HTS	Hypertonic sucrose
HSV-1	Herpes simplex virus 1
K-W test	Kruskal-Wallis test
NAD	Non-linear anisotropic diffusion
OA	Okadaic acid
PKC	Protein kinase C
PSD	Postsynaptic density
RIM	Rab3-interacting molecule
RRP	Readily releasable pool
SIRT	Simultaneous iterative reconstruction technique
SNARE	Soluble N-ethylmaleimide-sensitive factor attachment protein (SNAP) receptor
SNR	Signal-to-noise ratio
TEM	Transmission electron microscopy
TeTx	Tetanus toxin
TIRF	Total internal reflection fluorescence
VAMP	Vesicle-associated membrane protein
VGLUT	Vesicular glutamate transporter
WBP	Weighted back-projection

Acknowledgments

At this point I would like to thank the people that, in one way or another, made this work possible.

Prof. Wolfgang Baumeister for giving me the opportunity to join the Department of Molecular Structural Biology and his guidance and support throughout my time here.

Vladan Lučić for his every day patience, support, help and inspiration.

Günter Pfeiffer and Jürgen Plitzko for keeping the microscopes running and being always ready to help when the beam was not behaving.

Inga Wolf, Christoph Best and William Delnet for their help with the computer affairs.

Sabina Von Polenz and Birgit Book for making my life much easier.

The whole department, specially the “extended virus group”, for the excellent atmosphere and making these four years unforgettable in and outside the lab.

María del Carmen Godino y José Sánchez-Prieto por su ayuda para preparar los mejores sinaptosomas del mundo.

Benoît Zuber for his excellent cryosectioning work that proved invaluable for this study, and always enriching discussions.

Jacques Dubochet and Marek Cyrklaff for making possible the collaboration between Martinsried and Lausanne and for insightful discussions.

Por supuesto, a toda mi familia y en especial a mis padres, por seguir estando cerca en la distancia y apoyarme siempre: os lo debo todo a vosotros.

References

- Ahmari, S.E., Buchanan, J., and Smith, S.J. (2000). *Assembly of presynaptic active zones from cytoplasmic transport packets*. *Nat Neurosci* 3, 445.
- Ahmari, S.E., and Smith, S.J. (2002). *Knowing a nascent synapse when you see it*. *Neuron* 34, 333.
- Al-Amoudi, A., Norlen, L.P.O., and Dubochet, J. (2004). *Cryo-electron microscopy of vitreous sections of native biological cells and tissues*. *J Struct Biol* 148, 131.
- Al-Amoudi, A., Studer, D., and Dubochet, J. (2005). *Cutting artifacts and cutting process in vitreous sections for cryo-electron microscopy*. *J Struct Biol* 150, 109.
- Ashton, A.C., and Dolly, J.O. (2000). *A late phase of exocytosis from synaptosomes induced by elevated $[Ca^{2+}]_i$ is not blocked by clostridial neurotoxins*. *J Neurochem* 74, 1979-1988.
- Ashton, A.C., and Ushkaryov, Y.A. (2005). *Properties of synaptic vesicle pools in mature central nerve terminals*. *J Biol Chem* 280, 37278-37288.
- Atwood, H.L., and Karunanithi, S. (2002). *Diversification of synaptic strength: presynaptic elements*. *Nat Rev Neurosci* 3, 497.
- Augustin, I., Rosenmund, C., Sudhof, T.C., and Brose, N. (1999). *Munc13-1 is essential for fusion competence of glutamatergic synaptic vesicles*. *Nature* 400, 457-461.
- Baker, T.S., and Henderson, R. (2010). *Electron cryomicroscopy of biological macromolecules*. *International Tables of Crystallography*.
- Bartlett, W.P., and Banker, G.A. (1984). *An electron microscopic study of the development of axons and dendrites by hippocampal neurons in culture. I. Cells which develop without intercellular contacts*. *J Neurosci* 4, 1944-1953.
- Batson, P.E., Dellby, N., and Krivanek, O.L. (2002). *Sub-angstrom resolution using aberration corrected electron optics*. *Nature* 418, 617-620.
- Becherer, U., Guatimosim, C., and Betz, W.J. (2001). *Effects of staurosporine on exocytosis and endocytosis at frog motor nerve terminals*. *J Neurosci* 21, 782-787.
- Betz, W.J., and Henkel, A.W. (1994). *Okadaic acid disrupts clusters of synaptic vesicles in frog motor nerve terminals*. *J Cell Biol* 124, 843-854.
- Bourne, J., Morgan, J.R., and Pieribone, V.A. (2006). *Actin polymerization regulates clathrin coat maturation during early stages of synaptic vesicle recycling at lamprey synapses*. *J Comp Neurol* 497, 600-609.
- Brandt, S. (2005). *Markerless alignment in electron tomography*. In *Electron tomography*, J. Frank, ed. (Springer), pp. 187-216.
- Briggs, J.A.G., Riches, J.D., Glass, B., Bartonova, V., Zanetti, G., and Kräusslich, H.-G. (2009). *Structure and assembly of immature HIV*. *Proceedings of the National Academy of Sciences* 106, 11090-11095.
- Cardone, G., Grünewald, K., and Steven, A.C. (2005). *A resolution criterion for electron tomography based on cross-validation*. *J Struct Biol* 151, 117-129.
- Chen, Y.A., and Scheller, R.H. (2001). *SNARE-mediated membrane fusion*. *Nat Rev Mol Cell Biol* 2, 98-106.
- Cingolani, L.A., and Goda, Y. (2008). *Actin in action: the interplay between the actin cytoskeleton and synaptic efficacy*. *Nat Rev Neurosci* 9, 344.
- Coggan, J.S., Bartol, T.M., Esquenazi, E., Stiles, J.R., Lamont, S., Martone, M.E., Berg, D.K., Ellisman, M.H., and Sejnowski, T.J. (2005). *Evidence for ectopic neurotransmission at a neuronal synapse*. *Science* 309, 446-451.

- Cohen, P., Holmes, C.F.B., and Tsukitani, Y. (1990). *Okadaic acid: a new probe for the study of cellular regulation*. Trends Biochem Sci 15, 98-102.
- Comolli, L.R., and Downing, K.H. (2005). *Dose tolerance at helium and nitrogen temperatures for whole cell electron tomography*. J Struct Biol 152, 149.
- Cooper, J.A. (1987). *Effects of cytochalasin and phalloidin on actin*. J Cell Biol 105, 1473-1478.
- Couteaux, R., and Pecot-Dechavassine, M. (1970). *Synaptic vesicles and pouches at the level of "active zones" of the neuromuscular junction*. CR Acad Sci Paris, Série D 271, 2346-2349.
- Crowther, R.A., DeRosier, D., and Klug, A. (1970). *The reconstruction of a three-dimensional structure from projections and its application to electron microscopy*. Proc Royal Soc London Series A, Mathematical and Physical Sciences 317, 319-340.
- Dawes, C. (1971). *Biological techniques in electron microscopy* (Barnes & Noble).
- De Camilli, P., Harris, S., Jr, Huttner, W., and Greengard, P. (1983). *Synapsin I (Protein I), a nerve terminal-specific phosphoprotein. II. Its specific association with synaptic vesicles demonstrated by immunocytochemistry in agarose-embedded synaptosomes*. J Cell Biol 96, 1355-1373.
- De Robertis, E.D.P., and Bennett, H.S. (1954). *A submicroscopic vesicular component of Schwann cells and nerve satellite cells*. Exp Cell Res 6, 543-545.
- Deak, F., Xu, Y., Chang, W.-P., Dulubova, I., Khvotchev, M., Liu, X., Südhof, T.C., and Rizo, J. (2009). *Munc18-1 binding to the neuronal SNARE complex controls synaptic vesicle priming*. J Cell Biol 184, 751-764.
- Del Castillo, J., and Katz, B. (1954). *Quantal components of the end-plate potential*. J Phys 124, 560-573.
- Derosier, D.J., and Klug, A. (1968). *Reconstruction of three dimensional structures from electron micrographs*. Nature 217, 130-&.
- Dierksen, K., Typke, D., Hegerl, R., and Baumeister, W. (1993). *Towards automatic electron tomography II. Implementation of autofocus and low-dose procedures*. Ultramicroscopy 49, 109-120.
- Dierksen, K., Typke, D., Hegerl, R., Koster, A.J., and Baumeister, W. (1992). *Towards automatic electron tomography*. Ultramicroscopy 40, 71-87.
- Dosemeci, A., Vinade, L., Winters, C.A., Reese, T.S., and Tao-Cheng, J.H. (2002). *Inhibition of phosphatase activity prolongs NMDA-induced modification of the postsynaptic density*. J Neurocytol 31, 605-612.
- Dubochet, J., Adrian, M., Chang, J.-J., Homo, J.-C., Lepault, J., McDowell, A.W., and Schultz, P. (1988). *Cryo-electron microscopy of vitrified specimens*. Q Rev Biophys 21, 129-228.
- Dulubova, I., Sugita, S., Hill, S., Hosaka, M., Fernandez, I., Südhof, T., and Rizo, J. (1999). *A conformational switch in syntaxin during exocytosis: role of munc18*. EMBO J 18, 4372-4382.
- Dulubova, I.L.X., Lu J, Huryeva I, Alam A, Schneggenburger R, Südhof TC, Rizo J. (2005). *A Munc13/RIM/Rab3 tripartite complex: from priming to plasticity?* EMBO J 24, 2839-2850.
- Dunkley, P.R., Heath, J.W., Harrison, S.M., Jarvie, P.E., Glenfield, P.J., and Rostas, J.A.P. (1988). *A rapid Percoll gradient procedure for isolation of synaptosomes directly from an S1 fraction: homogeneity and morphology of subcellular fractions*. Brain Res 441, 59-71.
- Dunkley, P.R., Jarvie, P.E., Heath, J.W., Kidd, G.J., and Rostas, J.A.P. (1986). *A rapid method for isolation of synaptosomes on Percoll gradients*. Brain Res 372, 115-129.

- Edwards, R.H. (2007). *The neurotransmitter cycle and quantal size*. *Neuron* 55, 835.
- Egerton, R.F., and Leapman, R.D. (1995). *Electron optics in imaging energy filters*. In *Energy-filtering transmission electron microscopy*, L. Reimer, ed. (Springer), pp. 269-290.
- Erickson, H.P., and Klug, A. (1971). *Measurement and compensation of defocusing and aberrations by Fourier processing of electron micrographs*. *Philos Transact B, Biol* 261, 105-118.
- Estable, C., Reissig, M., and De Robertis, E. (1954). *Microscopic and submicroscopic structure of the synapsis in the ventral ganglion of the acoustic nerve*. *Exp Cell Res* 6, 255-262.
- Fernandez-Chacon, R., Konigstorfer, A., Gerber, S.H., Garcia, J., Matos, M.F., Stevens, C.F., Brose, N., Rizo, J., Rosenmund, C., and Sudhof, T.C. (2001). *Synaptotagmin I functions as a calcium regulator of release probability*. *Nature* 410, 41-49.
- Fernandez, J.-J., and Li, S. (2003). *An improved algorithm for anisotropic nonlinear diffusion for denoising cryo-tomograms*. *J Struct Biol* 144, 152.
- Fernandez, J.J., Li, S., and Crowther, R.A. (2006). *CTF determination and correction in electron cryotomography*. *Ultramicroscopy* 106, 587.
- Fletcher, T., De Camilli, P., and Banker, G. (1994). *Synaptogenesis in hippocampal cultures: evidence indicating that axons and dendrites become competent to form synapses at different stages of neuronal development*. *J Neurosci* 14, 6695-6706.
- Förster, F., Medalia, O., Zauberman, N., Baumeister, W., and Fass, D. (2005). *Retrovirus envelope protein complex structure in situ studied by cryo-electron tomography*. *Proc Natl Acad Sci U S A* 102, 4729-4734.
- Frangakis, A.S., and Förster, F. (2004). *Computational exploration of structural information from cryo-electron tomograms*. *Curr Opin Struct Biol* 14, 325-331.
- Frangakis, A.S., and Hegerl, R. (2001). *Noise reduction in electron tomographic reconstructions using nonlinear anisotropic diffusion*. *J Struct Biol* 135, 239.
- Frank, J. (2006). *Three-dimensional electron microscopy of macromolecular assemblies* (Oxford University Press).
- Gaertner, T.R., Kolodziej, S.J., Wang, D., Kobayashi, R., Koomen, J.M., Stoops, J.K., and Waxham, M.N. (2004). *Comparative analyses of the three-dimensional structures and enzymatic properties of α , β , γ , and δ Isoforms of Ca^{2+} -calmodulin-dependent protein kinase II*. *J Biol Chem* 279, 12484-12494.
- Gaffield, M.A., and Betz, W.J. (2007). *Synaptic vesicle mobility in mouse motor nerve terminals with and without synapsin*. *J Neurosci* 27, 13691-13700.
- Gähwiler, B.H., Capogna, M., Debanne, D., McKinney, R.A., and Thompson, S.M. (1997). *Organotypic slice cultures: a technique has come of age*. *Trends Neurosci* 20, 471-477.
- Garvalov, B.K., Zuber, B., Bouchet-Marquis, C., Kudryashev, M., Gruska, M., Beck, M., Leis, A., Frischknecht, F., Bradke, F., Baumeister, W., et al. (2006). *Luminal particles within cellular microtubules*. *J Cell Biol* 174, 759-765.
- Geppert, M., Goda, Y., Hammer, R.E., Li, C., Rosahl, T.W., Stevens, C.F., and Südhof, T.C. (1994). *Synaptotagmin I: A major Ca^{2+} sensor for transmitter release at a central synapse*. *Cell* 79, 717-727.
- Gerber, S.H., Rah, J.-C., Min, S.-W., Liu, X., de Wit, H., Dulubova, I., Meyer, A.C., Rizo, J., Arancillo, M., Hammer, R.E., et al. (2008). *Conformational switch of syntaxin-1 controls synaptic vesicle fusion*. *Science* 321, 1507-1510.
- Gilbert, P.F.C. (1972). *An iterative method for three-dimensional reconstruction from electron micrographs*. *Proc 5th European Congress on Electron microscopy*, 602-603.

- Giraudo, C.G., Garcia-Diaz, A., Eng, W.S., Chen, Y., Hendrickson, W.A., Melia, T.J., and Rothman, J.E. (2009). *Alternative zippering as an on-off switch for SNARE-mediated fusion*. *Science* 323, 512-516.
- Gitler, D., Takagishi, Y., Feng, J., Ren, Y., Rodriguiz, R.M., Wetsel, W.C., Greengard, P., and Augustine, G.J. (2004). *Different presynaptic roles of synapsins at excitatory and inhibitory synapses*. *J Neurosci* 24, 11368-11380.
- Godino, M., Torres, M., and Sánchez-Prieto, J. (2007). *CBI receptors diminish both Ca²⁺ influx and glutamate release through two different mechanisms active in distinct populations of cerebrocortical nerve terminals*. *J Neurochem* 101, 1471-1482.
- Godino, M.d.C. (2006). *Señalización por receptores de cannabinoides en los terminales glutamatérgicos de corteza cerebral*. In Facultad de Farmacia (Madrid, Universidad Complutense de Madrid).
- Gonen, T., Cheng, Y., Sliz, P., Hiroaki, Y., Fujiyoshi, Y., Harrison, S.C., and Walz, T. (2005). *Lipid-protein interactions in double-layered two-dimensional AQP0 crystals*. *Nature* 438, 633-638.
- Goslin, K., and Banker, G. (1991). *Rat hippocampal neurons in low-density culture*. In *Culturing Nerve Cells*, G. Banker, and K. Goslin, eds. (MIT Press), pp. 251-281.
- Gotow, T., Miyaguchi, K., and Hashimoto, P.H. (1991). *Cytoplasmic architecture of the axon terminal: filamentous strands specifically associated with synaptic vesicles*. *Neuroscience* 40, 587.
- Gottmann, K. (2008). *Transsynaptic modulation of the synaptic vesicle cycle by cell-adhesion molecules*. *J Neurosci Res* 86, 223-232.
- Gray, E. (1959). *Axo-somatic and axo-dendritic synapses of the cerebral cortex: an electron microscope study*. *J Anat* 93, 420-433.
- Gray, E. (1963). *Electron microscopy of presynaptic organelles of the spinal cord*. *J Anat* 97, 101-106.
- Grimm, R., Bärmann, M., Häckl, W., Typke, D., Sackmann, E., and Baumeister, W. (1997). *Energy filtered electron tomography of ice-embedded actin and vesicles*. *Biophys J* 72, 482-489.
- Grimm, R., Koster, A.J., Ziese, U., Typke, D., and Baumeister, W. (1996). *Zero-loss energy filtering under low-dose conditions using a post-column energy filter*. *J Microsc* 183, 60-68.
- Gulyas-Kovacs, A., de Wit, H., Milosevic, I., Kochubey, O., Toonen, R., Klingauf, J., Verhage, M., and Sorensen, J.B. (2007). *Munc18-1: sequential interactions with the fusion machinery stimulate vesicle docking and priming*. *J Neurosci* 27, 8676-8686.
- Gundelfinger, E.D., Kessels, M.M., and Qualmann, B. (2003). *Temporal and spatial coordination of exocytosis and endocytosis*. *Nat Rev Mol Cell Biol* 4, 127.
- Han, H.-W., Zuber, B., and Dubochet, J. (2008). *Compression and crevasses in vitreous sections under different cutting conditions*. *J Microsc* 230, 167-171.
- Harata, A.M.A., Richard W. Tsien, (2006). *Kiss-and-run and full-collapse fusion as modes of exo-endocytosis in neurosecretion*. *J Neurochem* 97, 1546-1570.
- Harlow, M.L., Ress, D., Stoschek, A., Marshall, R.M., and McMahan, U.J. (2001). *The architecture of active zone material at the frog's neuromuscular junction*. *Nature* 409, 479.
- Harris, K.M., and Sultan, P. (1995). *Variation in the number, location and size of synaptic vesicles provides an anatomical basis for the nonuniform probability of release at hippocampal CA1 synapses*. *Neuropharmacology* 34, 1387.
- Harrison, S.M., Jarvie, P.E., and Dunkley, P.R. (1988). *A rapid Percoll gradient procedure for isolation of synaptosomes directly from an S1 fraction: viability of subcellular fractions*. *Brain Res* 441, 72-80.

- Hart, R.C. (1968). *Electron microscopy of unstained biological material: The polytropic montage*. *Science* 159, 1664-1667.
- Hawkes, P. (2005). *The electron microscope as a structure projector*. In *Electron Tomography*, J. Frank, ed. (Springer), pp. 83-112.
- Hegerl, R., and Hoppe, W. (1976). *Influence of electron noise on 3-dimensional image reconstruction*. *Zeitschrift Fur Naturforschung A - J Phys Sci* 31, 1717-1721.
- Heide, H.G., and Zeitler, E. (1985). *The physical behavior of solid water at low temperatures and the embedding of electron microscopical specimens*. *Ultramicroscopy* 16, 151-160.
- Henderson, R. (1995). *The potential and limitations of neutrons, electrons and X-rays for atomic resolution microscopy of unstained biological molecules*. *Q Rev Biophys* 28, 171-193.
- Heuser, J.E., and Reese, T.S. (1973). *Evidence for recycling of synaptic vesicle membrane during transmitter release at the frog neuromuscular junction*. *J Cell Biol* 57, 315-344.
- Heuser, J.E., Reese, T.S., Dennis, M.J., Jan, Y., Jan, L., and Evans, L. (1979). *Synaptic vesicle exocytosis captured by quick freezing and correlated with quantal transmitter release*. *J Cell Biol* 81, 275-300.
- Hilfiker, S., Pieribone, V.A., Czernik, A.J., Kao, H.T., Augustine, G.J., and Greengard, P. (1999). *Synapsins as regulators of neurotransmitter release*. *Phil Trans R Soc Lond B* 354, 269.
- Hirokawa, N., Sobue, K., Kanda, K., Harada, A., and Yorifuji, H. (1989). *The cytoskeletal architecture of the presynaptic terminal and molecular structure of synapsin I*. *J Cell Biol* 108, 111-126.
- Holzinger, A. (2009). *Jasplakinolide: an actin-specific reagent that promotes actin polymerization*. In *Cytoskeleton methods and protocols*, pp. 71-87.
- Hoppe, W., Gassmann, J., Hunsmann, N., Schramm, H.J., and Sturm, M. (1974). *Three-dimensional reconstruction of individual negatively stained yeast fatty-acid synthetase molecules from tilt series in the electron microscope*. *Hoppe-Seylers Zeitschrift Fur Physiologische Chemie* 355, 1483-1487.
- Hosoi, N., Holt, M., and Sakaba, T. (2009). *Calcium dependence of exo- and endocytotic coupling at a glutamatergic synapse*. *Neuron* 63, 216-229.
- Hua, S.-Y., and Charlton, M.P. (1999). *Activity-dependent changes in partial VAMP complexes during neurotransmitter release*. *Nat Neurosci* 2, 1078-1083.
- Hui, E., Johnson, C.P., Yao, J., Dunning, F.M., and Chapman, E.R. (2009). *Synaptotagmin-mediated bending of the target membrane is a critical step in Ca²⁺-regulated fusion*. *Cell* 138, 709-721.
- Iancu, C.V., Wright, E.R., Heymann, J.B., and Jensen, G.J. (2006). *A comparison of liquid nitrogen and liquid helium as cryogens for electron cryotomography*. *J Struct Biol* 153, 231.
- Janka, Z., and Jones, D.G. (1982). *A morphometric study of cultured rat cerebral synapses exposed to different cationic media*. *Brain Res* 241, 215-225.
- Jovanovic, J.N., Sihra, T.S., Nairn, A.C., Hemmings, H.C., Jr., Greengard, P., and Czernik, A.J. (2001). *Opposing changes in phosphorylation of specific sites in synapsin I during Ca²⁺-dependent glutamate release in isolated nerve terminals*. *J Neurosci* 21, 7944-7953.
- Kaesler, P.S., Deng, L., Chávez, A.E., Liu, X., Castillo, P.E., and Südhof, T.C. (2009). *ELKS2 α /CAST deletion selectively increases neurotransmitter release at inhibitory synapses*. *Neuron* 64, 227-239.

- Karatekin, E., Tran, V.S., Huet, S., Fanget, I., Cribier, S., and Henry, J.-P. (2008). *A 20-nm step toward the cell membrane preceding exocytosis may correspond to docking of tethered granules*. *Biophys J* 94, 2891-2905.
- Katz, B. (1969). *The release of neuronal transmitter substances* (Liverpool Univ. Press).
- Kennedy, M., McGuinness, T., and Greengard, P. (1983a). *A calcium/calmodulin-dependent protein kinase from mammalian brain that phosphorylates Synapsin I: partial purification and characterization*. *J Neurosci* 3, 818-831.
- Kennedy, M.B., Bennett, M.K., and Erondy, N.E. (1983b). *Biochemical and immunochemical evidence that the "major postsynaptic density protein" is a subunit of a calmodulin-dependent protein kinase*. *Proc Natl Acad Sci U S A* 80, 7357-7361.
- Khvotchev, M., Dulubova, I., Sun, J., Dai, H., Rizo, J., and Sudhof, T.C. (2007). *Dual modes of Munc18-1/SNARE interactions are coupled by functionally critical binding to syntaxin-1 N terminus*. *J Neurosci* 27, 12147-12155.
- Kim, Y.-G., Raunser, S., Munger, C., Wagner, J., Song, Y.-L., Cygler, M., Walz, T., Oh, B.-H., and Sacher, M. (2006). *The architecture of the multisubunit TRAPP I complex suggests a model for vesicle tethering*. *Cell* 127, 817-830.
- Koss, D., Hindley, K., Riedel, G., and Platt, B. (2007). *Modulation of hippocampal calcium signalling and plasticity by serine/threonine protein phosphatases*. *J Neurochem* 102, 1009-1023.
- Koster, A.J., Chen, H., Sedat, J.W., and Agard, D.A. (1992). *Automated microscopy for electron tomography*. *Ultramicroscopy* 46, 207.
- Koster, A.J., de Ruijter, W.J., Van Den Bos, A., and Van Der Mast, K.D. (1989). *Autotuning of a TEM using minimum electron dose*. *Ultramicroscopy* 27, 251-272.
- Koster, A.J., Grimm, R., Typke, D., Hegerl, R., Stoschek, A., Walz, J., and Baumeister, W. (1997). *Perspectives of molecular and cellular electron tomography*. *J Struct Biol* 120, 276-308.
- Kraszewski, K., Daniell, L., Mundigl, O., and De Camilli, P. (1996). *Mobility of synaptic vesicles in nerve endings monitored by recovery from photobleaching of synaptic vesicle-associated fluorescence*. *J Neurosci* 16, 5905-5913.
- Kraszewski, K., Mundigl, O., Daniell, L., Verderio, C., Matteoli, M., and De Camilli, P. (1995). *Synaptic vesicle dynamics in living cultured hippocampal neurons visualized with CY3-conjugated antibodies directed against the luminal domain of synaptotagmin*. *J Neurosci* 15, 4328-4342.
- Kullmann, D.M., and Lamsa, K.P. (2007). *Long-term synaptic plasticity in hippocampal interneurons*. *Nat Rev Neurosci* 8, 687-699.
- Landis, D.M.D., Hall, A.K., Weinstein, L.A., and Reese, T.S. (1988). *The organization of cytoplasm at the presynaptic active zone of a central nervous system synapse*. *Neuron* 1, 201.
- Lenzi, D., Runyeon, J.W., Crum, J., Ellisman, M.H., and Roberts, W.M. (1999). *Synaptic vesicle populations in saccular hair cells reconstructed by electron tomography*. *J Neurosci* 19, 119-132.
- Levitan, E. (2008). *Signaling for vesicle mobilization and synaptic plasticity*. *Mol Neurobiol* 37, 39-43.
- Li, Z., and Murthy, V.N. (2001). *Visualizing postendocytic traffic of synaptic vesicles at hippocampal synapses*. *Neuron* 31, 593-605.
- Liu, J., Bartesaghi, A., Borgnia, M.J., Sapiro, G., and Subramaniam, S. (2008). *Molecular architecture of native HIV-1 gp120 trimers*. *Nature* 455, 109-113.

- Lonart, G., Schoch, S., Kaeser, P.S., Larkin, C.J., Südhof, T.C., and Linden, D.J. (2003). *Phosphorylation of RIM1- α by PKA triggers presynaptic long-term potentiation at cerebellar parallel fiber synapses*. *Cell* 115, 49-60.
- Lou, X., Korogod, N., Brose, N., and Schneggenburger, R. (2008). *Phorbol esters modulate spontaneous and Ca²⁺-evoked transmitter release via acting on both *munc13* and protein kinase C*. *J Neurosci* 28, 8257-8267.
- Lučić, V., Forster, F., and Baumeister, W. (2005a). *Structural studies by electron tomography: from cells to molecules*. *Annu Rev Biochem* 74, 833-865.
- Lučić, V., Kossel, A.H., Yang, T., Bonhoeffer, T., Baumeister, W., and Sartori, A. (2007). *Multiscale imaging of neurons grown in culture: From light microscopy to cryo-electron tomography*. *J Struct Biol* 160, 146.
- Lučić, V., Yang, T., Schweikert, G., Forster, F., and Baumeister, W. (2005b). *Morphological characterization of molecular complexes present in the synaptic cleft*. *Structure* 13, 423.
- Marks, B., and McMahon, H.T. (1998). *Calcium triggers calcineurin-dependent synaptic vesicle recycling in mammalian nerve terminals*. *Curr Biol* 8, 740.
- Martens, S., and McMahon, H.T. (2008). *Mechanisms of membrane fusion: disparate players and common principles*. *Nat Rev Mol Cell Biol* 9, 543-556.
- Masich, S., Ostberg, T., Norlen, L., Shupliakov, O., and Daneholt, B. (2006). *A procedure to deposit fiducial markers on vitreous cryo-sections for cellular tomography*. *J Struct Biol* 156, 461.
- Mastrorarde, D. (2005). *Fiducial marker and hybrid alignment methods for single- and double- axis tomography*. In *Electron Tomography*, J. Frank, ed. (Springer), pp. 163-186.
- Maurer, U.E., Sodeik, B., and Grünewald, K. (2008). *Native 3D intermediates of membrane fusion in herpes simplex virus 1 entry*. *Proc Natl Acad Sci U S A* 105, 10559-10564.
- McEwen, B.F., Downing, K.H., and Glaeser, R.M. (1995). *The relevance of dose-fractionation in tomography of radiation-sensitive specimens*. *Ultramicroscopy* 60, 357-373.
- McIntosh, J.R. (2001). *Electron microscopy of cells: a new beginning for a new century*. *J Cell Biol* 153, 25F-32.
- McMahon, H.T., Foran, P., Dolly, J.O., Verhage, M., Wiegant, V.M., and Nicholls, D.G. (1992). *Tetanus toxin and botulinum toxins type A and B inhibit glutamate, gamma-aminobutyric acid, aspartate, and met-enkephalin release from synaptosomes. Clues to the locus of action*. *J Biol Chem* 267, 21338-21343.
- Meberg, P.J., and Miller, M.W. (2003). *Culturing hippocampal and cortical neurons*. In *Methods in cell biology* (Academic Press), pp. 111-127.
- Medalia, O., Beck, M., Ecke, M., Weber, I., Neujahr, R., Baumeister, W., and Gerisch, G. (2007). *Organization of actin networks in intact filopodia*. *Curr Biol* 17, 79.
- Meila, M. (2007). *Comparing clusterings - An information based distance*. *J Multivar Anal* 98, 873-895.
- Midgley, P.A., and Weyland, M. (2003). *3D electron microscopy in the physical sciences: the development of Z-contrast and EFTEM tomography*. *Ultramicroscopy* 96, 413.
- Murk, J.L.A.N., Posthuma, G., Koster, A.J., Geuze, H.J., Verkleij, A.J., Kleijmeer, M.J., and Humbel, B.M. (2003). *Influence of aldehyde fixation on the morphology of endosomes and lysosomes: quantitative analysis and electron tomography*. *J Microsc* 212, 81-90.

- Murthy, V.N., and De Camilli, P. (2003). *Cell biology of the presynaptic terminal*. *Annu Rev Neurosci* 26, 701-728.
- Nagy, A., and Delgado-Escueta, A.V. (1984). *Rapid preparation of synaptosomes of mammalian brain using nontoxic isoosmotic gradient material (Percoll)*. *J Neurochem* 43, 1114-1123.
- Neher, E., and Sakaba, T. (2008). *Multiple roles of calcium ions in the regulation of neurotransmitter release*. *Neuron* 59, 861-872.
- Nicholls, D.G., and Sihra, T.S. (1986). *Synaptosomes possess an exocytotic pool of glutamate*. *Nature* 321, 772.
- Nickell, S., Förster, F., Linaroudis, A., Net, W.D., Beck, F., Hegerl, R., Baumeister, W., and Plitzko, J.M. (2005). *TOM software toolbox: acquisition and analysis for electron tomography*. *J Struct Biol* 149, 227-234.
- Ninan, I., and Arancio, O. (2004). *Presynaptic CaMKII is necessary for synaptic plasticity in cultured hippocampal neurons*. *Neuron* 42, 129-141.
- O'Keefe, M.A. (1992). *"Resolution" in high-resolution electron microscopy*. *Ultramicroscopy* 47, 282-297.
- Oliver, C.J., and Shenolikar, S. (1998). *Physiologic importance of protein phosphatase inhibitors*. *Frontiers in Bioscience* 3, D961-972.
- Ortiz, J.O., Förster, F., Kürner, J., Linaroudis, A.A., and Baumeister, W. (2006). *Mapping 70S ribosomes in intact cells by cryoelectron tomography and pattern recognition*. *J Struct Biol* 156, 334-341.
- Palacios-Prü, E., Miranda-Contreras, L., Mendoza B, R.V., and Zambrano, E. (1988). *Dendritic RNA and postsynaptic density formation in chick cerebellar synaptogenesis*. *Neuroscience* 24, 111-118.
- Palade, G., and Palay, S.L. (1954). *Electron microscope observations of interneuronal and neuromuscular synapses*. *The Anatomical Record* 118, 275-454.
- Palay, S.L. (1956). *Synapses in the central nervous system*. *J Cell Biol* 2, 193-202.
- Parpura, V., and Mohideen, U. (2008). *Molecular form follows function: (un)snaring the SNAREs*. *Trends Neurosci* 31, 435.
- Penczek, P., Marko, M., Buttle, K., and Frank, J. (1995). *Double-tilt electron tomography*. *Ultramicroscopy* 60, 393-410.
- Penczek, P.A. (2002). *Three-dimensional spectral signal-to-noise ratio for a class of reconstruction algorithms*. *J Struct Biol* 138, 34-46.
- Pfenninger, K., Sandri, C., Akert, K., and Eugster, C.H. (1969). *Contribution to the problem of structural organization of the presynaptic area*. *Brain Res* 12, 10-18.
- Phillips, G.R., Huang, J.K., Wang, Y., Tanaka, H., Shapiro, L., Zhang, W., Shan, W.-S., Arndt, K., Frank, M., and Gordon, R.E. (2001). *The presynaptic particle web: ultrastructure, composition, dissolution, and reconstitution*. *Neuron* 32, 63.
- Purves, D., Augustine, G.J., Fitzpatrick, D., Hall, W.C., LaMantia, A.-S., McNamara, J.O., and White, L.E. (2008). *Neuroscience*, Fourth edn (Sunderland, MA, USA, Sinauer Associates).
- Radon, J. (1917). *Über die Bestimmung von Funktionen durch ihre Integralwerte längs gewisser Mannigfaltigkeiten*. *Math Phys Klasse* 69, 262-277.
- Reim, K., Mansour, M., Varoquaux, F., McMahan, H.T., Südhof, T.C., Brose, N., and Rosenmund, C. (2001). *Complexins regulate a late step in Ca²⁺-dependent neurotransmitter release*. *Cell* 104, 71-81.
- Reimer, L., and Kohl, H. (2008). *Transmission electron microscopy* (Springer).
- Reimer, L., and Rossmessemer, R. (1989). *Contrast in the electron spectroscopic imaging mode of A TEM.1. Influence of zero-loss filtering on scattering contrast*. *Journal of Microscopy* 155, 169-182.

- Ringstad, N., Gad, H., Löw, P., Di Paolo, G., Brodin, L., Shupliakov, O., and De Camilli, P. (1999). *Endophilin/SH3p4 is required for the transition from early to late stages in clathrin-mediated synaptic vesicle endocytosis*. *Neuron* 24, 143-154.
- Rizzoli, S.O., and Betz, W.J. (2005). *Synaptic vesicle pools*. *Nat Rev Neurosci* 6, 57.
- Rizzoli, S.O., and Jahn, R. (2007). *Kiss-and-run, collapse and 'readily retrievable' vesicles*. *Traffic* 8, 1137-1144.
- Robertson, J. (1953). *Ultrastructure of two invertebrate synapses*. *Proc Soc Exp Biol Med* 82, 219-223.
- Rollenhagen, and Lübke (2006). *The morphology of excitatory central synapses: from structure to function*. *Cell Tissue Res* 326, 221.
- Rosenmund, C., Sigler, A., Augustin, I., Reim, K., Brose, N., and Rhee, J.-S. (2002). *Differential control of vesicle priming and short-term plasticity by Munc13 isoforms*. *Neuron* 33, 411-424.
- Rosenmund, C., and Stevens, C.F. (1996). *Definition of the readily releasable pool of vesicles at hippocampal synapses*. *Neuron* 16, 1197.
- Ruska, E. (1986). *The development of the electron microscope and of electron microscopy*. Nobel Prize Lecture.
- Sankaranarayanan, S., Atluri, P.P., and Ryan, T.A. (2003). *Actin has a molecular scaffolding, not propulsive, role in presynaptic function*. *Nat Neurosci* 6, 127.
- Sasaki-Sherrington, S., Jacobs, J., and Stevens, J. (1984). *Intracellular control of axial shape in non-uniform neurites: a serial electron microscopic analysis of organelles and microtubules in AI and AII retinal amacrine neurites*. *J Cell Biol* 98, 1279-1290.
- Schiavo, G., Matteoli, M., and Montecucco, C. (2000). *Neurotoxins affecting neuroexocytosis*. *Physiol Rev* 80, 717-766.
- Schikorski, T., and Stevens, C.F. (2001). *Morphological correlates of functionally defined synaptic vesicle populations*. *Nat Neurosci* 4, 391.
- Schoch, S., Castillo, P.E., Jo, T., Mukherjee, K., Geppert, M., Wang, Y., Schmitz, F., Malenka, R.C., and Sudhof, T.C. (2002). *RIM1 α forms a protein scaffold for regulating neurotransmitter release at the active zone*. *Nature* 415, 321-326.
- Schoch, S., Deak, F., Königstorfer, A., Mozhayeva, M., Sara, Y., Sudhof, T.C., and Kavalali, E.T. (2001). *SNARE function analyzed in synaptobrevin/VAMP knockout mice*. *Science* 294, 1117-1122.
- Schoch, S., and Gundelfinger, E. (2006). *Molecular organization of the presynaptic active zone*. *Cell Tissue Res*, 1.
- Schweikert, G. (2004). *Quantitativer Vergleich der Strahlenschädigung biologischer Proben im Transmissions-Elektronenmikroskop bei Stickstoff- und Helium-Temperatur*. In Department of Structural Molecular Biology, MPI of Biochemistry (Technische Universität München).
- Schweizer, F.E., and Ryan, T.A. (2006). *The synaptic vesicle: cycle of exocytosis and endocytosis*. *Curr Opin Neurobiol* 16, 298.
- Serysheva, I.I., Ludtke, S.J., Baker, M.R., Chiu, W., and Hamilton, S.L. (2002). *Structure of the voltage-gated L-type Ca²⁺ channel by electron cryomicroscopy*. *Proc Natl Acad Sci U S A* 99, 10370-10375.
- Sheng, M., and Hoogenraad, C.C. (2007). *The postsynaptic architecture of excitatory synapses: a more quantitative view*. *Annu Rev Biochem* 76, 823-847.
- Shtrahman, M., Yeung, C., Nauen, D.W., Bi, G.-q., and Wu, X.-l. (2005). *Probing vesicle dynamics in single hippocampal synapses*. *Biophys J* 89, 3615-3627.
- Shupliakov, O., Bloom, O., Gustafsson, J.S., Kjaerulff, O., Low, P., Tomilin, N., Pieribone, V.A., Greengard, P., and Brodin, L. (2002). *Impaired recycling of synaptic*

- vesicles after acute perturbation of the presynaptic actin cytoskeleton*. Proc Natl Acad Sci U S A 99, 14476-14481.
- Siksou, L., Rostaing, P., Lechaire, J.-P., Boudier, T., Ohtsuka, T., Fejtova, A., Kao, H.-T., Greengard, P., Gundelfinger, E.D., Triller, A., *et al.* (2007). *Three-dimensional architecture of presynaptic terminal cytomatrix*. J Neurosci 27, 6868-6877.
- Siksou, L., Triller, A., and Marty, S. (2009a). *An emerging view of presynaptic structure from electron microscopic studies*. J Neurochem 108, 1336-1342.
- Siksou, L., Varoqueaux, F., Pascual, O., Triller, A., Brose, N., and Marty, S. (2009b). *A common molecular basis for membrane docking and functional priming of synaptic vesicles*. Eur J Neurosci 30, 49-56.
- Sim, A.T.R., Lloyd, H.G.E., Jarvie, P.E., Morrison, M., Rostas, J.A.P., and Dunkley, P.R. (1993). *Synaptosomal amino acid release: effect of inhibiting protein phosphatases with okadaic acid*. Neurosci Lett 160, 181.
- Sjöstrand, F. (1953). *The ultrastructure of the retinal rod synapses of the guinea pig eye*. J Appl Phys 24.
- Smith, M.F., and Langmore, J.P. (1992). *Quantitation of molecular densities by cryo-electron microscopy : Determination of the radial density distribution of tobacco mosaic virus*. J Mol Biol 226, 763-774.
- Smith, S.M., Renden, R., and von Gersdorff, H. (2008). *Synaptic vesicle endocytosis: fast and slow modes of membrane retrieval*. Trends in Neurosciences 31, 559-568.
- Sobolevsky, A.I., Rosconi, M.P., and Gouaux, E. (2009). *X-ray structure, symmetry and mechanism of an AMPA-subtype glutamate receptor*. Nature 462, 745-756.
- Soille, P. (2003). *Morphological image analysis* (New York, Springer).
- Steward, O., and Falk, P. (1986). *Protein-synthetic machinery at postsynaptic sites during synaptogenesis: a quantitative study of the association between polyribosomes and developing synapses*. J Neurosci 6, 412-423.
- Stewart, M., and Vigers, G. (1986). *Electron microscopy of frozen-hydrated biological material*. Nature 319, 631-636.
- Stoppini, L., Buchs, P.A., and Muller, D. (1991). *A simple method for organotypic cultures of nervous tissue*. J Neurosci Methods 37, 173-182.
- Studer, D., Humbel, B., and Chiquet, M. (2008). *Electron microscopy of high pressure frozen samples: bridging the gap between cellular ultrastructure and atomic resolution*. HistochemCell Biol 130, 877-889.
- Südhof, T.C. (2004). *The synaptic vesicle cycle*. Annu Rev Neurosci 27, 509-547.
- Südhof, T.C. (2006). *Synaptic vesicles: an organelle comes of age*. Cell 127, 671.
- Südhof, T.C., and Rothman, J.E. (2009). *Membrane fusion: grappling with SNARE and SM proteins*. Science 323, 474-477.
- Sutton, R.B., Fasshauer, D., Jahn, R., and Brunger, A.T. (1998). *Crystal structure of a SNARE complex involved in synaptic exocytosis at 2.4 Å resolution*. Nature 395, 347.
- Sztul, E., and Lupashin, V. (2006). *Role of tethering factors in secretory membrane traffic*. Am J Physiol Cell Physiol 290, C11-26.
- Takamori, S., Holt, M., Stenius, K., Lemke, E.A., Grønborg, M., Riedel, D., Urlaub, H., Schenck, S., Brügger, B., Ringler, P., *et al.* (2006). *Molecular anatomy of a trafficking organelle*. Cell 127, 831.
- Takao-Rikitsu, E., Mochida, S., Inoue, E., Deguchi-Tawarada, M., Inoue, M., Ohtsuka, T., and Takai, Y. (2004). *Physical and functional interaction of the active zone proteins, CAST, RIM1, and Bassoon, in neurotransmitter release*. J Cell Biol 164, 301-311.
- Taylor, K.A., and Glaeser, R.M. (1974). *Electron diffraction of frozen, hydrated protein crystals*. Science 186, 1036-1037.

- Toonen, R., Kochubey, O., de Wit, H., Gulyas-Kovacs, A., Konijnenburg, B., Sorensen, J., Klingauf, J., and Verhage, M. (2006a). *Dissecting docking and tethering of secretory vesicles at the target membrane*. *EMBO J* 25, 3725-3737.
- Toonen, R.F.G., Wierda, K., Sons, M.S., de Wit, H., Cornelisse, L.N., Brussaard, A., Plomp, J.J., and Verhage, M. (2006b). *Munc18-1 expression levels control synapse recovery by regulating readily releasable pool size*. *Proc Natl Acad Sci U S A* 103, 18332-18337.
- Toyoshima, C., and Unwin, N. (1988). *Contrast transfer for frozen-hydrated specimens: Determination from pairs of defocused images*. *Ultramicroscopy* 25, 279-291.
- Tripathi, A., Ren, Y., Jeffrey, P.D., and Hughson, F.M. (2009). *Structural characterization of Tip20p and Dsl1p, subunits of the Dsl1p vesicle tethering complex*. *Nat Struct Mol Biol* 16, 114-123.
- Tyler, W.J., and Pozzo-Miller, L.D. (2001). *BDNF enhances quantal neurotransmitter release and increases the number of docked vesicles at the active zones of hippocampal excitatory synapses*. *J Neurosci* 21, 4249-4258.
- Unser, M., Sorzano, C.O.S., Thevenaz, P., Jonic, S., El-Bez, C., De Carlo, S., Conway, J.F., and Trus, B.L. (2005). *Spectral signal-to-noise ratio and resolution assessment of 3D reconstructions*. *J Struct Biol* 149, 243.
- Varoqueaux, F., Sigler, A., Rhee, J.-S., Brose, N., Enk, C., Reim, K., and Rosenmund, C. (2002). *Total arrest of spontaneous and evoked synaptic transmission but normal synaptogenesis in the absence of Munc13-mediated vesicle priming*. *Proc Natl Acad Sci U S A* 99, 9037-9042.
- Vaughan, R.A., Huff, R.A., Uhl, G.R., and Kuhar, M.J. (1997). *Protein kinase C-mediated phosphorylation and functional regulation of dopamine transporters in striatal synaptosomes*. *J Biol Chem* 272, 15541-15546.
- Verhage, M., Maia, A.S., Plomp, J.J., Brussaard, A.B., Heeroma, J.H., Vermeer, H., Toonen, R.F., Hammer, R.E., van den Berg, T.K., Missler, M., *et al.* (2000). *Synaptic assembly of the brain in the absence of neurotransmitter secretion*. *Science* 287, 864-869.
- Verhage, M., and Sørensen, J. (2008). *Vesicle docking in regulated exocytosis*. *Traffic* 9, 1414-1424.
- Washbourne, P., Thompson, P.M., Carta, M., Costa, E.T., Mathews, J.R., Lopez-Bendito, G., Molnar, Z., Becher, M.W., Valenzuela, C.F., Partridge, L.D., *et al.* (2002). *Genetic ablation of the t-SNARE SNAP-25 distinguishes mechanisms of neuroexocytosis*. *Nat Neurosci* 5, 19-26.
- Waters, J., and Smith, S.J. (2000). *Phorbol esters potentiate evoked and spontaneous release by different presynaptic mechanisms*. *J Neurosci* 20, 7863-7870.
- Weimer, R.M., Gracheva, E.O., Meyrignac, O., Miller, K.G., Richmond, J.E., and Bessereau, J.-L. (2006). *Unc-13 and Unc-10/Rim localize synaptic vesicles to specific membrane domains*. *J Neurosci* 26, 8040-8047.
- Whittaker, V.P. (1993). *Thirty years of synaptosome research*. *J Neurocytol* 22, 735-742.
- Williams, D., and Carter, C. (1996). *Transmission electron microscopy* (Plenum Press).
- Wojcik, S.M., and Brose, N. (2007). *Regulation of membrane fusion in synaptic excitation-secretion coupling: speed and accuracy matter*. *Neuron* 55, 11.
- Wojcik, S.M., Rhee, J.S., Herzog, E., Sigler, A., Jahn, R., Takamori, S., Brose, N., and Rosenmund, C. (2004). *An essential role for vesicular glutamate transporter 1*

- (VGLUT1) in postnatal development and control of quantal size. *Proc Natl Acad Sci U S A* 101, 7158-7163.
- Wolf, M., Eberhart, A., Glossmann, H., Striessnig, J., and Grigorieff, N. (2003). *Visualization of the domain structure of an L-type Ca²⁺ channel using electron cryo-microscopy*. *J Mol Biol* 332, 171-182.
- Wu, X.-S., McNeil, B.D., Xu, J., Fan, J., Xue, L., Melicoff, E., Adachi, R., Bai, L., and Wu, L.-G. (2009). *Ca²⁺ and calmodulin initiate all forms of endocytosis during depolarization at a nerve terminal*. *Nat Neurosci* 12, 1003-1010.
- Xiong, Q., Morpew, M.K., Schwartz, C.L., Hoenger, A.H., and Mastrorarde, D.N. (2009). *CTF determination and correction for low dose tomographic tilt series*. *Journal of Structural Biology* 168, 378-387.
- Yu, X., Jin, L., and Zhou, Z.H. (2008). *3.88 Å structure of cytoplasmic polyhedrosis virus by cryo-electron microscopy*. *Nature* 453, 415-419.
- Zampighi, G.A., Zampighi, L.M., Fain, N., Lanzavecchia, S., Simon, S.A., and Wright, E.M. (2006). *Conical electron tomography of a chemical synapse: vesicles docked to the active zone are hemi-fused*. *Biophys J* 91, 2910-2918.
- Zenisek, D., Steyer, J.A., and Almers, W. (2000). *Transport, capture and exocytosis of single synaptic vesicles at active zones*. *Nature* 406, 849.
- Zhang, P., Land, W., Lee, S., Juliani, J., Lefman, J., Smith, S.R., Germain, D., Kessel, M., Leapman, R., Rouault, T.A., et al. (2005). *Electron tomography of degenerating neurons in mice with abnormal regulation of iron metabolism*. *J Struct Biol* 150, 144-153.
- Zhang, W., and Benson, D.L. (2001). *Stages of synapse development defined by dependence on F-actin*. *J Neurosci* 21, 5169-5181.
- Zhou, Y., Frey, T.K., and Yang, J.J. (2009). *Viral calciomics: Interplays between Ca²⁺ and virus*. *Cell Calcium* 46, 1-17.
- Ziese, U., Geerts, W.J.C., Van Der Krift, T.P., Verkleij, A.J., and Koster, A.J. (2003). *Correction of autofocusing errors due to specimen tilt for automated electron tomography*. *J Microsc* 211, 179-185.
- Ziv, N.E., and Garner, C.C. (2004). *Cellular and molecular mechanisms of presynaptic assembly*. *Nat Rev Neurosci* 5, 385.
- Zuber, B., Nikonenko, I., Klauser, P., Muller, D., and Dubochet, J. (2005). *The mammalian central nervous synaptic cleft contains a high density of periodically organized complexes*. *Proc Natl Acad Sci U S A* 102, 19192-19197.

Note

Parts of this work have been accepted for publication as:

R. Fernández-Busnadiego, B. Zuber, U. Maurer, M. Cyrklaff, W. Baumeister and V. Lučić: *Quantitative analysis of the native presynaptic cytomatrix by cryo-electron tomography*, J. Cell Biol. (in press)